Doctoral dissertation

Faculty of Physics, Astronomy and Applied Computer Science
Jagiellonian University, Kraków, Poland

Testing CPT symmetry in ortho-positronium decays at the precision of 10^{-4} with J-PET

Neha Chug

Supervisor:
prof. dr hab. Paweł Moskal

Auxiliary supervisor:
dr Aleksander Gajos

Kraków
December 2024

Wydział Fizyki, Astronomii i Informatyki Stosowanej
Uniwersytet Jagielloński

Oświadczenie

Ja niżej podpisany Neha Chug (nr indeksu: 1162819), doktorant Wydziału Fizyki Astronomii i Informatyki Stosowanej Uniwersytetu Jagiellońskiego, oświadczam, że przedłożona przeze mnie rozprawa doktorska pt. „Testing CPT symmetry in ortho-positronium decays at the precision of 10^{-4} with J-PET" jest oryginalna i przedstawia wyniki badań wykonanych przeze mnie osobiście, pod kierunkiem prof. dr. hab. Pawła Moskala oraz dr. Aleksander Gajos. Pracę napisałem samodzielnie.

Oświadczam, że moja rozprawa doktorska została opracowana zgodnie z Ustawą o prawie autorskim i prawach pokrewnych z dnia 4 lutego 1994 r. (Dziennik Ustaw 1994 nr 24 poz. 83 wraz z późniejszymi zmianami).

Jestem świadom, że niezgodność niniejszego oświadczenia z prawdą ujawniona w dowolnym czasie, niezależnie od skutków prawnych wynikających z ww. ustawy, może spowodować unieważnienie stopnia nabytego na podstawie tej rozprawy.

Kraków, dnia Podpis autora pracy

In loving memory of my grandparents, Nani maa and Nana ji.

Abstract

This work describes the experimental search for violation of fundamental discrete symmetries in the charged leptonic system consisting of electron and positron. It looks into the combined product of Charge, Parity, and Time (CPT) violating effects by performing a direct test for the electromagnetic interactions in the decays of the positronium atom. The experiment was performed with the 192 plastic strip Jagiellonian-PET detector and data was collected over one year from April 2021–August 2022. The CPT-sensitive angular correlation was studied for the identified ortho-positronium decays which is defined as the scalar product of ortho-positronium spin and the vector normal to the annihilation plane.

The main work of this thesis focuses on improving the present best experimental precision limits of the CPT symmetry test that was obtained with J-PET tomograph to the precision level of 0.00067 ± 0.00095 in 2021. The advancements were made in terms of the detection system by using a symmetric-shaped positronium production medium and a long run of data taking with a low source activity. It resulted in identifying around 48 million ortho-positronium events for this test. The results are consistent with the conservation of CPT symmetry at the precision of 0.00022, an improvement of factor four to the previous test.

The thesis also includes the first step realized to further improve the sensitivity of this test to 10^{-5} with a new Modular J-PET detector. A Monte Carlo simulation study was performed to optimize the best detector configuration of the detector system with the Modular J-PET for the future generation of CPT tests with J-PET.

Streszczenie

W pracy opisano eksperymentalne poszukiwania naruszenia podstawowych dyskretnych symetrii w naładowanym układzie leptonowym, składającym się z elektronów i pozytonów. Praca dotyczy badania symmetrii C, P i T oraz ich kombinacji CPT, przeprowadzając bezpośredni test interakcji elektromagnetycznych w rozpadach atomu pozytonium. Eksperyment przeprowadzono za pomocą 192-paskowego tomografu J-PET zbudowanego ze scyntylatorów plastikowych, a dane zbierano przez ponad rok, od kwietnia 2021 do sierpnia 2022. Badano korelację kątową wrażliwą na CPT dla zidentyfikowanych rozpadów orto-pozytonium, która jest zdefiniowana jako iloczyn skalarny spinu orto-pozytonium i wektora normalnego do płaszczyzny rozpadu.

Główne zadanie tej pracy skupia się na zwiększeniu precyzji obecnie najlepszych eksperymentalnych testów symetrii CPT, uzyskanych za pomocą tomografu J-PET, do poziomu precyzji 0.00067 ± 0.00095 w 2021 roku. Udoskonalenia dokonano w zakresie systemu detekcji poprzez zastosowanie ośrodka do produkcji pozytonium o symetrycznym kształcie i wydłużeniu okresu gromadzenia danych przy niskiej aktywności źródła. Zaowocowało to zidentyfikowaniem na potrzeby tego testu około 48 milionów zdarzeń z orto-pozytonium. Wyniki są zgodne z zachowaniem symetrii CPT przy precyzji 0.00022, co stanowi poprawę o czynnik 4 w stosunku do poprzedniego testu.

Praca obejmuje takie pierwszy krok mający na celu dalsze zwiększenie czułości tego testu do 10^{-5} za pomocą nowego modularnego detektora J-PET. Przeprowadzono badanie symulacyjne Monte Carlo w celu optymalizacji najlepszej konfiguracji modułowego detektora J-PET na potrzeby przyszłych testów symetrii CPT.

10:1305528600

Contents

Introduction

The study aims to improve the precision of discrete symmetries tests in the charged leptons by searching for the CPT odd decays of positronium. The CPT symmetry, a combined product of charge, parity, and time, is tested by measuring the angular correlations between the spin direction of ortho-positronium and the momenta of its annihilation photons. Any deviation of angular correlation amplitude from zero larger than 10^{-9} would signal a violation of symmetry [1, 2, 3]. At the precision level of 10^{-9}, false asymmetry effects arising from photon-photon interactions are predicted [4].

The measurements for the CPT symmetry test are conducted using a 192-strip Jagiellonian PET detector, made of plastic scintillators [5, 6, 7]. The detector is capable of recording different kinematics of annihilation photons from positronium decays. The methodology applied in this thesis is based on ref. [1]. J-PET has already performed its first CPT symmetry test with no observed violation to the precision level of 0.00067 ± 0.00095 [8]. The results obtained in ref. [8] are so far the best precise test of CPT in ortho-positronium decays. The previous best experiment conducted by the Gammasphere detector in 2003 achieved a precision of 0.0026 ± 0.0031 [9].

This work aims to improve the precision achieved in the earlier test, which is limited by the statistics of the collected ortho-positronium (o-Ps) atoms. Here a new experimental setup is discussed that aims to increase the o-Ps production rate in J-PET allowing to improve the statistics and hence to improve the precision. This setup employs a large annihilation chamber where o-Ps atoms are produced via e^+e^- interactions. The annihilation events o-Ps $\rightarrow 3\gamma$, recorded in the detector, are used to test the CPT-odd angular correlation operators. The use of large annihilation chamber allows to estimate the spin axis for each registered o-Ps event. The measurements are performed using a low-activity radioactive source for the duration of 356 days. Low positron source activity ensured low background from accidental coincidences.

A significant part of the thesis involves analyzing the experimental data to estimate the expectation value of the CPT odd operator. Additionally, a Monte Carlo simulation study is performed to identify o-Ps signal events and the background that mimics these events in this test. This work results in reaching a new limit of CPT invariance in positronium decays using the J-PET detector. Furthermore, a simulation study for the next generation of CPT symmetry test with the new J-PET technology is carried out to optimize detector configuration in view of further improving the precision of CPT symmetry test at the level of 10^{-5}.

This thesis is divided into eight chapters. Chapter 1 introduces the discrete symmetries and the positronium properties that make it a suitable candidate for this test. It also presents angular correlation operators to test the symmetry violation in ortho-positronium decays, compares the sensitivity of different experiments searching for CPT violations, and introduces the upcoming technologies aimed to improve the test precision. Chapter 2 describes the J-PET experimental setup and properties of the detector for testing CPT symmetry. It provides details on the long-term measurement performed for this test and the data reconstruction. Chapter 3 outlines the selection criteria for identifying o-Ps $\rightarrow 3\gamma$ decays in the experimental data. Chapter 4 presents a comparison of experimental data with Monte Carlo simulations, along with a detailed background study for the CPT symmetry test with J-PET. Chapter 5 discusses the various trials done to understand the impact of section cuts and threshold variables on the the CPT-odd angular correlation operator in both experimental data and MC simulations. It also addresses the checks for different sources of systematic in this test. Chapter 6 summarizes the final result of this thesis work, estimating the amplitude of CPT-violating effects and its comparison with the previous experiments. Chapter 7 focuses on the simulation study using a new prototype of the J-PET detector where the different configurations of the detector setup are studied in view of finalizing one detector geometry for the next CPT symmetry test. Chapter 8 concludes the whole thesis work and provides a future perspectives of improving the precision of CPT symmetry test with J-PET.

Author's contribution:

In context to the thesis work, the author actively participated in the mounting of a spherical annihilation chamber inside the J-PET detector to start measurements for the CPT symmetry test that took place in 2021. The author monitored the two experimental measurement campaigns with the spherical chamber and J-PET over the course of one year from April 2021 - August 2022. Additionally, the author prepared the online monitoring analysis code for these measurements. Around 1 PB of data was collected from these measurements. The author performed the preselection of the data which resulted in effectively reducing the size of the total data. The author prepared and implemented the analysis criteria for the signal selection in this study for data as well as Monte Carlo simulations [a], given in Chapters 3 and 4. The positronium production and annihilation setup was integrated into the MC simulations by the author. The author generated and analyzed the Monte Carlo simulation events for this study, as outlined in Chapter 4. The author performed the systematic studies for this test, given in Chapter 5. The author also contributed to the testing of the Modular J-PET detector, implementing simulations for various detector configurations, as discussed in Chapters 7. These studies aimed to optimize the detector setup for future CPT symmetry tests [b, d]. The author also contributed to the preparation of online monitoring of measurements with Modular J-PET for the next-generation CPT symmetry test as well as participated in data taking [e]. The results of this thesis are being formulated into a research article, which is currently under preparation [g]. Throughout the Ph.D. program, the author presented these results at numerous international conferences.

Relevant articles associated with this thesis work include:

[a] N. Chug and A. Gajos, "CPT symmetry test in positronium annihilations with the J-PET detector", *Proceedings of Science (PANIC2021), 440* (2022).

[b] N. Chug and A. Gajos, "Towards Improving the Sensitivity of the CPT Symmetry in Positronium Decays with the Modular J-PET Detector", *Acta Phys. Polon. B Proc. Suppl. 15, 4-A6* (2022).

[c] N. Chug and A. Gajos, "Modular J-PET with Improved o-Ps Detection Efficiency for CPT Tests", *CPT and Lorentz Symmetry, World Scientific Book, 253-255* (2023).

[d] N. Chug and A. Gajos, "Improved test of CPT invariance in ortho-positronium decays at J-PET", *PoS (DISCRETE2022), 064* (2024).

[e] N. Chug, "Exploring the limits of CPT symmetry in ortho-positronium decays with J-PET", *PoS (EPS-HEP2023), 366* (2024).

[f] N. Chug and P. Moskal, "Classification of signal events for CPT symmetry studies with J-PET using Machine learning techniques", *Acta Phys. Polon. B Proc. Suppl. 17, 7-A2* (2024).

[g] N. Chug, P. Moskal, *et al.,* "Studies of CPT symmetry in positronium decays with 192 plastic strip J-PET detector", in preparation.

Chapter 1

The CPT Symmetry

A persistent challenge in fundamental physics lies in rigorously quantifying deviations from, or upholding the exactness of, discrete symmetries observed in nature. This endeavor has the potential to unveil new physics through symmetry breaking, a phenomenon that has previously led to revision of the existing theoretical frameworks and may yet require the introduction of entirely new ones if new breaking mechanisms are observed. Conversely, if experiments continuously refining their sensitivity to symmetry violation effects do not observe deviations from these fundamental invariances, it strengthens the existing theoretical frameworks by setting stringent constraints on the possible magnitude of effects not foreseen by these frameworks.

1.1 Historic background

The discrete symmetries include Charge-conjugation (C), Parity (P), and Time-reversal (T) and their combinations of CP, CPT, etc. The P symmetry means invariance of physics laws under the space inversion transformation corresponding to the reversal of the three spatial axes of the system ($\vec{r} \rightarrow -\vec{r}$) and the T symmetry transformation corresponds to invariance under the inversion of the time coordinate (t $\rightarrow$ -t). The C symmetry transformation is linked to the exchange of particles with their antiparticles under which all kinds of charges change signs without affecting space-time-related quantities [10].

The year 1956-57 witnessed a paradigm shift in understanding fundamental symmetries. Lee and Yang, through their theoretical exploration of the θ-τ puzzle, laid the groundwork for questioning parity conservation in weak interactions [11]. Their theoretical prediction of parity non-conservation in weak interactions received experimental confirmation through Wu's beta decay experiment in 1957 [12]. Subsequent studies confirmed this violation in the decays of π and μ particles [13, 14]. These experiments also demonstrated the non-conservation of charge symmetry in weak interactions [15]. Following these discoveries, the question of the conservation of the combined CP symmetry arose. The first evidence of CP violation in weak interactions, observed in the decays of neutral kaons in 1964 [16], implied T violation through the CPT theorem [17].

The CPT theorem postulates the invariance of all interactions under the combined transformation of charge conjugation, parity, and time reversal [18]. Therefore, if CP symmetry is violated, T symmetry must also be violated to maintain the validity of the CPT theorem. While the theoretical implications pointed towards T violation, direct experimental confirmation remained elusive for some time. This gap was bridged by the CPLEAR experiment in 1998, which provided the first concrete evidence of T violation in neutral kaon decays [19]. There were controversies about whether the CPLEAR result was a direct T violation observation as the observed asymmetry could just as well arise from CP violation; under CPT. This means T violation as well, but some argued that a true "direct" T symmetry violation observation would be one that could not be caused by CP violation. In that sense, the BaBar result in 2012 was the first direct observation of T violation in B meson decays [20].

To date, CPT symmetry remains the last of the fundamental symmetries which was never observed to be violated. Numerous experimental approaches have been and continue to be developed to test its validity across different particle systems. Despite the lack of a direct violation, these tests have established stringent experimental limits. The significant implication of the CPT theorem is that particles and their antiparticles should possess identical properties, including mass, lifetime, electric charge, and magnetic moment.

Current CPT symmetry tests primarily focus on a comparison of fundamental properties between particle-antiparticle pairs. These properties include mass, lifetime, electric charge, and magnetic moment [3]. High-precision penning-trap experiments exemplify such direct tests by comparing the charge-to-mass ratio and magnetic moments of proton and antiproton [21, 22]. Similarly, other highly sensitive tests involve comparing the magnetic moments and masses of electrons and positrons [23, 24]. Another approach utilizes hyperfine spectroscopy measurements with anti-hydrogen, where the 1S-2S transition energy is compared with hydrogen. The CPT theorem predicts identical spectra for both hydrogen and anti-hydrogen [25, 26].

Beyond comparisons of fundamental properties, CPT symmetry can also be tested by analyzing particles' interactions. One approach involves comparing decay channels in weak interactions. For instance, CPT symmetry demands that the decay rates of neutral mesons into two charged and neutral pions be identical [27]. Another method investigates the correlations observed during Positronium decay in electroweak interactions. Deviations from the expected correlations would signal a violation of CPT symmetry [28]. Looking to the future, the AEgIS collaboration aims to test the gravitational interaction of antimatter using anti-hydrogen and also using positronium [29]. This experiment could provide even more precise limits on CPT symmetry violation [30].

The research presented in this thesis focuses on the CPT symmetry test in electromagnetic interactions with the 3γ decays of polarised positronium atoms using the angular correlations between positronium spin and momenta of the annihilation photons [28, 31].

1.2 Motivation for investigating CPT symmetry

There are several motivations for conducting experimental investigations into the fundamental nature of CPT symmetry [2, 32]. Exploring the invariance of CPT symmetry is crucial for several reasons. A few important reasons are:

- **Searching for manifestations of physics not foreseen by the Standard Model:** The theoretical framework of the SM rests upon the foundational pillars of CPT and Lorentz symmetry. CPT violation implies Lorentz violation, a significant prediction of the Standard-Model Extension (SME) [33, 34]. Investigating potential violations of CPT symmetry provides insights into theories that extend beyond the established framework of particle physics.
- **Testing the universality of fundamental physical laws:** CPT symmetry's validity is intrinsically linked to fundamental principles such as Lorentz invariance and quantum mechanics. The validity of CPT symmetry within the SM and quantum theories hinges on assumptions regarding these foundational principles. Any observed violation of CPT symmetry would imply a breakdown of this fundamental symmetry, prompting a reassessment of our understanding of the universe's underlying laws.
- **Explaining the Matter-Antimatter Asymmetry:** The abundance of matter in the Universe is explained by the Sakharov postulate on C and CP violation [35]. The Standard Model prediction on CP violation is insufficient in explaining this imbalance. It is hypothesized that CPT violation could have served as a mechanism during the Big Bang, ultimately leading to the creation of more matter than antimatter.

1.3 Positronium, QED, and CPT

Significant efforts have been made to search for symmetry violations in the lepton system including electrons, muons, neutrinos, etc. Neutrino oscillation experiments offer a sensitive tool to investigate potential CPT violations within the leptonic sector. These experiments exploit the phenomenon of neutrino oscillation, where a neutrino of one flavor (e.g., electron neutrino) can transform into another flavor (e.g., muon neutrino) as it travels. By measuring the masses and mixing parameters of neutrinos and their antiparticles (antineutrinos), they search for deviations from the behavior expected under CPT symmetry. The T2K neutrino oscillation experiment yielded the first hint of CP violation in the leptons with a statistically significant level of 3σ [36]. While no definitive CPT violation has been observed to date, next-generation neutrino oscillation experiments promise even greater sensitivity to potential CPT violation effects [37].

Explorations with charged leptons also contribute to the quest for CPT violation. High-precision measurements of the magnetic moments of single electrons (e^-) and positrons (e^+) have yielded results that are in agreement with the quantum electrodynamics (QED) predictions based on the fine-structure constant [38]. These precise comparisons offer a stringent test of CPT symmetry,

with current experimental limits reaching a precision level of 10^{-12} [2, 39, 40]. It is worth noting that QED, the theoretical framework governing the physics of charged leptons, does not predict CPT violation.

1.3.1 Positronium: A Unique Probe for QED Tests

Positronium (Ps), an exotic bound state system composed of an electron and its antiparticle, a positron, presents a unique investigative tool for testing high-precision QED theory [2, 41]. Recent tests involving positronium fine-structure measurements have revealed discrepancies between experimental results and QED predictions [42]. These discrepancies highlight the importance of further investigations into the structure and interactions within positronium.

Positronium is described by a set of quantum numbers n, L, S, and j (principal quantum number, orbital angular momentum, combined spin state of electron and positron, and total angular momentum (L+S)). In the ground state (L=0), Ps can exist in two distinct configurations based on the spin S of the electron and positron:

- **Singlet $^1\mathbf{S}_0$:** The state where spins of e^+ and e^- are anti-parallel with total spin S = 0. This state of Ps is termed para-positronium (p-Ps) with a mean lifetime of 125 ps in vacuum [41].
- **Triplet $^3\mathbf{S}_1$:** It is known as ortho-positronium (o-Ps) where total spin S = 1 with a longer mean lifetime of 142 ns in vacuum [41].

These distinct spin configurations of the electron-positron pair give rise to four possible quantum states for positronium [4]

$$\begin{aligned}
&|S| = 0\,,\ m_s = 0\,;\ |\Psi_S\rangle = \frac{1}{\sqrt{2}}(\,|\uparrow\downarrow\rangle - |\downarrow\uparrow\rangle\,)\,,\\
&|S| = 1\,,\ m_s = 1\,;\ |\Psi_S\rangle = |\uparrow\uparrow\rangle\,,\\
&|S| = 1\,,\ m_s = 0\,;\ |\Psi_S\rangle = \frac{1}{\sqrt{2}}(\,|\uparrow\downarrow\rangle + |\downarrow\uparrow\rangle\,)\,,\\
&|S| = 1\,,\ m_s = -1\,;\ |\Psi_S\rangle = |\downarrow\downarrow\rangle\,.
\end{aligned} \tag{1.1}$$

The two ground states of positronium (p-Ps and o-Ps) exhibit well-defined properties under parity (P), charge conjugation (C), and time reversal (T) transformations. Under Charge Conjugation (C = $(-1)^{L+S}$) the behavior of o-Ps and p-Ps differ. For o-Ps (S = 1, L = 0), the C transformation results in an odd state (C = -1) while in p-Ps (S = 0, L = 0) it results in an even state (C = +1) to the initial spin state. Under Parity transformation (P = $(-1)^{L+1}$), both o-Ps and p-Ps exhibit odd parity (P = -1). For the combined charge parity, CP = $(-1)^{S+1}$, which means for o-Ps the final state has CP = 1 whereas for p-Ps the final state has CP = -1. Since QED conserves CP symmetry for Ps decays and by the conservation law $(-1)^{L+S} = (-1)^n$ for these decays, the o-Ps ground state decays into odd number of photons and p-Ps decays into even number [43]. A pictorial representation of the decays of Ps is given in Fig 1.1.

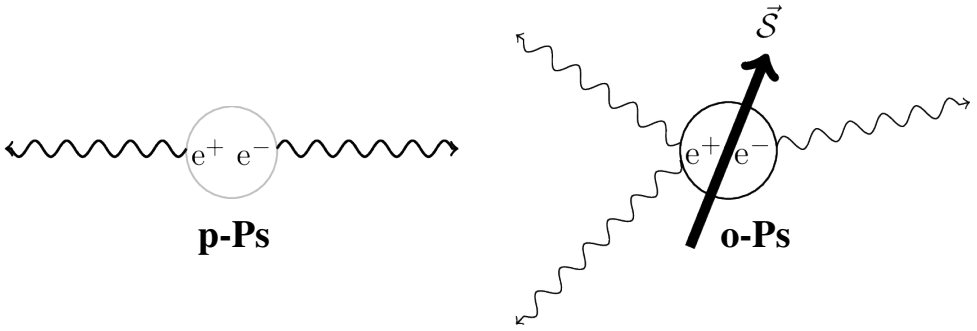

FIGURE 1.1: **Positronium decays.** The singlet (p-Ps) and triplet (o-Ps) states of the positronium atom decay into two and three annihilation photons, respectively.

1.3.2 Precision studies with positronium decay processes

The unique properties of Ps decay processes make them ideal candidates for high-precision studies of fundamental symmetries in particle physics. Some key tests can be:

- **Search for C-Symmetry Violation:** Search for forbidden decay processes due to violation of C symmetry e.g. decays of p-Ps (o-Ps) to an odd (even) number of photons [44]. The experiments designed to test C symmetry invariance measure the branching ratio of the forbidden decays of Ps (e.g. $^1S_0 \rightarrow 3\gamma$ decay which is C forbidden). Any deviation in the branching ratio from zero results in setting the limit of C symmetry non-invariance. The upper limit for those decays is in order of 10^{-7} [45].
- **Tests of CP and CPT Symmetry:** Tests of CP and CPT symmetry involving the angular correlation operators from photons momenta and its polarization [1, 28, 46].
- **Invisible Decay of Ps and Light Dark Matter:** Invisible decay of Ps to estimate its single photon decay rate that could constitute the signal of light Dark Matter in Ps [47].

1.4 Search for Discrete Symmetry violation with ortho-positronium

The model-independent approach to search for discrete symmetry violation in 3γ decays of positronium was first proposed in the work of Bernreuther et al. [28]. Certain angular correlations can be defined using the annihilation photons momenta and ortho-positronium spin to test the CP and CPT symmetry invariance in the charged lepton system, mentioned in Table 1.1. Even correlations are denoted with a '+' sign while odd ones with a '-' sign. Odd correlations can be used to test the respective symmetry conservation in Ps decay. Any signature of violation of discrete symmetry would come as a non-zero expectation value of such odd operators [10].

Some restrictions exist in using these correlations for the symmetry test. The CP and CPT symmetry is conserved in QED for Ps decays but there are final state interaction effects of photons that could mimic CPT violating effects in o-Ps decays at the precision level of 10^{-9} [4]. The other

possible effect is the weak interaction amplitude in Ps due to parity mixing and weak decays of its state that constitute the CPT violation at the precision of 10^{-12} [4, 28].

TABLE 1.1: Angular correlation operators in the three-photon decay of ortho-positronium. '+' and '-' denote whether an operator is even or odd under a given symmetry transformation. The momenta of annihilation photons are represented by k_i, where $k_1 > k_2 > k_3$, and S represents the spin of o-Ps.

Operators	C	P	T	CP	CPT
$\vec{S}\cdot\vec{k_1}$	+	-	+	-	-
$\vec{S}\cdot(\vec{k_1}\times\vec{k_2})$	+	+	-	+	-
$(\vec{S}\cdot\vec{k_1})\,(\vec{S}\cdot(\vec{k_1}\times\vec{k_2}))$	+	-	-	-	+

The transformation of individual vectors used to construct the above-defined operators in o-Ps $\rightarrow 3\gamma$ decay is given in Equation 1.2. The spin of decaying o-Ps changes its direction under T transformation and the momentum of annihilation photons reverses its direction both under P and under T discrete symmetry. The vector product $(\vec{k_1}\times\vec{k_2})$ remains unaffected after applying the P or T transformation.

$$\begin{aligned} \vec{k_i} &\xrightarrow{\text{P , T}} -\vec{k_i}\,, \\ \vec{S} &\xrightarrow{\text{T}} -\vec{S}\,, \\ \hat{n} = (\vec{k_1}\times\vec{k_2}) &\xrightarrow{\text{P , T}} \hat{n}\,. \end{aligned} \tag{1.2}$$

To date, the CP and CPT symmetry invariance in o-Ps decays has been experimentally verified at the precision level of 0.00067 ± 0.00095 [8]. There is a range of five orders of magnitude unexplored to test the CP and CPT symmetry invariance. The research work in this thesis focuses on pushing the experimental sensitivity into the unexplored region, i.e. searching for the violations at a higher precision than the already achieved level of 0.00067 ± 0.00095 [8].

1.4.1 Experimental tests of CPT symmetry with o-Ps

The first experimental test of CPT violating angular correlation $\vec{S}\cdot(\vec{k_1}\times\vec{k_2})$ was started in 1988 [4]. The CPT-odd operator is the angular correlation between o-Ps spin and normal to the decay plane orientation of the o-Ps atom, shown in Fig 1.2. The search for the non-zero expectation value of the operator would indicate symmetry violation. A non-zero correlation implies that the number of events with a spin direction parallel to the direction of normal to the decay plane (N_+) is not equal to the number of events with a spin direction anti-parallel to the direction of normal to the decay plane (N_-). The up-down asymmetry is estimated from an asymmetric parameter

$$A = \frac{N_+ - N_-}{N_+ + N_-}\,. \tag{1.3}$$

The amplitude of symmetry violation effects C_{CPT} is estimated from the asymmetric parameter and the analyzing power of the experimental setup.

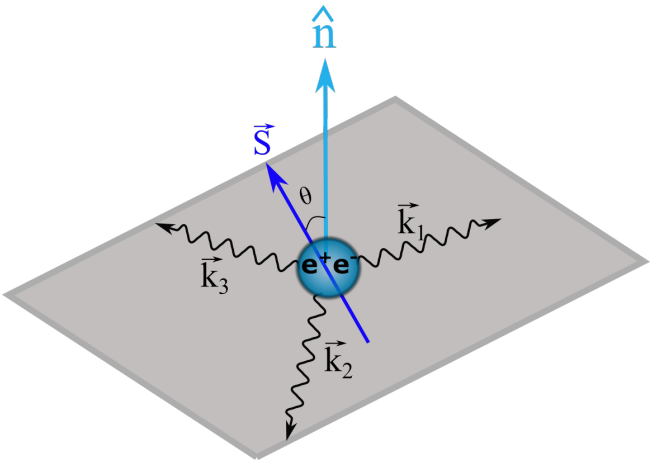

FIGURE 1.2: **CPT sensitive operator from o-Ps spin and decay plane.** The decay of o-Ps to three annihilation photons in one plane. The photons' momenta given as $\vec{k_1}$, $\vec{k_2}$ and $\vec{k_3}$ are ordered in decreasing values of their energy. The vector $\vec{S}$ represents the spin of decaying o-Ps (given in a dark blue color). The normal to the annihilation plane, denoted by $\hat{n}$, is a vector product from the momentum of the two most energetic annihilation photons ($\vec{k_1} \times \vec{k_2}$). The angle between spin and vector product is denoted by theta.

The best precise experimental tests of CPT symmetry are listed in Table 1.2.

TABLE 1.2: Measurements done so far to test the CPT-odd angular correlation operators in o-Ps to 3γ decays. The CPT violation coefficients C_{CPT} are mentioned indicating the precision obtained with different experiments. The Table is adapted from ref. [43] with an addition of recent results of the CPT symmetry test as a last entry.

No.	CPT-odd operator	Violation coefficient	Year
1.	$\hat{S} \cdot (\hat{k_1} \times \hat{k_2})$	$C_{CPT} = 0.020 \pm 0.023$	1988 [4]
2.	$\hat{S} \cdot (\hat{k_1} \times \hat{k_2})$	$C_{CPT} = 0.0140 \pm 0.0190$	2000 [48]
3.	$\hat{S} \cdot (\hat{k_1} \times \hat{k_2})$	$C_{CPT} = 0.0071 \pm 0.0062$	2003 [9]
4.	$\hat{S} \cdot (\hat{k_1} \times \hat{k_2})$	$C_{CPT} = 0.00067 \pm 0.00095$	2021 [8]

The first two experiments in Table 1.2 used an array of NaI detectors where the scintillators were arranged in a way to record two of the three most energetic photons. They used the polarized positron beam or polarizing Ps using an external magnetic field for the fixed Ps spin direction. The first most energetic photon was recorded in one fixed scintillator, while the second one can be recorded in any one of the other two at a single time. The change in detector alignment was required to record the opposite orientation of the spin to normal to the decay plane. These experiments reverse the normal to decay plane and o-Ps spin and estimate the asymmetry ratio (A) by averaging over the recorded events with two different spin directions. These studies were sensitive to the geometrical asymmetries and found no CPT violation at the precision level of 10^{-2} [48, 49]. These were the only experiments capable of recording up-down asymmetry due to their construction which is an important difference with respect to how Gammasphere and J-PET do it later.

The third experiment was the most precise CPT symmetry tested with the 4π Gammasphere detector using arrays of high-purity germanium (HPGe) [9]. The possibility of recording all three photons from Ps annihilation allowed it to estimate the different orientations of normal to the decay plane of o-Ps with respect to a given spin direction, which is given by θ,

$$cos\theta = \hat{S} \cdot (\vec{k_1} \times \vec{k_2}) / \mid \vec{k_1} \times \vec{k_2} \mid \tag{1.4}$$

The up and down asymmetry (A) was estimated for all possible orientations θ of the decay plane and resulted in the observation of CPT conservation at the precision level of 10^{-3}. These studies were less sensitive to the asymmetries from detector efficiency.

The most recent results with the J-PET detector resulted in improving the precision of this test by a factor of three and consistent with CPT conservation at the level of $\pm$ 0.00095 [8]. The detector from plastic scintillators has a better timing and angular resolution (250 ps and 1 degree) of recording o-Ps to 3γ compared to the Gammasphere detector with 4.6 ns and 4 degrees [50], respectively. The features like the spin estimation of each o-Ps event without the use of an external magnetic field and estimating the measure of asymmetry from the expectation value of the CPT-odd angular correlation (integral over the whole angle/theta region), make it different from previous experiments.

This thesis reports on improving the resolution of this study with a J-PET detector as compared to the last results by a factor of five with no observation of CPT violation at a precision of 9.5×10^{-4}. It also includes the study on attempts to further improve the sensitivity of this study to 10^{-5} precision with a new detector prototype.

1.4.2 CP symmetry tests with Ps

It is worth mentioning that the CP odd angular correlation operator $(\vec{S} \cdot \vec{k_1})(\vec{S} \cdot (\vec{k_1} \times \vec{k_2}))$ has been used to test the CP invariance in o-Ps decays to the precision of 10^{-3} [51]. A new methodology is developed at J-PET to test the discrete symmetries in o-Ps decays using the polarization of annihilation photon [1]. The angular correlation is defined as

$$O = \epsilon_i \cdot k_j / (\mid \epsilon_i \mid \cdot \mid k_j \mid), \tag{1.5}$$

where $\epsilon_i = k_i \times k_i'$. The angular correlation consists of the polarization of the annihilation photon from the momentum of one photon before (k_i) and after it gets Compton scattered in the detector (k_i') and the momentum of another photon. The operator is odd under the CP, P, and T transformation and hence makes it possible to test CP symmetry in positronium decays. The recent results of this study are consistent with the CP symmetry conservation in charged leptonic section at the precision of $\mathcal{O}(\mathcal{CP})$ = 0.0005 $\pm$ 0.0007 [52].

1.4.3 Upcoming experiments

There are a few new detector system prototypes designed to search for CP and CPT violations in Ps decays further improving the sensitivity of these tests. The new APEX detector from an array of 24 NaI(Tl) is arranged cylindrically in one layer with 3/4 of 4π angular coverage designed for the detection of o-Ps events [53]. It utilizes the trigger method of tagging 1.2 MeV prompt photon (from ^{22}Na decay) instead of positron tagging, as utilized in the J-PET experiments [1, 31, 54]. The other technology is a KAPAE detector made of BGO crystals designed to detect the annihilation photons from Ps decays with higher angle resolution [55]. The source being enclosed directly within the sensitive material of the detector provides higher detection efficiency of registering photons in all directions. The trigger system is used to tag positrons when they reach the region of aerogel to form Ps. The detector can improve the statistical limit for the sensitivity of the CPT violation angular correlation by a factor of 9 times as compared to the J-PET detector [56]. Another new detector from LYSO crystals is being developed at Michigan State University in the United States that aims to improve the precision of CP violating angular correlation by a factor of 10 in Ps decays [57].

Chapter 2

The J-PET Experiment

The thesis presents an experimental search for potential violations of CPT symmetry in the decays of ortho-positronium atoms. In this thesis, a second generation of the experimental setup is applied following the methodology described in reference [1]. The investigation entails determining the expectation value of the CPT-odd angular correlation operator, derived from the positronium spin and the momenta of annihilation photons resulting from ortho-positronium decay. The study is conducted with a specialized detection system designed to record the multi-photon final states generated from electron-positron annihilation within a low ($\sim$ 1 MeV) energy range. This chapter presents a detailed overview of the experimental setup to test the CPT symmetry violation in the charged lepton system used in this work.

2.1 The Detector

With a broader goal of developing a cost-effective Positron Emission Tomography (PET) scanner and advancing fundamental physics research, the J-PET device was designed in 2009 at the Jagiellonian University in Krakow, Poland [58, 59, 60]. Named after its purpose, the Jagiellonian Positron Emission Tomograph (J-PET) serves as a versatile detector optimized for recording photons emitted from annihilations of e^+ e^- or via the formation of positronium atom [1].

The J-PET detector comprises 192 plastic scintillator strips configured in a cylindrical arrangement, as illustrated in Fig. 2.1 [5, 7]. J-PET utilizes a triggerless data acquisition system (DAQ) comprising Field Programmable Arrays (FPGAs) implemented with Time-to-Digital Converters (TDCs) [61, 62]. Initially, the electrical signals from the Photomultiplier Tubes (PMTs) undergo probing at four distinct thresholds, constituting a multi-threshold system [63, 64]. At each threshold level, the arrival time and width of the signal are observed and digitized via TDCs. Consequently, for each signal, four timing points are recorded at both the leading and trailing edges.

Such data is collected from all PMTs within the detector and subsequently processed in the DAQ system using FPGAs.

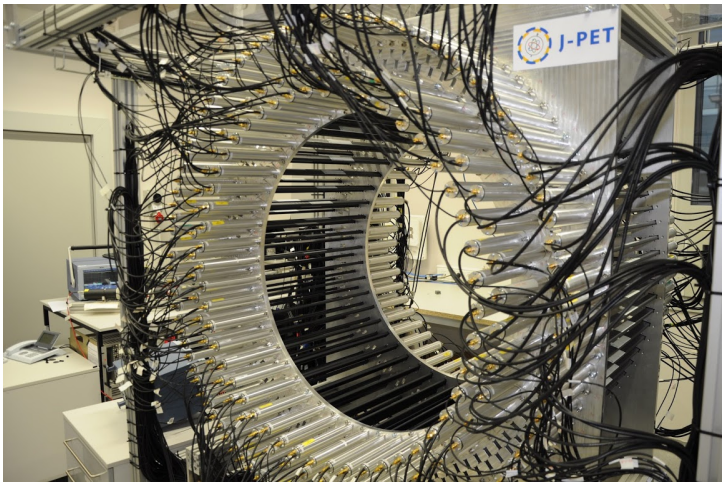

FIGURE 2.1: **The J-PET Detector.** The detector constructed of plastic EJ-230 material scintillators where each strip with dimensions of $50 \times 1.9 \times 0.7$ cm^3 and is enveloped in Vikuiti ESR foil [7]. Structurally, the detector consists of a triple-layered barrel, with 48, 48, and 96 scintillators positioned in the first, second, and third layers, respectively, forming radii of 42.50 cm, 46.75 cm, and 57.50 cm from the center of the scintillator array. Optical coupling of the two ends of the scintillators is achieved with vacuum Photomultiplier Tubes (PMTs) with photocathode of 22 mm diameter, specifically Hamamatsu R9800 type, responsible for the conversion of collected light (or photon interactions in scintillator) into electrical signals.

In organic scintillators, the primary mode of gamma interaction involves Compton scattering, whereby photons do not fully transfer their energy in a single interaction. This contrasts conventional PET scanners utilizing crystal scintillators, where photons deposit their energy through the photoelectric effect in 40% cases and where the photoelectric effect is void for PET imaging [65].

2.1.1 Properties of the J-PET detector

Plastic scintillators in the J-PET exhibit fast-timing properties with a signal rise and decay time of 0.5 ns and 1.5 ns, respectively [66]. The annihilation photons are detected at a time resolution of 220 ps in the detector system [7]. The ability to resolve the pile-up events thanks to the high time resolution, leads to the use of high-intensity radioactive sources in J-PET. The use of a high number of scintillator strips in the detector enhances its granularity. The larger geometrical acceptance and angular resolution of around 1° for annihilation photons makes it capable of recording different kinematical configurations of annihilation photons from e^+e^- and decays of positronium atoms. Its unique feature of estimating photons' polarization has resulted in testing discrete symmetry violation in positronium decays [52]. Additionally, detecting secondary Compton-scattered photons within J-PET facilitates studies on the quantum entanglement of annihilation photons [67, 68, 69, 70]. Furthermore, the detector system enables Positronium imaging by detecting annihilation and de-excitation photons [31, 54, 71, 72, 73]. The internal space of the detector can be equipped with interchangeable setups for positronium production medium [74], as elaborated in subsequent sections of this chapter.

2.2 Experimental setup

The experimental setup used to test the CPT-odd angular correlation in this work constitutes the 3-layer J-PET detector system with an annihilation chamber for positronium production, which is presented in Fig. 2.2. The spherical-shaped large annihilation chamber was constructed at UMCS Lublin, Poland. The chamber consists of two Plexiglas hemispheres with a radius of 10 cm each. The inner walls of hemispheres are coated with a 2 mm thick and 2.5 g/cm^3 dense RG60 porous silica aerogel as shown in Fig. 2.4 (b). The porous materials are required for a high fraction of o-Ps atoms annihilating to three photons. The porosity depends on the pore size of the material [75]. In the experiment, the aerogel layer is formed from the mesoporous SiO_2 and gypsum mixture with a 15-25 nm pore size [8].

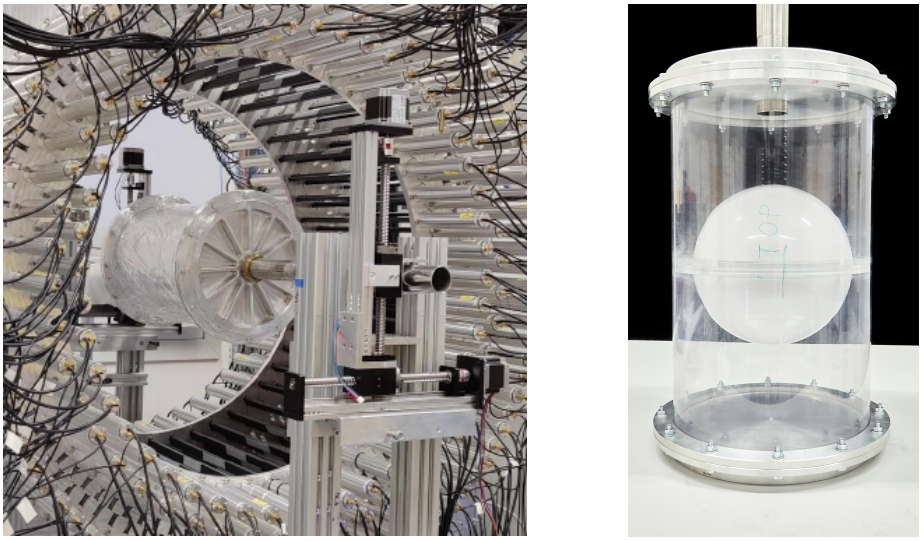

(a) **(b)**

FIGURE 2.2: **Experimental setup for CPT symmetry test.** (a) Picture of 192 plastic strips J-PET detector with spherical annihilation chamber placed at its center. (b) The assembly of a spherical annihilation chamber inside the cylindrical tube.

2.2.1 Improvements in comparison to the first CPT symmetry test with J-PET

The first test of CPT symmetry with J-PET was done in 2018 using a cylindrical-shaped annihilation chamber [8]. Due to the chamber's geometry with open ends of the cylinder, there was a geometrical constraint that the positrons reaching the ends of the chamber wouldn't be able to form positronium.

For the studies presented in this thesis, a symmetric annihilation chamber was proposed to maximize the utilization of the emitted positrons. As a result, this study is done with a symmetric spherical-shaped annihilation chamber that results in 1.5 times higher positronium formation than the cylindrical chamber [76] as given in Fig. 2.3. The first test used a 30-day measurement with 10 MBq source activity. In addition, there is a 356-day-long measurement with a lower source

activity of 1.1 and 4 MBq. Lowering activity gives less background to the studies and the longer run of data taking compensates for using higher source activity.

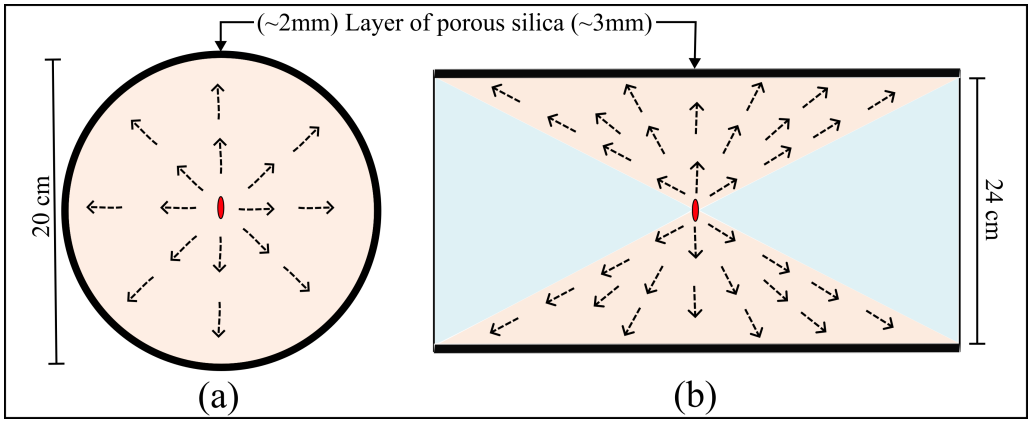

FIGURE 2.3: **Annihilation chamber setup used so far for the CPT symmetry test with J-PET.** (a) Spherical and (b) cylindrical-shaped annihilation chamber. Isotropic emission of e^+ from ^{22}Na source placed at the center of both chambers (marked in red color). There is a layer of porous silica ($\approx$ 2 mm in (a) and $\approx$ 3 mm in (b)) on the inner walls of the chamber (shown in black color). The region with arrows in (b) shows the volume in which emitted e^+e^- pairs may be detected. While in (a) this region is extended throughout the sphere, there are no such geometrical constraints on the formation of positronium (Ps) atom from a chamber point of view.

2.2.2 Present setup

A positron source, ^{22}Na used in the measurement was prepared by evaporating a water solution of ^{22}NaCl onto 7.5 μm thick and 1.065 mg cm^2 dense polyamide Kapton foil (shown in yellow color in Fig. 2.4 (a)). The Kapton foil allows the transmission of around 92% of positrons and the rest are passing through it [74, 77]. The source is placed along the equatorial plane of the hemisphere using a ring-like source holder made of plastic, as shown in Fig. 2.4 (a). There are four holes on the circumference of the hemisphere in a plane perpendicular to the equatorial plane to insert the source holder. The target is centered on the axis of the detector system with four spacer pins from polyoxymethylene each of length 1.7 cm and 0.25 mm thick strings (fishing thread) attached to the source holder.

The two identical hemispheres (shown in Fig. 2.4 (b)) are joined to form a spherical annihilation chamber with the radioactive source at its center. The plane of the source holder is vertical along the axis of the chamber. The spherical chamber is enclosed in the center of a polycarbonate tube closed by two aluminum endcaps which serve as a vacuum vessel as shown in Fig. 2.2 (b). The outer tube is 43 cm long, and 2 mm thick with an inner radius of 12.2 cm. The small space between the spherical chamber and the walls of the cylindrical tube is kept for uniform pumping out of the air.

Vacuum is maintained inside the chamber to minimize the scattering of positrons from the ^{22}Na source. The whole chamber setup is placed inside the J-PET detector and is connected to the vacuum system through the long pipe at one endcap/lid as shown in Fig. 2.2. The vacuum system

in J-PET consists of a rotary and a turbomolecular pump along with the pressure gauges and monitoring system to record the pressure values for the two pumps. For this CPT symmetry test, the pressure inside the spherical chamber was kept lower than 1 Pa. A pressure lower than 1 Pa can minimize the scatterings in the chamber made of 3 mm thick plastic [74].

(a) **(b)**

FIGURE 2.4: **Spherical chamber setup.** (a) Picture of the interior of the spherical annihilation chamber where ^{22}Na source wrapped in Kapton foil (yellow) is attached to the ring-like source holder. The source holder is placed on one of the hemispheres through the four attached bolts. (b) Two hemispheres of the chamber with porous silica coating on its inner walls.

2.3 Data taking

The measurement campaign for the CPT symmetry test with a 3-layer J-PET and spherical annihilation chamber took 1.3 years of data taking. During this period, two experiments (internally labeled as J-PET Runs 12 and 13) were carried out with the same experimental setup except for different positron source activities. The set of multi-thresholds applied to the PMT in these two experiments are 30, 80, 190, and 300 mV. There are a total of 356 effective days of measurement where the data is collected at a pressure of less than 1 Pa inside the spherical chamber. On the remaining days, data is collected at comparatively higher pressure above 1 Pa or atmospheric pressure i.e. without the use of vacuum pumps. The comparison of studies at different pressures is shown in further chapters. The total volume of data collected from the above-mentioned measurements is around 2 petabytes. The data analysis presented in the following chapters of this Thesis is based on the entire data-set collected during these measurements.

2.3.1 Data reconstruction and preselection

The data collected during measurements with J-PET is preselected and analyzed from the perspective of identifying ortho-positronium events in this study using the J-PET Framework Analysis Software [78]. The J-PET raw data is stored in a binary format that consists of leading and trailing edge times of electric signal recorded at four fixed threshold voltages applied to a single photomultiplier in the detector. In the first stage of data reconstruction, these timestamps from a single photomultiplier are assembled to form a signal. The signals in a single detection module consisting

TABLE 2.1: The description of two experimental runs conducted for the CPT symmetry test with 3-layer J-PET and spherical annihilation chamber

J-PET Run	Source Activity (MBq)	Period	Number of effective days of measurement
12	1.1	April — Sept 2021	78
13	4	Oct 2021 — Aug 2022	278
Test Run	Cosmic	Oct & Dec 2020	60

of two PMTs at its ends are grouped to identify the gamma interaction in that scintillator strip to form a hit, shown in Fig. 2.5. The pairing is done when the arrival time of these signals is within the range of 6 ns. At the last stage, the groups of hits (γ interaction in the scintillator) coincident within a 2.5 ns window are grouped into events. The events with at least 3 hits within an event time window of 2.5 ns are considered for further analysis in this study, described in Chapter 3. The size of the event time window is chosen to suppress the accidental coincidence events.

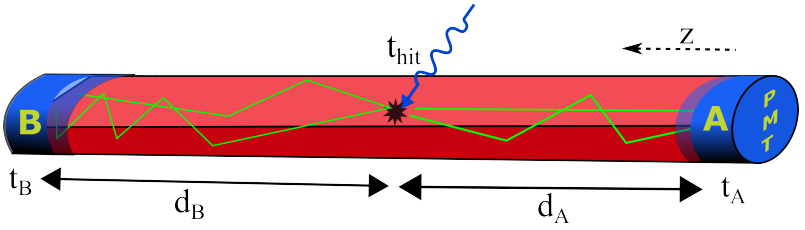

FIGURE 2.5: **A single scintillator module mounted with two photomultiplier tubes at its ends.** The incoming photon interacts with the scintillator and is converted into an electrical signal using PMT on sides A and B of the scintillator. The position (Z_{hit}) and time of interaction (t_{hit}) of gamma at a point in the scintillator are reconstructed from the registration time of the signal at each PMT (t_A and t_B). t_A and t_B are the leading times at the lowest threshold of the electric signal from PMT.

During the reconstruction process, the time of a single γ interaction is estimated from the average of the signal times and time taken by photons to reach PMTs, defined as:

$$t_{hit} = \frac{t_A + t_B}{2} - \frac{d_A + d_B}{2v} \tag{2.1}$$

where $d_A + d_B$ is the length of the scintillator strip, and v is the velocity of light in the plastic scintillator strip [5]. The z position of γ interaction on the scintillator strip is reconstructed from the difference in the registered times of the signal, given as:

$$z_{hit} = \frac{(t_A - t_B) \cdot v}{2} \tag{2.2}$$

The X and Y hit positions are equivalent to the scintillator's placement in X and Y coordinates [79].

Chapter 3

Data processing and event selection

This chapter describes the reconstruction and analysis of data collected from the measurements with the J-PET detector for a CPT symmetry test. The study focuses on identifying ortho-positronium (o-Ps) decays to evaluate the CPT-odd angular correlation operator introduced in the previous Chapter.

3.1 Data preprocessing and monitoring

The data, collected with the experimental setup described earlier, is segmented into three categories based on the pressure within the annihilation chamber during measurement given in Table 3.1. The data from the 356-day measurement (when pressure is less than 1 Pa inside the chamber) is chosen for the CPT-odd angular correlation operator analysis. The vacuum is created inside the annihilation chamber to maximize the production of o-Ps. Data sets collected at other pressure conditions are discussed in a separate chapter of the systematic studies.

TABLE 3.1: The duration of measurements with 3-layer J-PET and spherical annihilation chamber at different pressures inside the annihilation chamber.

Pressure	Measurement duration
1 – 5 Pa	24 days
less than 1 Pa	356 days
101 kPa (Atmospheric pressure)	35 days

As the first step after installation of the o-Ps production chamber in the detector, the source position in the experiment is verified. It is important to have a source position in the center of the detector to avoid spurious asymmetries in the CPT odd angular correlation operator distribution. It is checked by reconstructing the annihilation point of two gamma events from direct annihilation within the collected data. The annihilation point distribution in the transverse (XY) plane for the identified two back-to-back 511 keV gammas from direct e^+ e^- annihilation is presented in Fig. 3.1. The position is estimated to be from the center of the detector in the X-Y plane. The pattern in the

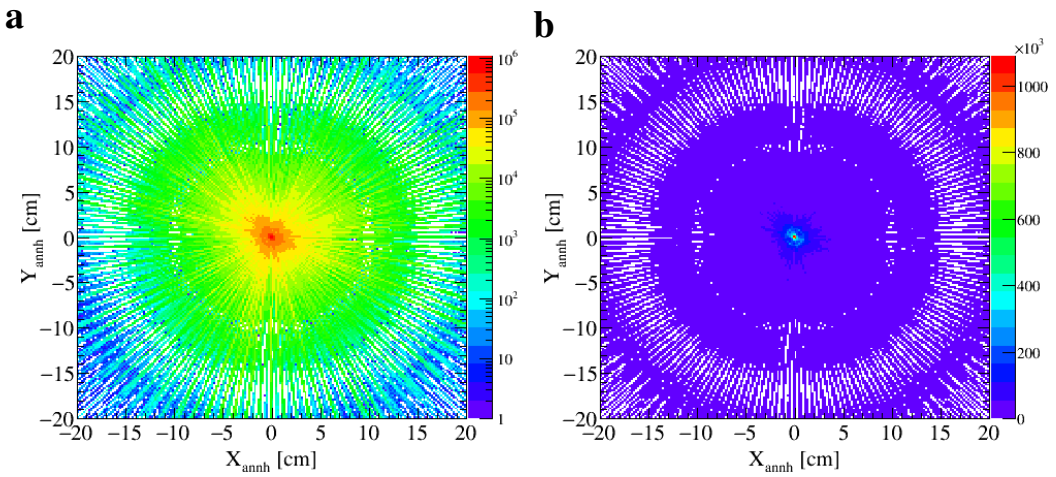

FIGURE 3.1: The distribution of reconstructed annihilation points obtained from $e^+e^- \rightarrow 2\gamma$ events with 511 keV photons from ^{22}Na source with 1.1 MBq activity, in (a) logarithmic and (b) linear scale. The 2γ annihilation points are reconstructed on the Line of Response (LOR) of two 511 keV photons using the position and time of these hits. It is a standard method of reconstructing tomographic images [73].

distribution reflects the uneven 2γ detection efficiency in the transverse plane due to the placement of scintillators in the J-PET detector. The 2γ images were used to monitor the source position and the placement of the annihilation chamber throughout the measurements.

3.2 Analysis procedure for identification of o-Ps $\rightarrow 3\gamma$ events

The identification of ortho-positronium (o-Ps) annihilation events within the detector relies on the selection of at least three gamma-ray interactions ("hits") within a narrow time window. This time window is typically set to 2.5 ns. The size of this window is chosen to be just enough to accommodate differences in TOF-s of photons traveling from extreme points of the chamber to different layers. The analysis procedure is implemented in a two-stage approach. The first stage employs hit-level selection criteria. Individual hits are evaluated based on predefined parameters, and those failing to meet the criteria are discarded. Importantly, this stage does not eliminate the entire event to which the failing hit belongs. The second stage utilizes event-level selection criteria. Here, the complete event is assessed based on the information from all its constituent hits. If any hit within an event fails to satisfy the defined criteria, the entire event is rejected.

3.2.1 Hit-level selection

Hit Multiplicity: The initial stage of the analysis focuses on hit multiplicity. Events containing at least three detected photons (hits) within the 2.5 ns time window are selected for further processing (see Fig. 3.2). This selection criterion significantly reduces the initial data volume, with up to 15% of the original volume of events surviving.

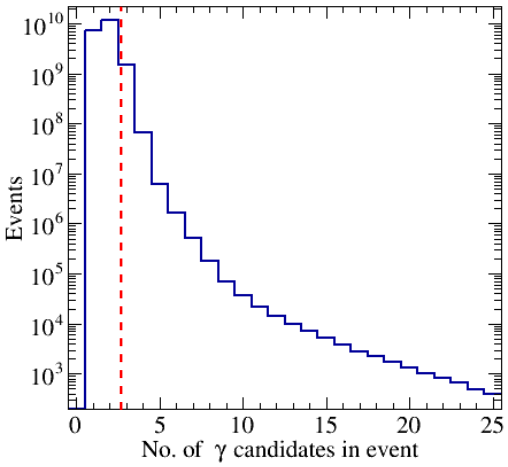

FIGURE 3.2: **Hit Multiplicity.** Distribution of the number of photon interactions (hits) recorded within a single event in a 2.5 ns event time window. Events with a multiplicity of at least three hits are considered for further analysis.

Energy Discrimination via Time-over-Threshold (TOT): In the J-PET detector, the Time-over-Threshold (TOT) method is employed to measure the energy deposited by individual photons [80]. The technique proves valuable in differentiating prompt photons (1275 keV) from annihilation photons originating from the decay of ^{22}Na [81], due to the significantly higher average energy deposition of the prompt photons. The TOT for each hit is defined in Fig. 3.3 (a).

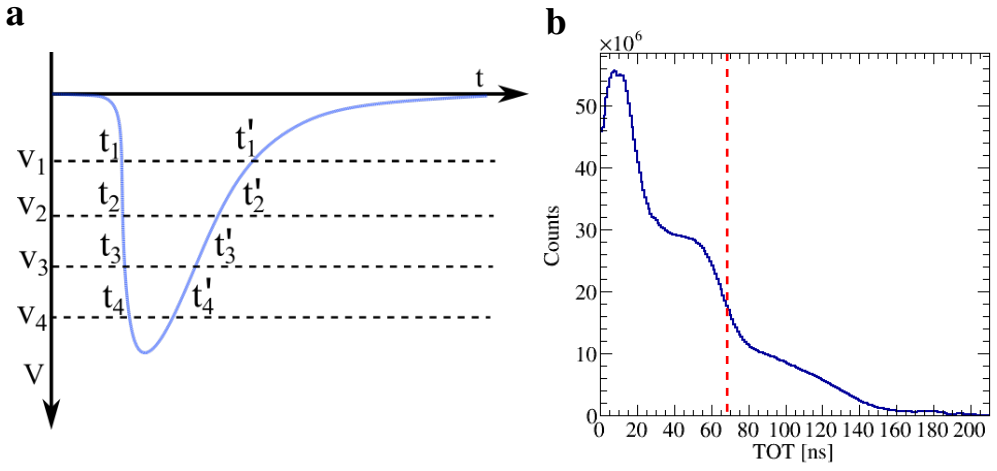

FIGURE 3.3: **Time-over-Threshold (TOT):** (a) An electric signal from the photomultiplier, probed at four different threshold values v_1, v_2, v_3 and v_4 of -30, -80, -190, and -300 mV. The time difference between the trailing (t_i') and the leading (t_i) edge of the signal at each threshold is evaluated. The total TOT of the signal is calculated using $\sum_{i=1}^{4}$ TOT$_i$, where TOT$_i = t_i' - t_i$. The sum of TOT of signals from two PMTs on both ends of a scintillator is taken as TOT of a hit. (b) Experimental distribution of Time Over Threshold (TOT) values for measurement with the spherical annihilation chamber. The values of TOT above 80 ns represent the high energetic de-excitation photons (1.27 MeV) and cosmic rays. In comparison, the region with TOT $<$ 67 ns is used to identify 3γ annihilation from o-Ps (Energy $<$ 511 keV), 2γ annihilation from e^+ e^- (Energy $=$ 511 keV).

Figure 3.3 (b) illustrates the distribution of Time Over Threshold for hits in the detector due to ^{22}Na source. This distribution is a superposition of Compton scattering spectrum, including contributions from 1274 keV de-excitation photons, 511 keV for back-to-back annihilation photons, photons with energy less than 511 kev originating from o-Ps decay, and secondary scattering within the detector. The Compton edge appears prominently around 80 ns for the 1274 keV photons and at 60 ns for the 511 keV photons. Since the energy of the photons form o-Ps decay ranges from 0 to 511 kev, a TOT value of 67 ns and below is used to primary identify the annihilation photons.

Secondary Compton Scatterings: The primary interaction mechanism for gamma rays within the J-PET detector is Compton scattering. During this process, the incident gamma photon deposits some of its energy into the scintillator material, resulting in a scattered photon with lower energy. This scattered photon can subsequently interact again within the detector volume through another Compton scattering event. Due to the sparse, segmented design of J-PET, these secondary interactions can be detected and distinguished from the primary annihilation signal [82]. The exemplary geometric representation of secondary scattered events from o-Ps annihilations is shown in Fig. 3.4.

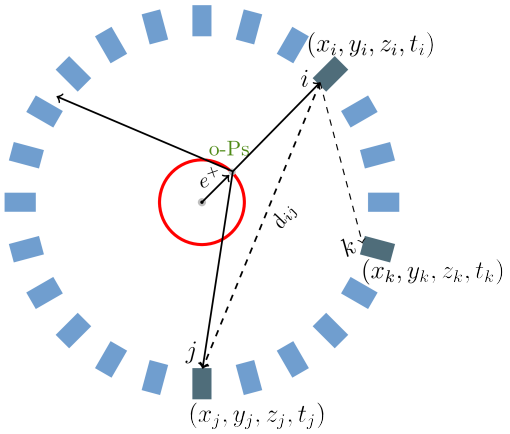

FIGURE 3.4: **Scatter Test.** Schematic representation of the secondary Compton scattered event recorded in the J-PET detector, shown in transverse (cross-sectional) view. The blue rectangles represent the plastic scintillator modules for photon detection. For simplicity, only a few scintillators from a single layer of the detector are shown. At the center of the setup, there is a ^{22}Na source that emits a positron (e^+). The e^+ interacts with a porous aerogel layer coating the walls of a spherical chamber (red circle), where it forms ortho-positronium (o-Ps). The two primary photons from o-Ps (represented by solid arrows) are recorded while one of those photons gets scattered in the scintillator and recorded as a third hit in the neighboring scintillator module of the detector (dashed arrow). The d_{ij} represents the distance between the hit positions for a pair of hits in three hit events defined in Equation 3.1. The scintillators in dark color represent the ones where photon gets registered in the detector.

One major source of background in the study that mimics the three-photon signature of ortho-positronium (o-Ps) annihilation is secondary Compton scattering of 2γ and 3γ annihilation photons. To address this, a scatter test is implemented to exclude scattered photons based on the following function:

$$\delta d_{ij} = ||\vec{r_i} - \vec{r_j}| - c|t_i - t_j|| \tag{3.1}$$

where c denotes the speed of light in vacuum (29.98 cm·ns^{-1}), t_i and $\vec{r_i}$ denote registered hit times and positions for hits i and j. It involves the time of flight for i_{th} and j_{th} hits and the distance between these recorded interactions, as shown in Fig. 3.4.

It is based on the hypothesis that for the pair of primary photons recorded as hit i and j the time of interaction should be close as they all propagate from the chamber to the scintillators. The d_{ij} for such pairs are expected to be relatively large which results in getting values of δd_{ij} far greater than zero (shown in Fig. 3.4). For a pair of primary and scattered hits (i and k in Fig. 3.4) the function represents the hypothesis that a photon propagating directly between i and k should have d_{ij} equal to $(t_i - t_j)\cdot c$. Hence δd_{ij} should approach zero for a pair with primary and its secondary scattered photon.

The δd_{ij} value is calculated for all possible hit pairs in an event containing 3 or more hits which can be δd_{12}, δd_{23}, δd_{24}, etc. Such a distribution of δd_{ij} for all possible combinational pairs is given in Fig. 3.5 (a).

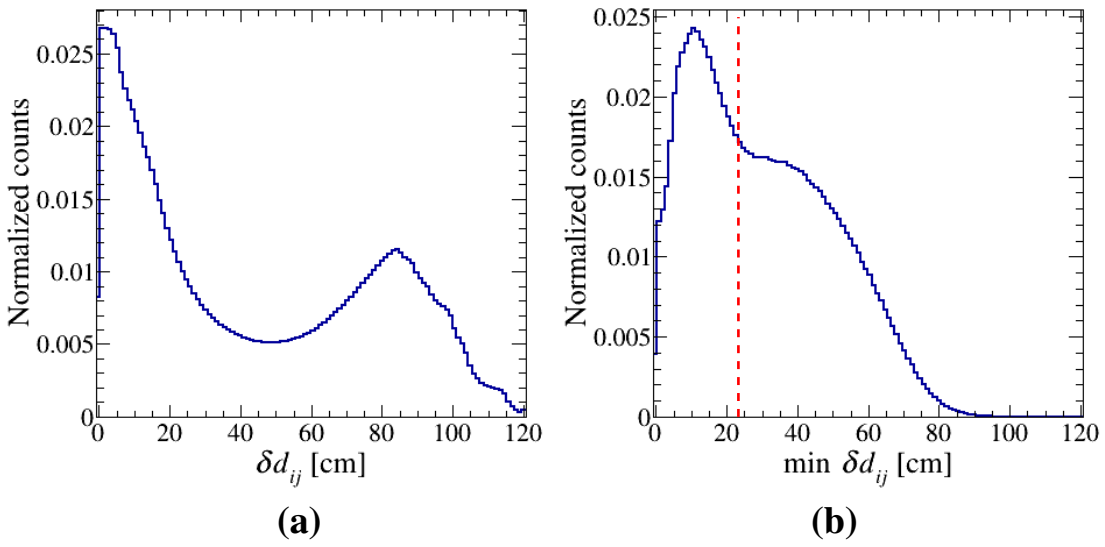

FIGURE 3.5: **Removal of secondary Compton scatterings.** (a) Distribution of δd_{ij} plotted for all the combinations of hit pairs in an event with a hit multiplicity of at least three. (b) Distribution of the minimum value of δd_{ij} for a single hit pair in a given event. The region near zero is marked as events of secondary Compton scatterings in the detector which are discarded by taking events with min $\delta d_{ij} > 23$ cm.

As per the hypothesis of the function, the events containing at least one recorded secondary scattered photon as well as its primary photon the value of δd_{ij} should approach zero. This means that for these hit pairs the value of δd_{ij} should be comparatively smaller than the hit pairs from primary photons. The minimum of the absolute values of δd_{ij} for a single event is chosen as shown in the distribution in Fig. 3.5 (b). The minimum δd_{ij} is plotted for only three-hit events. The reference cut value around the valley-like region at 23 cm is chosen to remove scattered hits in an event. In case a pair of hits with $\delta d_{ij} < 23$ cm is identified in an event, the later hit is removed from the

event considering it as a secondary scattered photon. It effectively reduces the event hit multiplicity. The reference cut value is not decided based on the δd_{ij} distribution for all the hits pairs in a single event (Fig. 3.5 (a)) which is around 50 cm as it might end up losing the hits of interest.

From now on wards, in the event, those hits are accepted where hit pairs have $\delta d_{ij} > 23$ cm and the fastest hit in the hit pairs with $\delta d_{ij} < 23$ cm. For further analysis, events with only three hits are considered which is explained in the following section.

3.2.2 Event-level selection

The previous hit-level selection removed hits from events with higher multiplicities, potentially reducing them to 3-hit events. There could be another approach of selecting the three-hit events only at first glance and applying similar selection criteria but all at the event level. The study is performed where these two methods are compared and it results that the approach of eliminating hits but restoring the event from which the hit is eliminated, results in a gain in efficiency for 3-hit events by 8%. The MC simulations are also used to prove that this approach of eliminating hits can recover 8% of event which would otherwise be rejected if we have required 3-hit events only from the beginning.

Following the hit-level selection, the events with only three-hit multiplicity are considered for further processing. A three-dimensional annihilation point reconstruction is performed for the selected three hit events. This reconstruction employs the trilateration method as described in [83]. The method calculates the intersection point of three spheres centered on the positions of the three detected photons, assuming they lie within a single plane. The hit positions and times are used as input, and the method not only estimates the annihilation point but also the corresponding annihilation time. It is a unique reconstruction of three-photon annihilations which is only attempted at J-PET [8]. The resolution of the reconstructed 3γ vertex achieved with this method ($\approx$ 8 cm) is sensitive to the hit timings. It is estimated that 29% of the total selected three-hit events are properly reconstructed using trilateration reconstruction.

Once the annihilation point of 3γ is determined, the direction of photons' momenta can be calculated and angles between them can be used to obtain the energy of the annihilation photons. The momenta direction of annihilation photons is estimated from the reconstructed annihilation vertex and the corresponding hit position in the scintillator.

3.2.2.1 Energy and angular distribution of 3γ

In the J-PET data, there is no information on the energy of the incoming photon as the photon deposits only a varying part of its energy via the Compton scattering effect. However, it is possible to reconstruct the energy of three γ from o-Ps decays due to the conservation of momentum and energy [84]. The energies can be expressed as a function of angles between the photons' momenta (θ_{12}, θ_{23}, θ_{13}) and are given:

$$
\begin{aligned}
E_1 &= -2m_e \frac{-\cos\theta_{13} + \cos\theta_{12}\cos\theta_{23}}{(-1+\cos\theta_{12})(1+\cos\theta_{12}-\cos\theta_{13}-\cos\theta_{23})}\,, \\
E_2 &= -2m_e \frac{\cos\theta_{12}\cos\theta_{13} - \cos\theta_{23}}{(-1+\cos\theta_{12})(1+\cos\theta_{12}-\cos\theta_{13}-\cos\theta_{23})}\,, \\
E_3 &= 2m_e \frac{1+\cos\theta_{12}}{1+\cos\theta_{12}-\cos\theta_{13}-\cos\theta_{23}}\,,
\end{aligned}
\tag{3.2}
$$

where m_e is the mass of electron. The energies of three photons are estimated using Equations 3.2.

The reconstructed vertex of 3γ annihilations must lie in a plane spanned by the three hits. There can be circumstances where the reconstructed vertex lies outside the triangle spanned by the hits, see Fig. 3.6. These kinematically infeasible reconstructed configurations lie within a plane and are an artifact of poor reconstruction. Such events are excluded from further analysis by requiring all photons within an event to possess positive energy values.

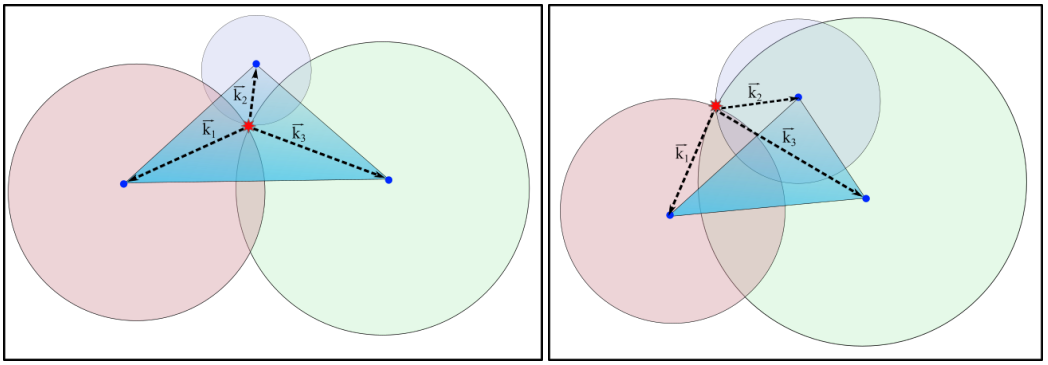

FIGURE 3.6: **Reconstruction of annihilation point.** Two different cases of reconstructed annihilation point of 3γ. The three photons from o-Ps decay lie in one plane given by blue triangles. The red point represents the reconstructed annihilation point using the trilateration method. (a) The annihilation vertex should lie in a triangle spanned by three hits in case of proper reconstruction. (b) The circumstances where the reconstructed annihilation vertex lies outside the triangle. The intersection of the three circles is the reconstructed annihilation vertex of 3γ which is the basic principle of the trilateration method [83].

Identification and elimination of background from 2γ annihilations: Significant background in this study is the two back-to-back photons from p-Ps and direct annihilation from the ^{22}Na source. The pair of photons from p-Ps and direct annihilation have a collinear momentum. To identify these background events two variables are defined based on the properties specific to 2γ annihilation events. These include the angles between photons' momentum and the distance between the hypothetical 2γ annihilation point and the center of the detector.

The first variable useful to distinguish a pair of photons with back-to-back momenta uses the angles between photons' momenta calculated from its position and detector center as shown in Fig. 3.7 (a). The angles θ_1, θ_2, and θ_3 are calculated for three hit pairs in a three-hit event from the detector center. Assuming that if the hits from direct and p-Ps annihilations are recorded in the detector then the angle between their photons would be 180° from their point of annihilation. To

identify the two hits from such a background in a three-hit event a sum of the two smallest such angles must be considered.

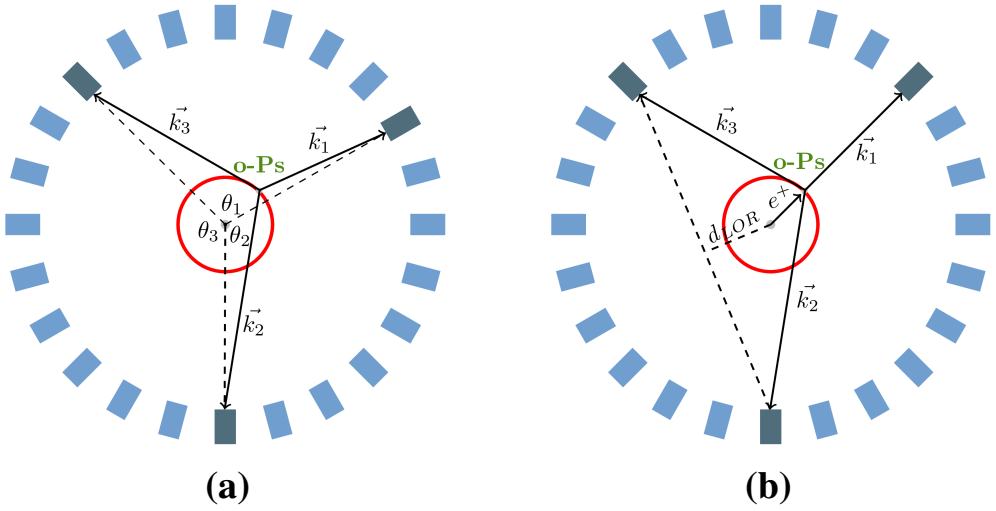

FIGURE 3.7: **Angle sum and min d_{LOR}.** (a) Schematic representation of the three relative angles θ_1, θ_2, θ_3 between photons from o-Ps decay calculated from the center of the detector. (b) Representation of the minimum distance between the hypothetical two-photon annihilation point estimated for two hits in a three-hit event and the center of the detector. In this setup, the blue rectangles represent the plastic scintillator and the ones in dark colors represents where photon gets recorded in the detector. For simplicity, only a few scintillators from a single layer of the detector are shown.

In a three-hit event, if photons from p-Ps or direct annihilation are identified along with other potential hits e.g. from secondary scattering or random coincidences, the 2γ annihilation point reconstruction would be useful to suppress this kind of background. These events would lie in the region where annihilation could happen. The 2γ annihilation point can be reconstructed using the standard tomographic method, described in Fig 3.1. To make use of this fact an attempt to identify the right pair of photons by calculating the 2γ annihilation point for each pair of hits in a three-hit event. The distance from this annihilation vertex (which would be on the Line of Response of 2γ annihilations) to the detector center is estimated for each pair termed as d_{LOR} in Fig 3.7 (b). The d_{LOR} value would be comparatively smaller for hits from 2γ annihilations than the signal events. The minimum of d_{LOR} values is considered as another variable to identify this kind of background.

It is to be noted that the angles for this variable are not calculated from the reconstructed 3γ annihilation vertex but rather from the center of the detector where the source is positioned. The representation of these two types of angle estimation is given in Fig. 3.8. Due to the conservation of momentum in o-Ps $\rightarrow 3\gamma$ decays, the sum of its two smallest angles would always be greater than 180°. It would be difficult to identify the events from 2γ annihilation that can mimic the o-Ps signal events in this study, given in Fig. 3.9. A major fraction of direct annihilation occurs at the source, so it is considered from the center as given in Fig. 3.10.

The sum of the two smallest angles between the momenta of registered annihilation photons is calculated to identify such events. Furthermore, 2 gamma annihilation points are estimated for

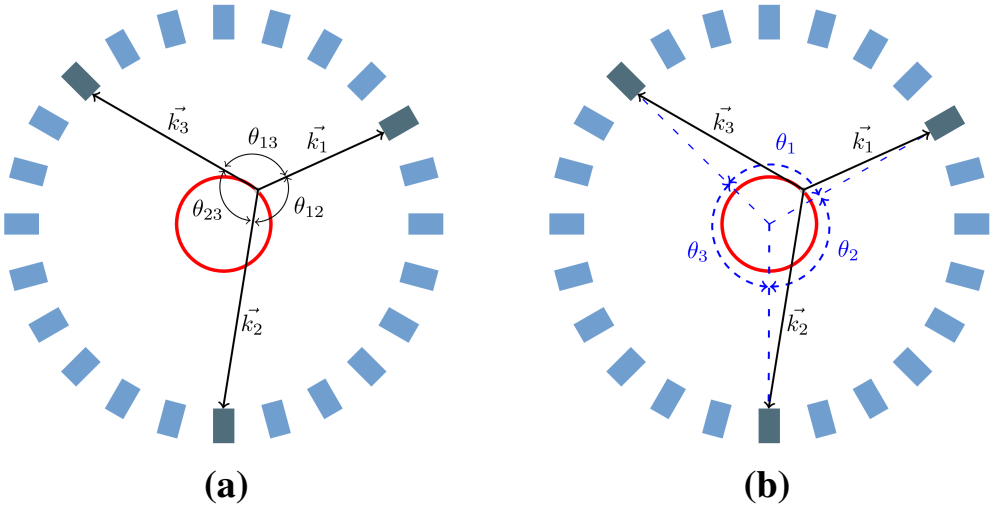

FIGURE 3.8: **Representation of the angles between photons.** (a) Schematic representation of the three relative angles θ_{12}, θ_{23}, θ_{13} between photons from o-Ps decay calculated from its reconstructed decay vertex. (b) Representation of angles θ_1, θ_2, θ_3 between photons from o-Ps decay calculated from the center of the detector.

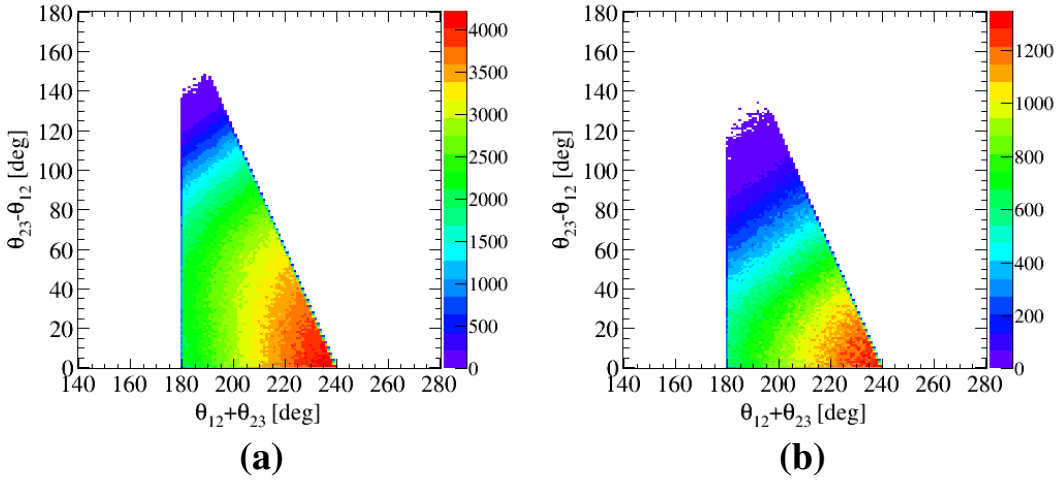

FIGURE 3.9: **The relative distribution of the difference and sum of two smallest angles between photon momenta.** The angles are calculated from the reconstructed 3γ annihilation vertex to the photons' interaction position in the detector, as represented in Fig. 3.8 (a). Due to momentum conservation in ortho-positronium (o-Ps) decay to three photons, the analysis is restricted to the region where the sum of the two smallest angles is greater than 180 degrees. This distribution is not suitable for background suppression from two-photon (2γ) annihilation events because their distribution significantly overlaps with the signal from o-Ps decay. The distribution for the three-hit events (a) before and (b) after the final selection criteria on $\theta_1 + \theta_2 > 204°$ (angles measured relatively from detector center). It is important to note that the top-most edge of the triangular distribution in (a) and (b) exhibits a non-uniformity. This is a consequence of eliminating events originating from Compton scattering before plotting the distribution.

every pair of hits for a three-hit event, which would lie somewhere on its Line of Response (LOR) as shown in Fig. 3.7. The shortest distance between each estimated annihilation point and the detector center (termed min d_{LOR}) is computed. These values are then plotted alongside the sum of the two smallest angles in a distribution, as shown in Fig. 3.11. Events from direct annihilation

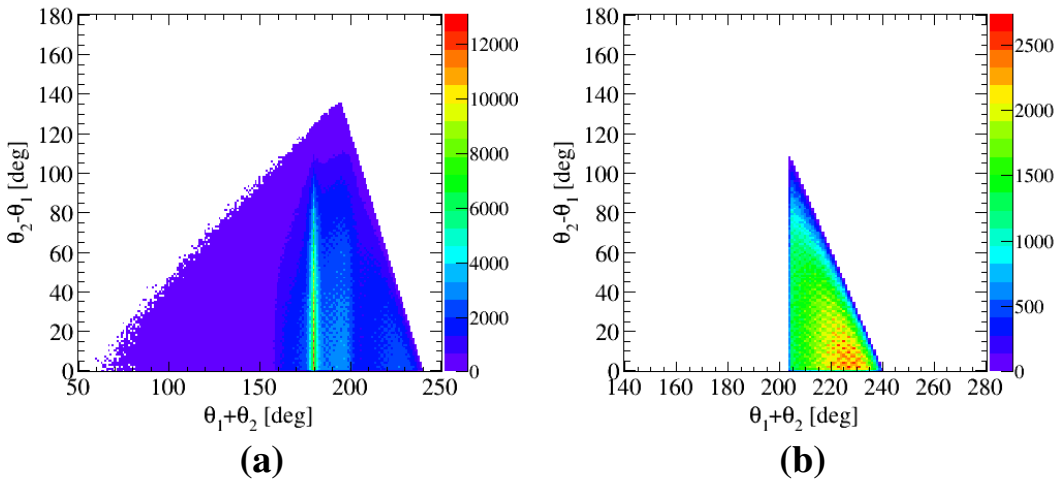

FIGURE 3.10: **Distribution of the difference and sum of two smallest angles between photons interaction points in the scintillator and the detector center.** The angles are calculated from the center of the detector system (shown in Fig. 3.8 (b)) to identify the events with two back-to-back photons of 511 keV energy in a three-hit event. (a) represents an exemplary distribution for three-hit events after eliminating the events with negative reconstructed energy of photons. The maximum concentrated region at $\theta_1 + \theta_2 = 180°$ is due to the events with 2γ from direct annihilation with opposite momentum. The band-like region from $160° < \theta_1 + \theta_2 < 200°$ represents the events from 2γ annihilations including the detection of primary and its secondary Compton scatterings. The events from o-Ps annihilations lie above $\theta_1 + \theta_2 > 180°$ due to momentum conservation. (b) The similar distribution after the last selection criteria on $\theta_1 + \theta_2 > 204°$ for the selection of o-Ps $\rightarrow 3\gamma$ events.

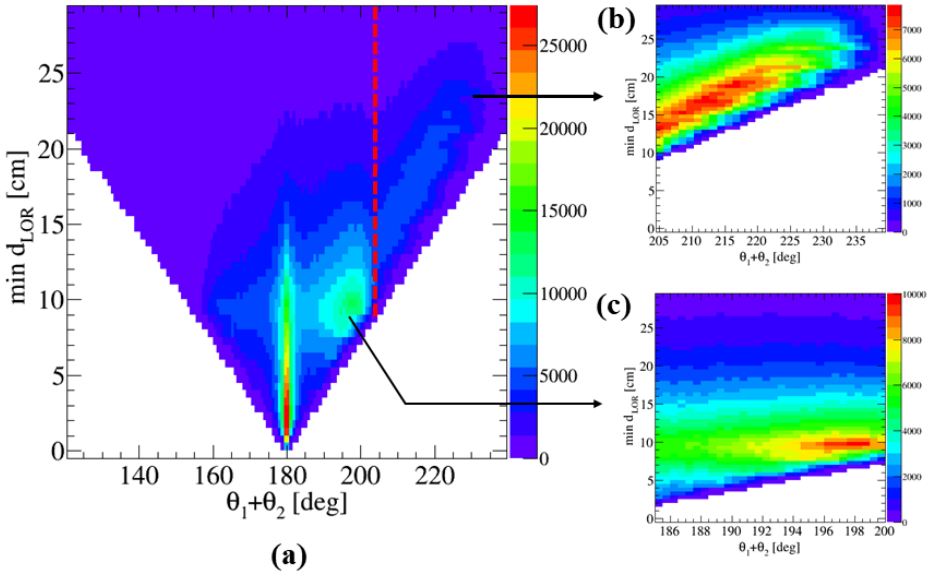

FIGURE 3.11: **Signal selection.** (a) Distribution of minimum distance between source position and hypothetical 2γ annihilation point on LOR vs. sum of two smallest angles between photons' momenta for data for the selected three annihilation photons. The region $\theta_1 + \theta_2 > 204°$ is selected for the signal events from o-Ps $\rightarrow 3\gamma$. The enhanced view of this region is given in (b). The maximum concentrated region at 180° in (a) originates from the 2 photon annihilation events from the source. The enhancement near $\theta_1 + \theta_2 = 195°$ to 200° is due to the 511 keV annihilations from p-Ps events, shown in (c).

are anticipated to cluster in the region with a small min d_{LOR} value and a sum of angles close to 180°. The events from p-Ps annihilation are concentrated around the region of 200° angles. Events falling within this designated region $\theta_1 + \theta_2 > 204°$ are the identified o-Ps events for the CPT symmetry test.

Detailed comparisons between the experimental data and Monte Carlo simulations at these specific cut values can be explored in Chapter 4.

3.2.3 Identification of o-Ps events

To validate the existence of the o-Ps events in the final data sample the decay time of the produced positronium is estimated. It is taken as the difference between the emission time of the de-excitation photon and the reconstructed 3γ annihilation time for the identified o-Ps. The de-excitation photons, selected based on TOT greater than 67 ns (see Fig. 3.3 (a)), are paired with the identified o-Ps events in a given time window. The time difference between each possible pair of de-excitation photons and o-Ps events is shown in Fig. 3.12. The exponential decay of the time difference distribution is due to the longer lifetime of o-Ps. The flat random coincidence background in the distribution comes from the pairs where o-Ps and de-excitation photons do not correspond to a single event.

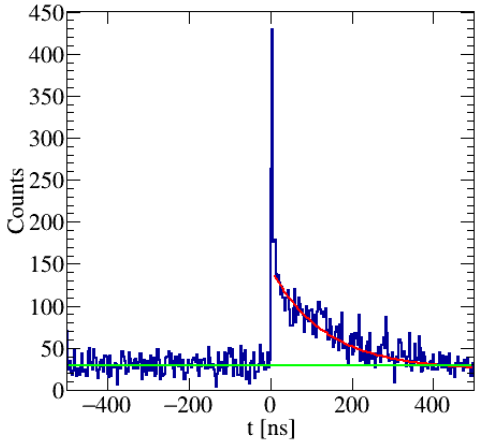

FIGURE 3.12: **Lifetime.** Difference of emission times between the de-excitation photon and 3γ recorded in the detector. A long-lived component with a decay constant of approximately $\tau \sim 138$ ns is visible above a flat random coincidence background (green line), which extends symmetrically to both positive and negative time differences, marking the identification of o-Ps events. The distribution is fitted with an exponential function (red color) over the range from 6 ns to 500 ns.

For the identified o-Ps events, the angles between photons' momenta and their energies using Equation 3.2 are calculated and presented in Fig 3.13.

The reconstructed annihilation point of o-Ps $\rightarrow 3\gamma$ events is shown in Fig. 3.14.

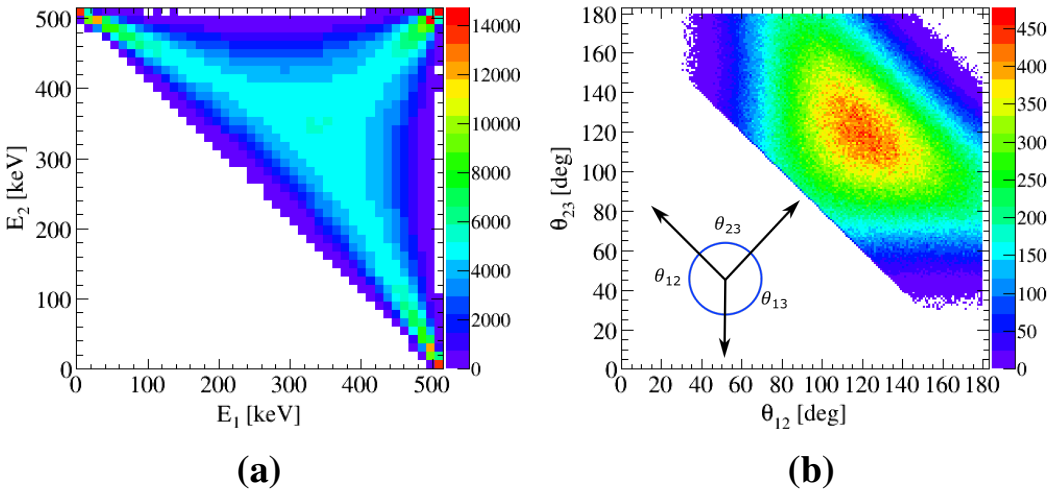

FIGURE 3.13: **Angle and energy of photons from o-Ps annihilations.** Distribution of (a) energies (Dalitz plot) and (b) angles between momenta of photons from o-Ps decays. The angles are calculated from the reconstructed three gamma annihilation vertex, as shown in Fig. 3.8 (a).

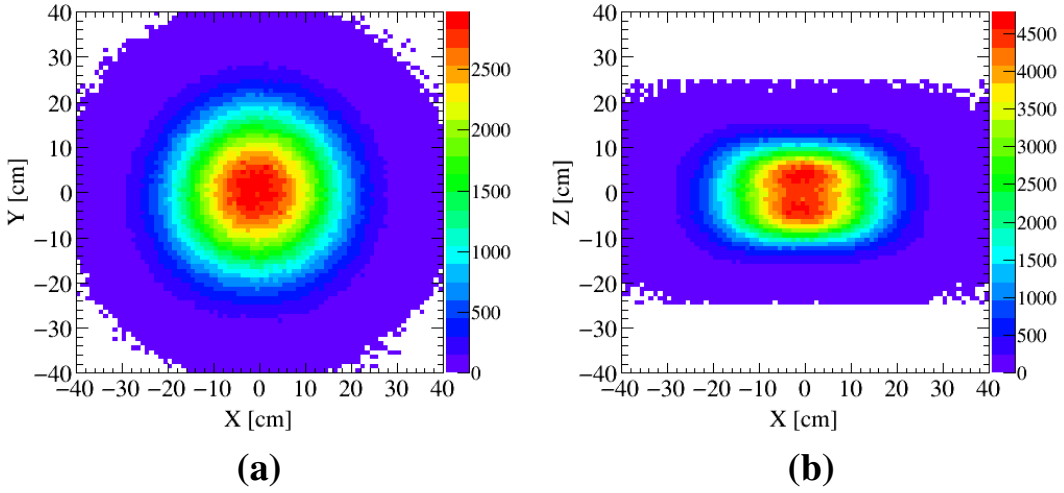

FIGURE 3.14: **Distribution of o-Ps annihilations.** The projections of reconstructed 3γ annihilation vertex of the identified o-Ps events using the trilateration method in (a) XY and (b) XZ reference plane of the detector.

3.3 Study of CPT-odd angular correlation operator with J-PET

The decaying o-Ps state is characterized by its spin (S) along a specific axis and the momenta (k_i) of the three annihilation photons in its final decay state. The CPT-sensitive angular correlation operator constructed from these observables is defined as:

$$\cos\theta = \vec{S} \cdot \frac{(\vec{k_1} \times \vec{k_2})}{|\vec{k_1} \times \vec{k_2}|} \tag{3.3}$$

where momenta are ordered as $|\vec{k_1}| > |\vec{k_2}| > |\vec{k_3}|$. It represents the angular correlation between the o-Ps spin and normal to the plane defined by the momenta of the three annihilation photons. The pictorial representation of the angle between spin and normal to the decay plane of o-Ps is shown in Fig. 1.2 in Chapter 1. The spin axis of o-Ps is defined along the direction of flight of the positron due to the longitudinal polarization of positrons from β^+ decay [85]. It is taken as a unit vector from the positron source position to the annihilation point of o-Ps on an event-by-event basis. The momenta of annihilation photons are estimated from the reconstructed hit positions of the three gamma interactions in the scintillator and the event's reconstructed annihilation point. The schematic view of a fully reconstructed o-Ps $\rightarrow 3\gamma$ annihilation event in the J-PET detector is represented in Fig. 3.15 (a).

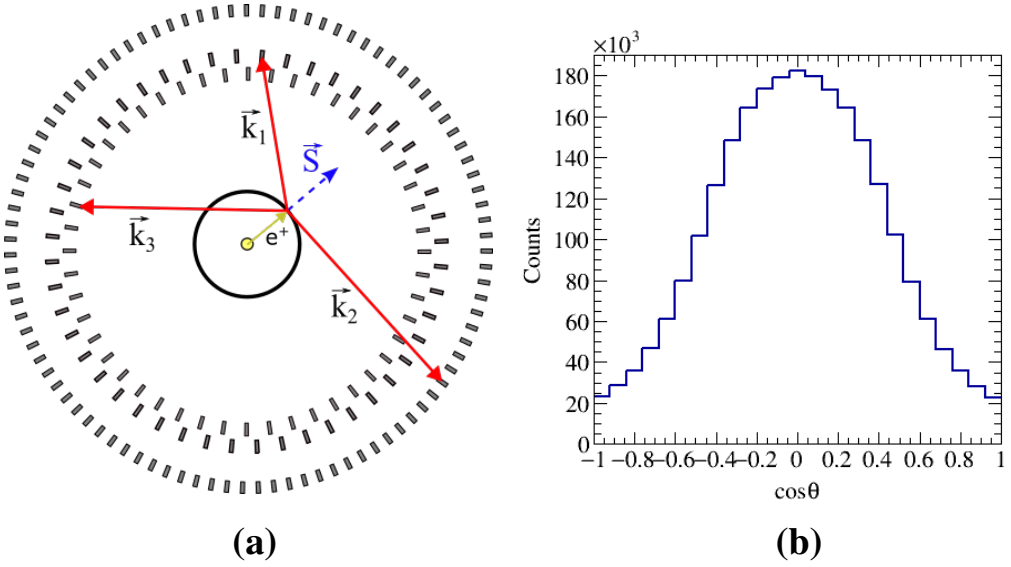

FIGURE 3.15: **CPT-violation sensitive angular correlation.** (a) Visualization of the o-Ps decay on the walls of the spherical annihilation chamber and detection of its annihilation photons in the different layers of the J-PET detector. (b) The distribution of the CPT-odd operator defined in equation 3.3 for the identified 2.8 million o-Ps events in the measurement with source activity 1.1 MBq.

For the identified signal events from two different sets of measurements with the J-PET detector, the angular distribution of $\cos\theta$ is plotted in Fig 3.15 (b). The expectation value of the CPT odd operator is taken as the mean of the CPT odd angular distribution. The operator's non-zero expectation value would give the symmetry violation's signature. More details on the shape of this distribution and its dependencies on certain factors are given in the coming chapters.

TABLE 3.2: The number of identified o-Ps events after the analysis criteria from the two J-PET measurements analyzed in this work (summarized in Table 2.1) for the CPT symmetry test

Measurement time (days)	Source activity (MBq)	No. of identified o-Ps
78	1.1	2.8×10^6
278	4	4.5×10^7

The number of o-Ps events from the J-PET run measured at different source activities is listed in Table 3.2. The identified o-Ps events are around 2.8 million from 78 days of measurement with

1.1 MBq source activity and 45 million signal events from 278 days of measurement with 4 MBq source activity. In total, this thesis identifies 47.8 million o-Ps events from a 3-layer J-PET detector measured over 356 days using a spherical annihilation chamber.

Chapter 4

A Simulation study

Understanding the impact of background events on the measured asymmetry in the CPT-odd angular correlation operator is crucial for CPT symmetry violation searches. A thorough background characterization using Monte Carlo simulations is essential to ensure reliable extraction of the CPT-violating signal. This section discusses the MC simulations for a J-PET detector equipped with a spherical annihilation chamber within the framework of Charge-Parity-Time (CPT) symmetry investigations. The primary objective is to assess and quantify potential background contributions in the final experimental data that could introduce false asymmetries in the CPT-odd angular correlation operator for ortho-positronium (o-Ps) decays. It also includes the different checks and optimization done while comparing the angular correlation operator from experimental data to its MC simulations.

4.1 Introduction to J-PET Monte Carlo Geant4 software

The MC simulations are implemented using a Geant4-based package specifically developed for the J-PET detector [86]. The J-PET MC simulation package used by the J-PET collaboration already included the description of the 3-layer detector used in this work. The positronium production and annihilation setup, being unique to this experiment was implemented in the simulations by the Author. The setup implemented in the simulations is an accurate reproduction of the experimental setup with minor simplifications. The visualization of the detector geometry in the simulations is shown in Fig 4.2 (a).

The simulation package generates photons originating from various annihilation channels, including p-Ps, o-Ps, and direct annihilation. Additionally, a single de-excitation photon is simulated for each generated event. It incorporates the fraction of 3γ (three-photon) and 2γ (two-photon) annihilations for direct annihilation, p-Ps annihilation, and o-Ps annihilation via the pick-off process. The ratio of 3γ to 2γ annihilation is directly linked to the positronium production material properties. This ratio is estimated based on the characteristic mean lifetime of each annihilation type within the specific material medium. Notably, the probability of direct annihilation resulting

in 3γ is approximately 1/378, whereas, for p-Ps annihilation, it is zero [77]. The 3γ contributions from o-Ps annihilation are estimated by calculating the ratio of its mean lifetime in the medium (τ_{medium}) to its vacuum lifetime (τ_{vacuum}). The probability of 2γ annihilation for a given decay channel is simply 1 minus the corresponding 3γ probability. The annihilation vertex point of γ from any of these decay channels is simulated based on the effective positron range in a given material. The target material used in this study is porous silica aerogel (SiO_2) on the inner walls of the annihilation chamber and the Kapton foil wrapped around the ^{22}Na source placed at the center of the chamber. The physical processes of generated photons after interaction with a medium and its path are tracked by a Livermore Polarized electromagnetic model list from the standard Geant4 simulation package [87].

The generated events from simulations are passed through the steps of reconstruction to obtain the simulated hits and events which would mimic the data as close as possible. At the level of generation, the MC simulations account for Compton interactions of photons, their angular distributions, the deposited energy in a material, the position and time of interaction in the detector (termed as hit time and hit position), a four-momentum vector of photons, multiple scatterings of photons in the detector, etc. Additional information like hit type i.e. primary, secondary Compton scattered or de-excitation photon can also be extracted which is useful for the background evaluation in simulations. Each generated hit is reconstructed by applying experimental smearing resolutions for hit position (σ_z = 2 cm) and time (σ_t = 300 ps). The threshold on deposited energy (E_{thr}) for each hit is kept to be 30 keV. The events formed after grouping the hits are distributed in time depending upon the activity used. The reconstructed events are processed through analysis steps of selection criteria of identification of ortho-positronium similar to the experimental data, explained in Section 4.2. This whole procedure involved in J-PET MC simulations is briefly given in Fig. 4.1.

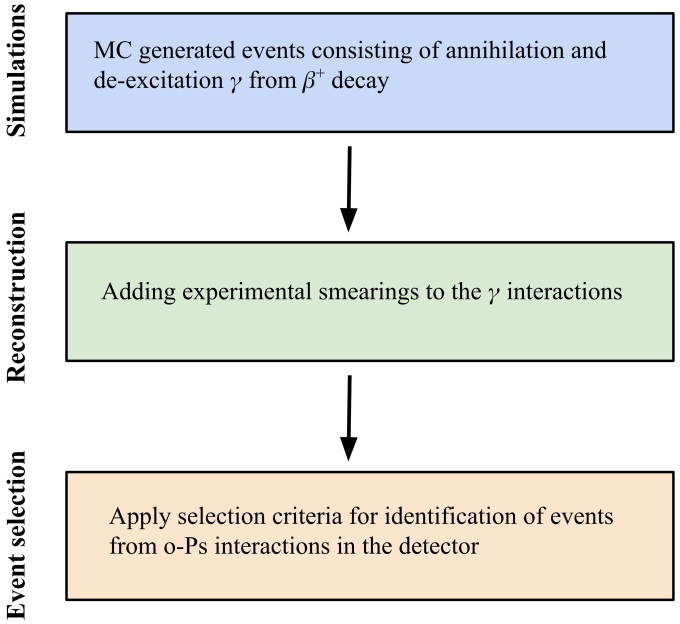

FIGURE 4.1: **Analysis chain for the simulated events.**

4.2 Analysis steps of o-Ps events selection from MC simulations

The MC reconstructed data is processed through identical analysis steps (except for the condition on δd_{ij} for scatter test) as done for the experimental data, described in Section 3.2. In simulations, there is direct information on energy deposited by a single hit in the scintillator instead of the Time over Threshold (TOT) method in the experimental data. As a result, the selection dependent on the energy of the different types of annihilation and the prompt photon is done using energy deposited by hits rather than estimating their energy equivalent TOT values.

J-PET studies on the relationship between photon energy deposition and its equivalent TOT have been conducted for 511 keV annihilation photons [80]. Achieving a universal energy deposition to TOT conversion remains challenging and was beyond the scope of this thesis.

The whole analysis scheme is divided into two sections:
Hit-level selection: The pre-refinement analysis steps include the criteria for selecting the hits based on their energy, position, and time properties. As in the data, the analysis started by applying the selection criteria to the energy deposition of hits based on the position of the Compton edges. The energy threshold value set in the simulations is 30 keV, and the hits with energy deposited less than 340 keV are chosen, as shown in Fig. 4.2 (b). The lower threshold value of 30 keV corresponds to the threshold applied in the Data Acquisition system based on energy deposition by photons in plastics to reduce electronic noise where the signals below this threshold are rejected.

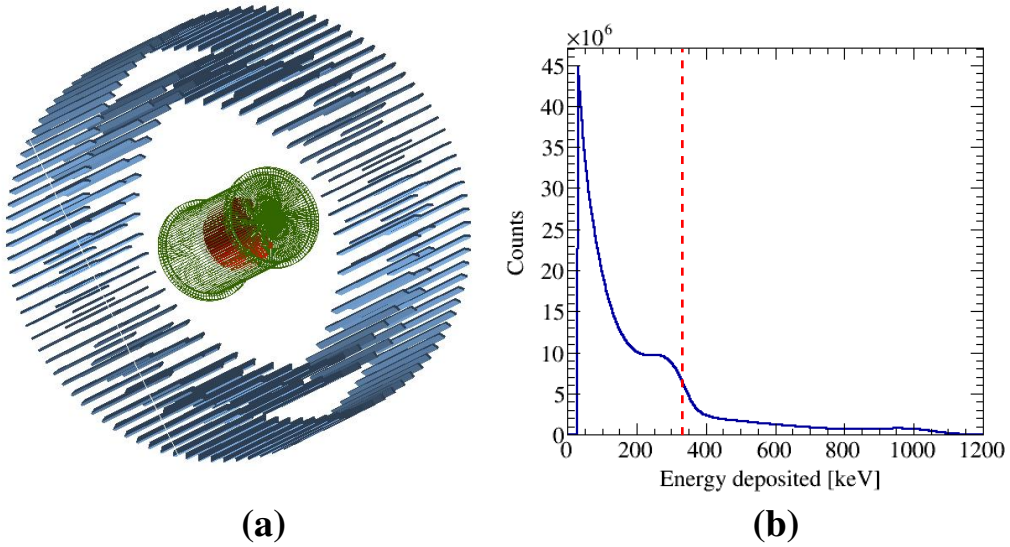

FIGURE 4.2: **Hit-level selection in MC simulations.** (a) Visualization of the 3-layer J-PET detector geometry with spherical annihilation chamber in Geant4. (b) Distribution of energy deposited by gamma quanta in the plastic scintillators. The Compton edge from 200 to 340 keV corresponds predominantly to the annihilation photons, while the high energy (0.8-1.2 MeV) is deposited by the de-excitation photon. For this study, the annihilation photons are chosen with the energy deposited less than 340 keV. The highest peak in the distribution starts from 30 keV, the lower threshold set on energy deposition in simulations.

The scatter test is performed as another selection criterion to remove the secondary Compton scatterings in the detector as explained in Section 3.2. The selection cut value on the δd_{ij} for

simulations is decided in a similar manner as done in the experimental data. The cut value is chosen at 35 cm based on the position of valley like structure, shown in Fig. 4.3 (a). While in the experimental data, it is kept at 23 cm due to difference in the peak position. The influence of this cut value on final result is checked as source of systematic and discussed in more detail in Chapter 5.

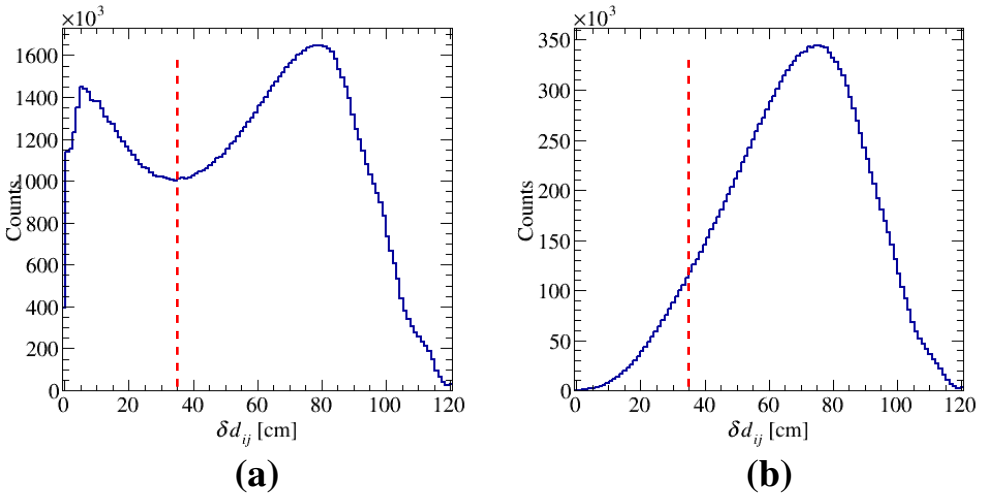

FIGURE 4.3: **Scatter Test:** The distributions representing the discrepancy between the distance traveled and the time of flight for every pair of recorded photons in a selected event plotted for (a) total MC simulated events and (b) for o-Ps $\rightarrow 3\gamma$ signal events. The hit pairs with $\delta d_{ij} > 35$ cm and the fastest hit in the hit pairs with $\delta d_{ij} < 35$ cm are selected for further analysis.

Event-level selection: The other part of the analysis is event-based where the events with three hits are selected similarly as done in the data. At this stage in simulations, these three hit events are classified into signal and the possible background components as described in Section 4.3. In the Geant-4-based J-PET MC simulations, the information of the original type of simulated events is retained along with the simulated hits and events so that different background channels can be identified in the selected event sample at each analysis stage.

The signal and the three hit background events are processed through further selection analysis criteria. It includes the trilateration reconstruction of the annihilation vertex of three photons. It is a criterion on the event topology using the time and position information of three recorded hits. The relative angle between the three annihilation photons and the corresponding photons' energy is estimated based on Equations 3.2. Similarly, as in the case of experimental data (given in Section 3.2.2), events with negative reconstructed photon energies, indicating poor event reconstruction, are eliminated. The events after the last selection criteria on $\theta_1 + \theta_2$ and the minimum d_{LOR} are taken as the final signal and the background for further study. The event-based selection cut values in MC are the same as the ones in the experimental data. The comparison of simulations to the experimental data is done in the further sections of this chapter.

4.2.1 Comparison with the experimental data

The MC simulations are verified at different stages of the analysis by comparing them with the experimental data [88]. The distribution of a sum of the two smallest angles between photons versus a minimum of d_{LOR} are compared for the selected three-hit events after the hit-based selection criteria as shown in Fig. 4.4. A similar distribution is explained in the previous chapter in Fig. 3.11. The maximum concentrated region around $\theta_1 + \theta_2 = 180°$ in experimental data (Fig. 4.4 (a)) is due to the direct annihilations from ^{22}Na source, while in the simulations, this background channel is not simulated which results in missing of such region in total simulations in Fig 4.4 (b). A more detailed background study is shown in the next section.

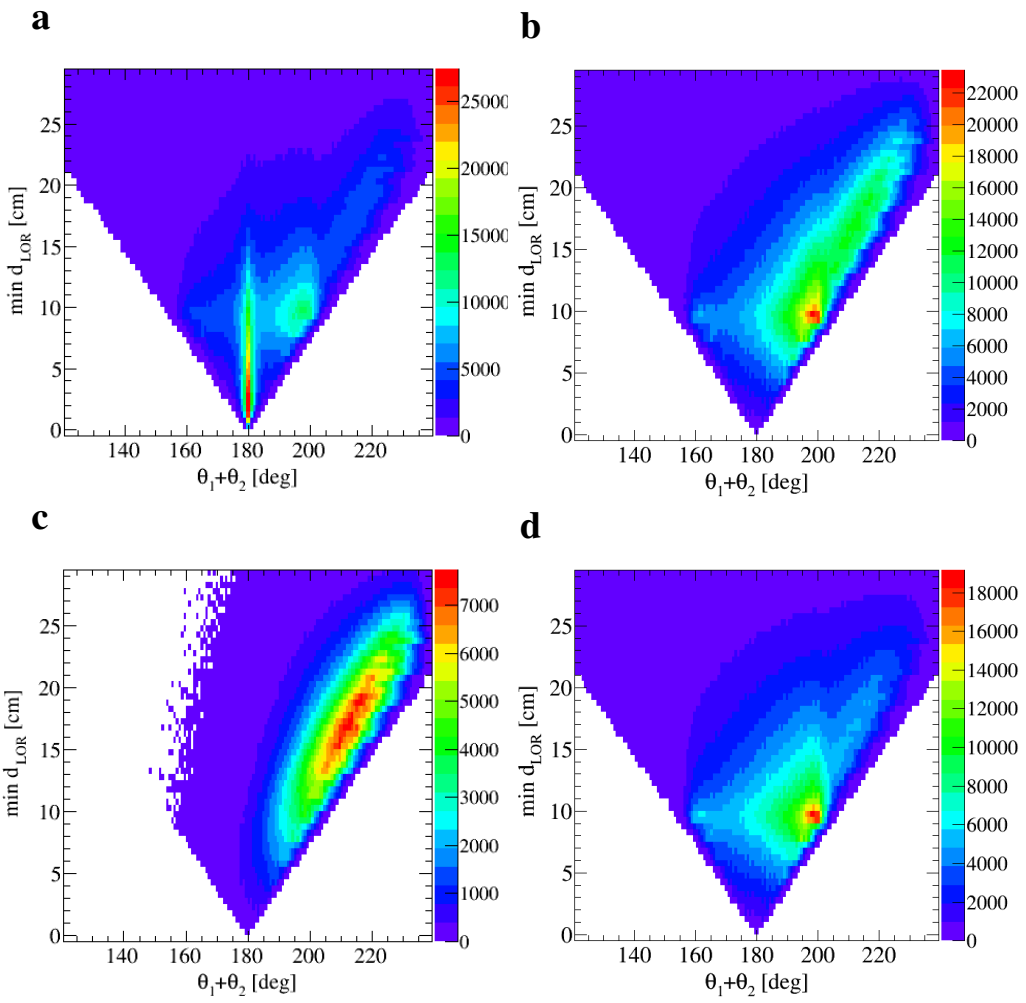

FIGURE 4.4: **Experimental data and MC simulation comparison.** The distribution of the sum of two smallest angles vs. min d_{LOR} for 3γ events in the case of (a) the experimental data, (b) all MC simulated events including the background and signal, (c) only simulated signal events from o-Ps$\rightarrow 3\gamma$, and (d) the simulated background channels. After comparing the experimental data to simulations, the region from $\theta_1 + \theta_2 < 200°$ corresponds to the background as in (d) while the region $\theta_1 + \theta_2 > 200°$ maximizes the content of signal events as in (c). The maximum concentrated region in experimental data (a) at 180° is from 2γ annihilations from ^{22}Na source. Such a region is missing in total MC simulation (b) as the contribution from the source is not simulated in MC simulations for this study.

4.3 Background evaluation

In this experiment, several processes are present that can mimic the signal event of 3γ from the ortho-positronium annihilation. A detailed study is performed where different possible background events are defined and passed through the selection criteria of the identification of o-Ps events. These background events are majorly the secondary Compton scatterings of primary photons in the scintillators and within the annihilation chamber. The background events identified in this study are categorized as follows:

1. Contribution from direct or para-positronium annihilation: These include the events containing two primary photons of 511 keV energy each either from direct e^+ e^- annihilation or via the formation of para-positronium. The positrons from ^{22}Na source can directly annihilate to 2γ or interact with electrons in the porous material on the walls of the chamber where they form p-Ps which self annihilates to 2γ. This 2γ along with one de-excitation photon of 1.2 MeV energy resulting in a three-hit event is one of the major background components in this study. The pictorial representation of such kinds of events is shown in Fig. 4.5 (a) and (b).

2. Secondary Compton scatterings of annihilation photons in the detector: These include 3γ events where any one of the primary photons from o-Ps, p-Ps, or direct annihilation photon undergoes Compton scattering in the scintillators and is registered again as hit in the detector. This event consists of two primary annihilation hits while the third one corresponds to a secondary photon scattered from any of the primaries. The topology of this kind of event is shown in Fig. 4.5 (c) and (d).

3. The secondary Compton scatterings of primary photons inside the spherical annihilation chamber: These are similar kinds of events as mentioned above where the primary photon gets scattered on the walls of the spherical annihilation chamber, as shown in Fig. 4.5 (e).

4. Multiple Compton scattered events: The three gamma events where at least one of the primary photons gets scattered more than once in either the chamber material or in the scintillators. These include the scatterings of photons from direct, o-Ps, p-Ps annihilation, or the de-excitation photon shown in Fig. 4.5 (f).

5. Accidental coincidence events: Other cases like coincident events are also taken into account. These are the events where three recorded photons originate from more than one original event - they can just as well be coincidences of photons from e.g. two subsequent 2γ annihilations close in time.

These background events are classified and processed through the analysis scheme described in the event level selection criteria, described under Section 4.2 . This means that the energy deposition cut and scatter test was already performed before the background classification.

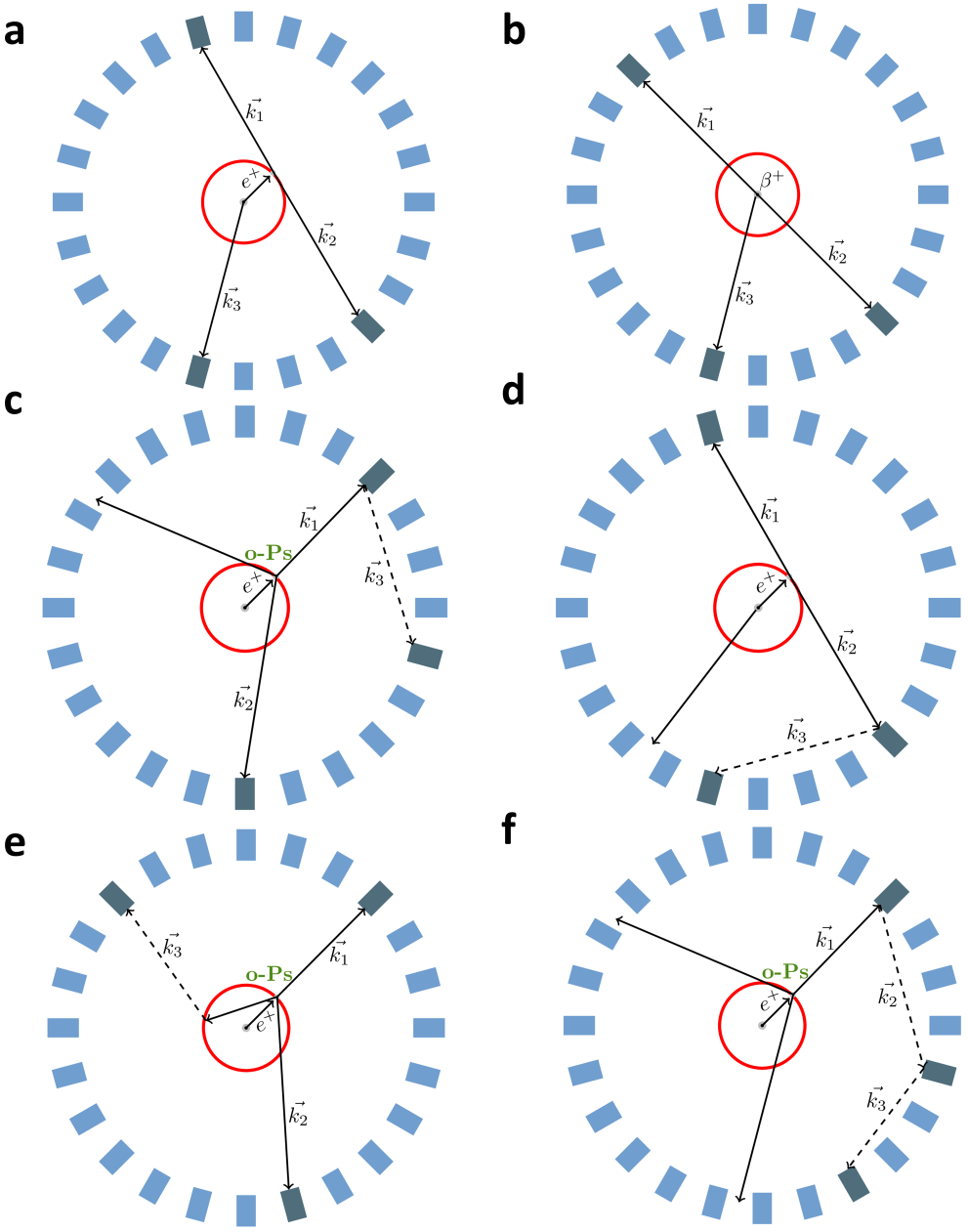

FIGURE 4.5: **Topological representation of 3γ background events.** Schematic representation of the different topologies of background events recorded in the J-PET detector where the red circle represents the cross-section of the spherical annihilation chamber at the center of the detector in the transverse plane. For clarity, only a reduced number of scintillation modules in one layer of J-PET are shown. The blue rectangles represent the scintillators while the ones in dark color correspond to those where photons get detected in the detector. Presented are events with 3γ interactions in the detector where (a) 2γ from para-positronium annihilation on the wall of spherical annihilation chamber along with the de-excitation photon, (b) 2γ from direct e^- and e^+ annihilation with the de-excitation photon (1.2 MeV), Secondary Compton scattering from (c) 3γ annihilation (o-Ps) where two of its primary photons recorded and the third photon is the secondary Compton scattering in the detector, (d) scattering events from 2γ annihilation, (e) Secondary Compton scattering in the annihilation chamber where two primary photons from o-Ps and third photon after scattered in the chamber get detected and (f) Multiple Compton scatterings in the detector.

The study is done to understand how these backgrounds behave differently from the signal events as shown in Fig. 4.6. This kind of distribution is already explained in the previous chapter in

Fig. 3.7. Here the background contribution from direct annihilation is not included, which mainly lies in the region of $\theta_1 + \theta_2 = 180°$ as the sum of two smallest angles between two back to back annihilation photons is 180°. At the last selection criteria, the events in the region $\theta_1 + \theta_2 > 204°$ and min $d_{LOR} > 11$ cm are taken for further studies.

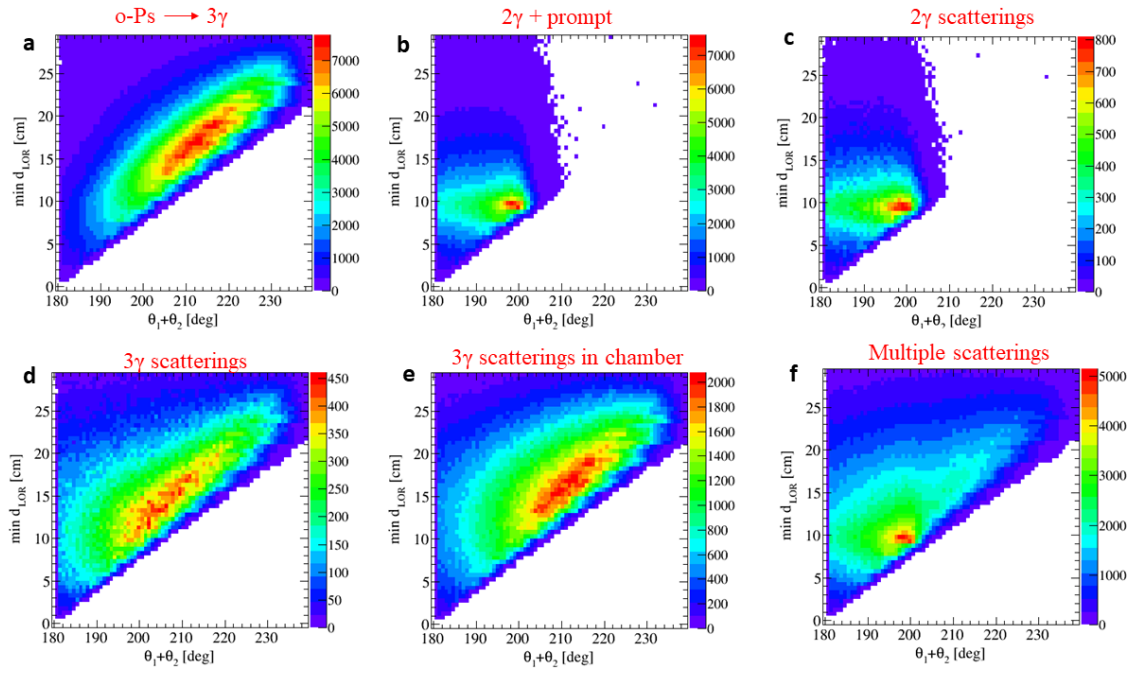

FIGURE 4.6: **Contribution of signal and background in MC simulations.** An exemplary distribution from MC simulations to visualize the properties of signal and background events. The x-axis represents the sum of the two smallest relative angles between the three recorded photons calculated from the center of the detector. The y-axis represents the shortest distance between the hypothetical 2γ annihilation point on the line of response (LOR) to the center of the detector. These are plotted after eliminating the 2γ background from direct annihilation which is $\theta_1 + \theta_2 = 180°$. The remaining 2γ events are the 511 keV photons from p-Ps annihilation and 3γ are from o-Ps annihilation. From (b) and (c) it is visible that the background from 2γ is concentrated mainly in the region of $181° < \theta_1 + \theta_2 < 200°$ and min $d_{LOR} < 10$ cm. The contribution of 3γ is in the region of $\theta_1 + \theta_2 > 200°$ and min $d_{LOR} > 10$ cm as visible from (a) and (e). Events with 3γ scatterings in the detector (d) and in the chamber (e) also follow a similar pattern to the signal events in (a) as these scattered events are from signal events.

Another distribution to differentiate the o-Ps signal events from the major background components in the study is presented in Fig. 4.7 [89]. The angles are calculated with respect to the center of J-PET detector. In the experimental data (Fig. 4.7 (a)), the region with highest concentration at $\theta_1 + \theta_2 = 180°$ is due to the direct annihilation of $e^+e^- \rightarrow 2\gamma$ events, as also visually represented in Figure 4.5 (b). The band around $154° < \theta_1 + \theta_2 < 208°$ in Fig. 4.7 (c) corresponds to the background events such as p-Ps$\rightarrow 2\gamma$ annihilation on chamber walls. These background events, involving two photons with opposite momenta, are expected to concentrate in a vertical band around 180° but as these annihilation occur on chamber wall, the range of their relative angles broadens to approximately $180° \pm 26°$ [90].

More discussion on the background overlapping with the signal events in the final studies is discussed in the next sections.

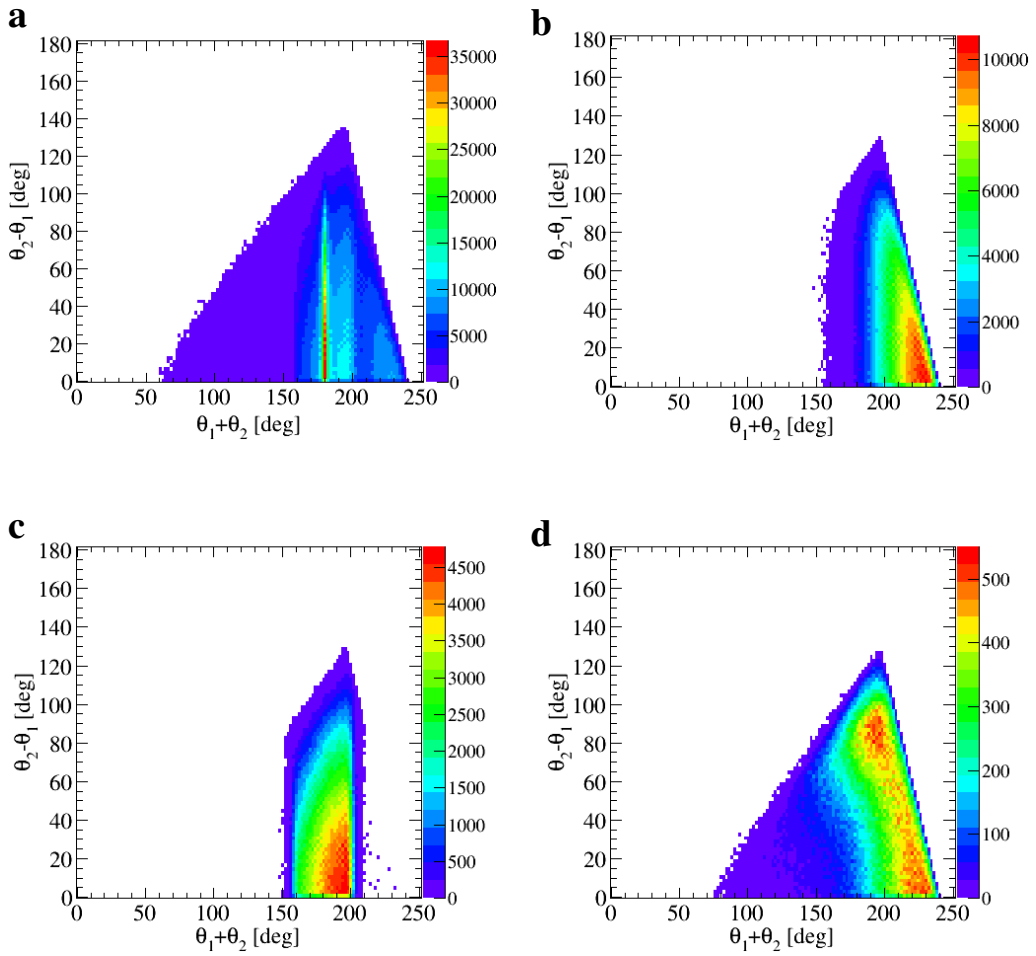

FIGURE 4.7: **Another exemplary distribution for comparison of experimental data to the signal and background events in MC simulations.** It is the relative distribution of the sum and difference of the two smallest angles between the 3γ recorded in the detector taken from the center of the detector frame. The relative distribution of angles for (a) experimental data compared with MC simulated events (b) o-Ps$\rightarrow 3\gamma$, (c) p-Ps$\rightarrow 2\gamma$ from the walls of the annihilation chamber, and (d) 3γ or 2γ annihilation with secondary Compton scattering. The rightmost region of $\theta_1 + \theta_2 > 200^\circ$ in experimental data is identified as o-Ps signal events.

4.4 Event selection efficiency

The effectiveness of the selection criteria applied to simulated signal and background events is evaluated by assessing the relative efficiency of the cuts for each event category. Relative efficiency is the proportion of events retained after applying a selection cut compared to the total number of events in that specific event category before that selection criteria. Table 4.1 showcases the relative efficiency achieved for both signal and various background events in analyzing the selection cuts. This table illustrates how the selection criteria influence specific event types. The high-efficiency value corresponds to the lower rejection rate and vice versa.

The amount of background events present in the study at the end of the whole selection criteria that mimic the signal events are given in Table 4.2. Out of all the major backgrounds left in the

TABLE 4.1: The relative event selection efficiency (%) of different background event types is compared with that of signal for the selection cuts based on energy deposition of photons, scatter test, and the sum of two smallest angles between photons. The total efficiency (%) is the product of three relative efficiencies at these selection cuts.

The event types are explained in the Section 4.3.

Event Type	Energy deposition Fig 4.2	Scatter test Fig 4.3	Angle sum (3D) Fig 4.4	Total Efficiency
3γ from o-Ps	62	79	64	31
3γ scattering	17	10	35	0.60
3γ scattering in chamber	53	69	47	17
2γ + prompt	64	15	0.2	0.02
2γ scatterings	14	5	0.3	0.002
2γ or prompt scatterings in chamber	56	26	14	2
Multiple scatterings in detector	19	11	26	1
Coincident events	34	18	26	2

study is the multiple scattering events, 2γ or 3γ scatterings in the chamber. The 55% of the total simulated events are from the signal events from o-Ps annihilation.

TABLE 4.2: The percentage of signal o-Ps $\rightarrow 3\gamma$ and specific background events evaluated in this study before and after applying the selection cuts.

Event Type	Before selection cuts (%)	After selection (%)
3γ from o-Ps annihilation (Signal)	0.7	55.3
3γ scattering	6	3.1
3γ scattering in chamber	0.5	17.1
2γ + prompt	2	0.2
2γ scatterings	13	0.2
2γ or prompt scatterings in chamber	10	4.5
Multiple scatterings in detector	50	17.3
Coincident events	0.2	2.1
Prompt γ and its scatterings	5	0.22

The cut-based selection method in the analysis is optimized by evaluating the signal-to-background ratio (S/B) and sample purity from the signal and background events at different selection cuts given in Table 4.3 and defined as:

$$\text{Purity} = \frac{\text{Signal}}{\text{Signal + Background}} \tag{4.1}$$

where Signal and Background correspond to the number of Signal and Background events.

TABLE 4.3: The selection cuts applied for the identification of o-Ps $\rightarrow 3\gamma$ (signal) events. The defined variables S/B, and purity depend on the amount of signal and total background present in the Monte Carlo simulations after each selection cut.

Selection Criteria	S/B	Sample Purity (%)
Energy deposition $<$ 340 keV	0.08	2.8
Trilateration condition	0.02	9
$\delta d_{ij} > 35$ cm	0.48	32
Angle sum (3D) $> 204°$	1.3	55

In this cut-based selection approach, the final MC simulated data sample has a signal-to-background ratio greater than one with a sample purity of 55%. The major background types that cannot be removed in this sample are the events with multiple scattering in the detector and scatterings in the chamber.

4.5 Background from Cosmic radiation

One of the background sources in the study comes from highly energetic cosmic radiation which includes the nuclei, electrons, positrons, etc. from outer space. These rays form secondary particles after interaction with an atmosphere (e.g. muons) which can be detected on the Earth's surface. The separate measurements were conducted with the J-PET detector without using any positron source and an annihilation chamber to study the effect of cosmic radiation interactions with the detector. The data is reconstructed similarly to identify the cosmic radiations that can pass the selection criteria for signal identification. These events deposit high energy in the plastic scintillators which can be realized from their Time over Threshold (TOT) distribution in Fig. 4.8. The cosmic events can mimic the annihilation and de-excitation photons as they span over the whole TOT range but with a maximum concentration above 120 ns. From the 60-day measurement with cosmic, in total 4123 cosmic events pass through the analysis criteria used for o-Ps signal identification for this study described in Section 3.2. After comparing the 356 days of measurement with the radioactive source for the CPT symmetry test, about 0.1% of the event sample is expected to come from cosmic radiation in accordance to equation 4.2.

$$N_{\text{Cosmic}} = \frac{\text{cosmic events}}{\text{Identified o-Ps events}} \times \frac{\text{Measurement time the } ^{22}\text{Na source}}{\text{Measurement time with cosmics}} \tag{4.2}$$

$$= \frac{4123}{47.8 * 10^6} \times \frac{356 \text{ days}}{60 \text{ days}} \sim 0.1\%$$

where N_{Cosmic} is the fraction of cosmic events in the final data sample.

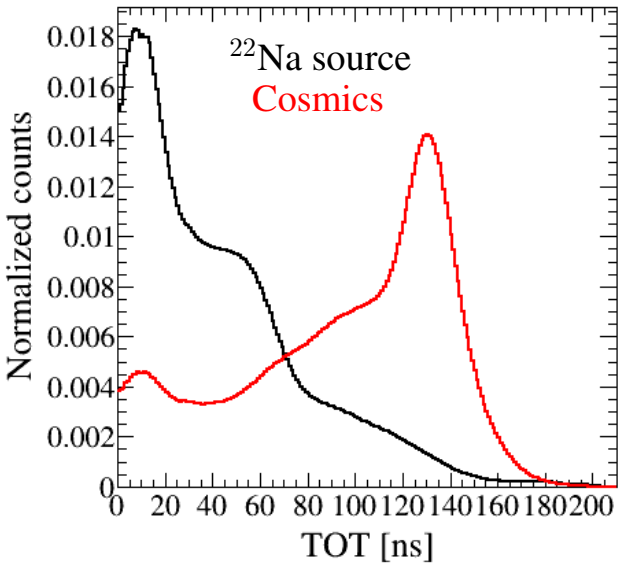

FIGURE 4.8: Time over Threshold (TOT) distribution for the experimental data from cosmic radiation interactions with the J-PET detector (red color). It is compared to the TOT from measurements with ^{22}Na source (black color, as given in Figure. 3.3).

4.6 CPT-odd angular correlation for the background

The operator of the CPT-odd correlation between the spin and normal to the decay plane of o-Ps is evaluated for the MC simulated events after the selection criteria described in Section 4.2.

The major 3γ background events considered are the multiple scatterings in the detector, scatterings in the annihilation chamber from o-Ps, and prompt gamma constituting 16%, 18% and 4% of the total data sample respectively, as given in Table 4.2. The angular correlation given by equation 3.3 is constructed for these background events and compared to the o-Ps signal events in MC simulation as shown in Fig. 4.9. The mean value of the operator distribution for each background channel is checked and they all are consistent with zero within the statistical uncertainty. Hence the backgrounds do not cause any asymmetry in the evaluation of the final CPT odd operator for this study at the level of achieved published uncertainty, more will be discussed in Chapter 5.

4.7 Optimizing smearing parameters in MC simulations

The simulated time and position of interaction are accounted for different detector resolutions of time (σ_t) and Z interaction of photons in the scintillator (σ_z). A dedicated study is performed to find the optimal resolutions of time and Z for the smearing of MC simulations where the reconstructed annihilation radius (Eq. 4.3) was a metric of consistency between experimental data and reconstructed MC-simulated events. The distance from the center of the detector of reconstructed

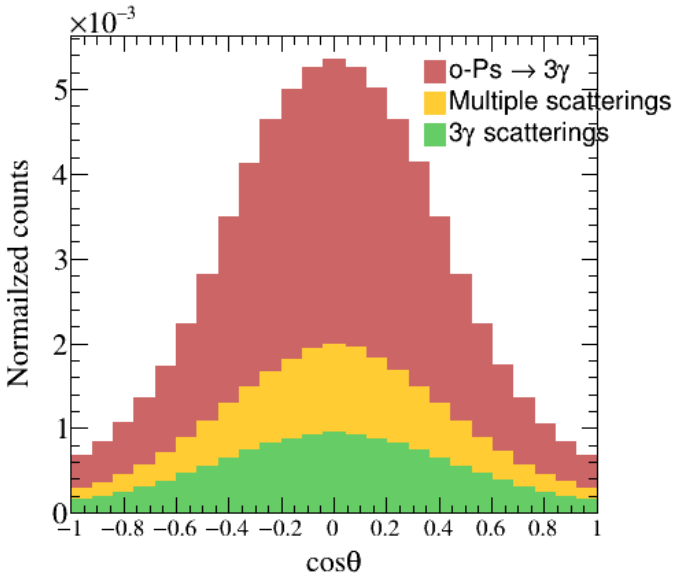

FIGURE 4.9: **CPT violation sensitive angular correlation.** Stack of the operator distribution for the o-Ps and the major background components in the study from MC simulations. The signal events constitute 55% of the total event sample with the remaining 45% constituted by the background from scatterings in the detector and annihilation chamber.

annihilation points of the identified o-Ps events, termed annihilation radius, is compared for data and MC simulations. The annihilation radius is given by

$$R = \sqrt{X^2 + Y^2 + Z^2} \tag{4.3}$$

X, Y, and Z are the three-dimensional coordinates of the reconstructed annihilation points of o-Ps events obtained from the trilateration reconstruction method (see Section 3.2.2 and Fig. 3.14).

The annihilation radius distribution for the identified o-Ps events in experimental data is compared to the MC simulations reconstructed for different values of σ_t = { 160, 190, 225, 250, 300 } ps. The comparison for different σ_t values is shown in Fig. 4.10. It is important to mention that the distributions are compared after the final analysis selection criteria on both data and simulations to know the best-optimized value of time resolution that can be used in MC simulations for this study.

The study is performed on the experimental data from a 78-day measurement with 1.1 MBq source activity and compared to its simulations. The statistics used in simulations are twice the statistics of data at the stage of the last selection criteria. The distributions for MC and data are normalized to their integrals while those of signal and background are normalized to the integral of total MC.

A shift of the distribution of the annihilation radius is observed for simulations at lower values of time resolution while comparing it to the distribution from data. The shift is decreasing with an increase in the time resolution. At a time resolution of 300 ps, the distribution is aligned for data and simulations and this value is chosen as the time resolution in MC simulations for this study.

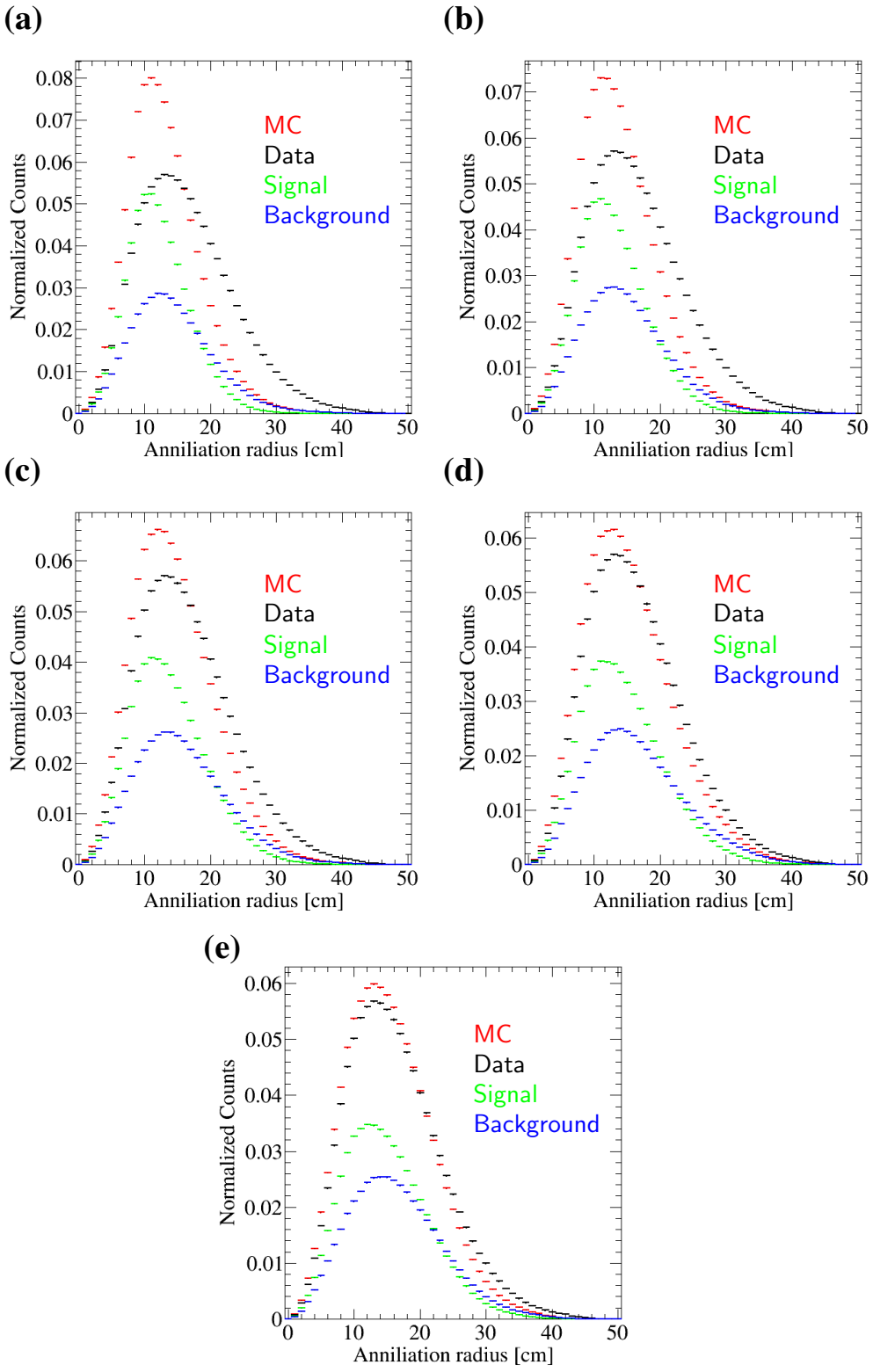

FIGURE 4.10: The annihilation radius distribution simulated for Time resolution (σ_t) values of (a) 160 ps, (b) 190 ps, (c) 225 ps, (d) 250 ps, and (e) 300 ps compared with the experimental data. The distributions from data and MC simulations are normalized to their integrals while signal and background are normalized to the integral of MC simulation. The shift in the data and MC simulation peaks is observed at lower values of time resolution. With higher values, the peaks start to align.

After fixing the time resolution to 300 ps, the Z resolution is varied to values σ_Z = { 1.5, 2, 2.5} cm. The comparison of simulations to data for the different values of z resolution is shown in Fig. 4.11. No significant shift in annihilation radius for simulations is observed at different z resolutions. The σ_Z = 2 cm and σ_t = 300 ps are chosen as resolution values in MC simulation for this study.

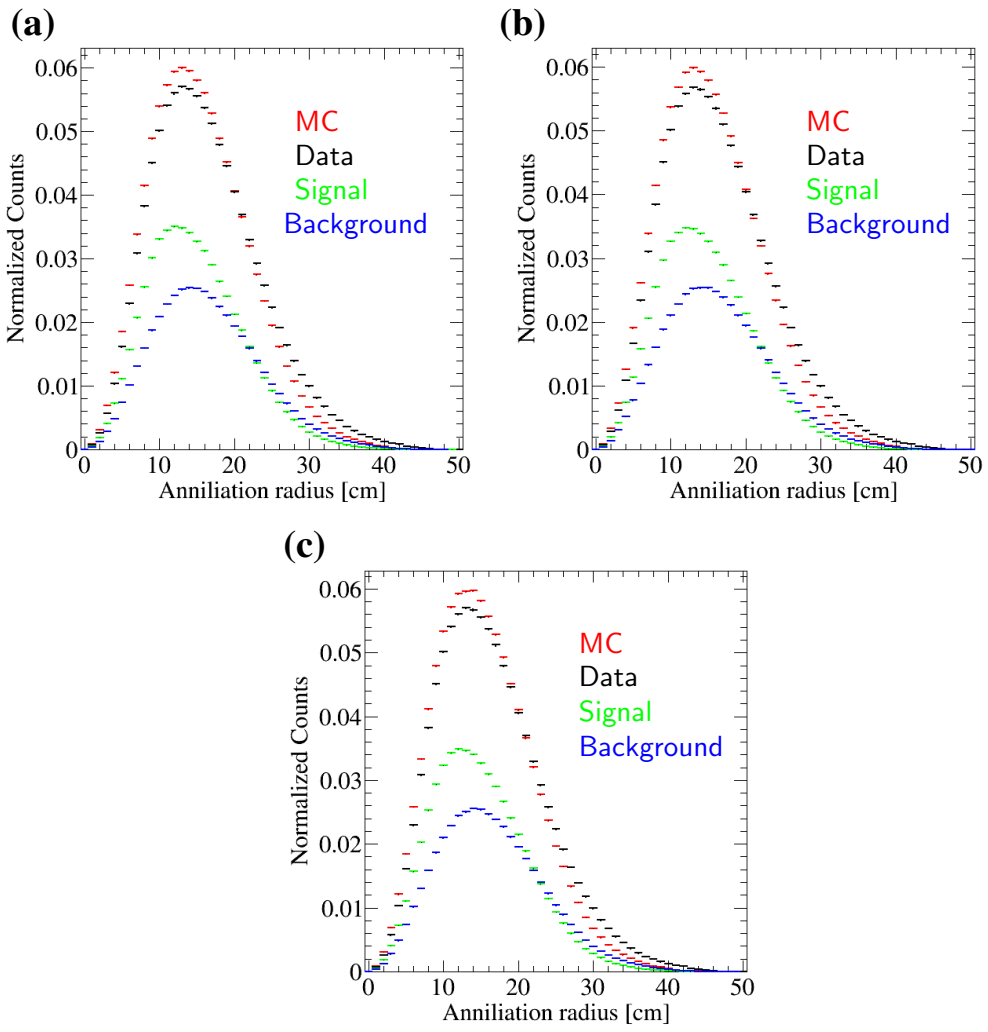

FIGURE 4.11: Comparison at different Z smearing of (a) 1.5 cm, (b) 2.0 cm and (c) 2.5 cm. The differences in the distributions at different z values are not significant.

4.7.1 Impact of the resolution parameters on the sensitivity of CPT odd operator

The time resolution impacts the distribution of the operator. Fig. 4.12 shows how the shape of the the CPT odd operator distribution in simulations varies at different values of time resolution. The value of $\sigma_t = 300$ ps is chosen in MC simulations for this study.

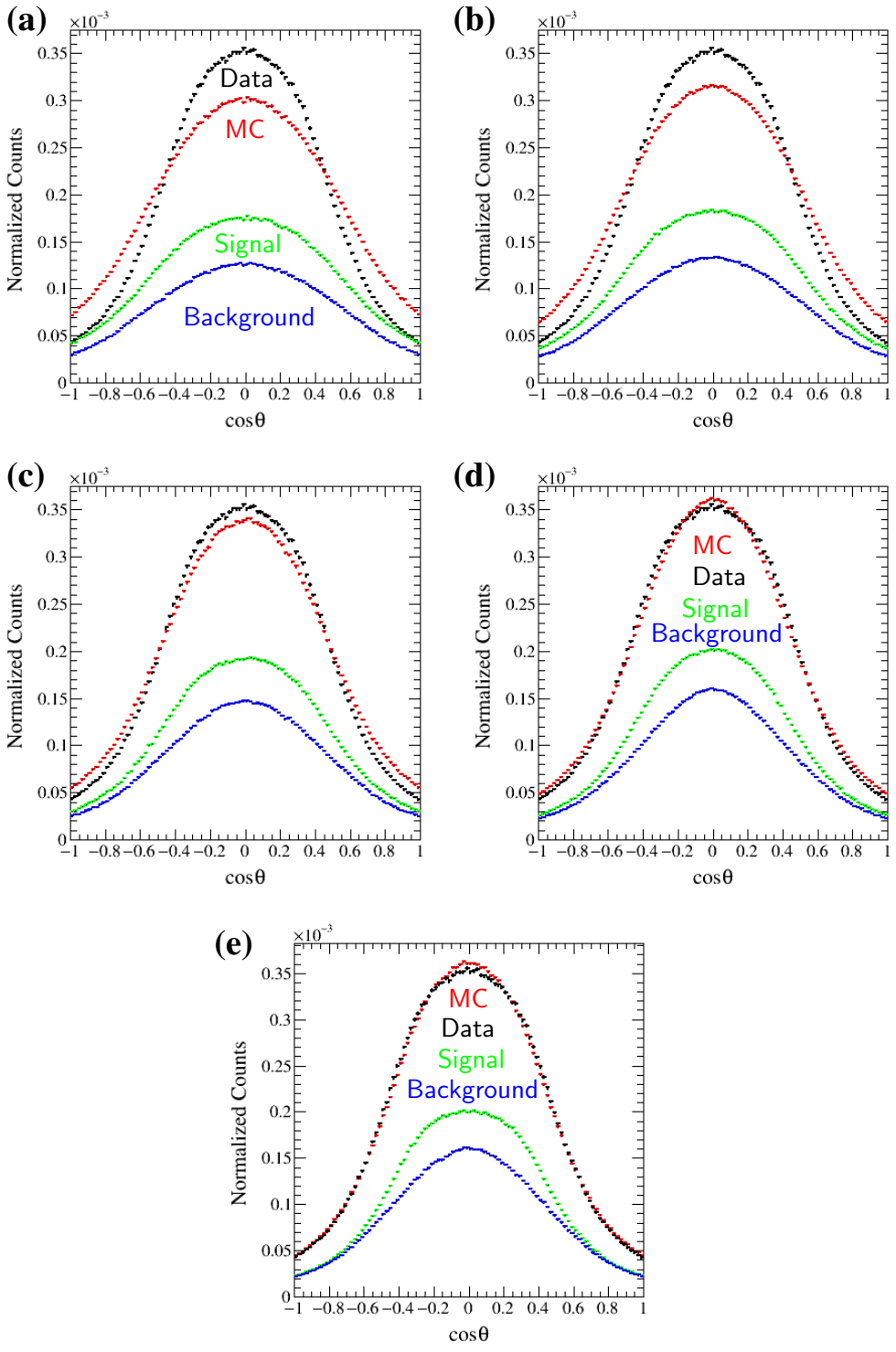

FIGURE 4.12: Comparison of the CPT odd operator distributions for Total Monte Carlo simulated events, experimental data, simulated signal, and background events. These are plotted at different Time resolution values of Time resolution (σ_t) (a) 160 ps, (b) 190 ps, (c) 225 ps, (d) 250 ps, and (e) 300 ps.

4.8 Optimizing selection criteria

The analysis scheme consists of three cut variables to identify the o-Ps events in experimental data and MC simulations, as given in Chapter 3 and 4. The TOT/Energy deposition (data/MC),

δd_{ij} in the scatter test, and a sum of the two smallest angles between photons (Angle sum) from the detector center are the three of the cut variables used in the analysis. The cut values for TOT or energy deposition are chosen based on the Compton edge for 511 keV annihilation photons as shown in Section 3.2 and 4.2. The main importance of this criterion is to reject the de-excitation photons.

To optimize the min δd_{ij} variable for the scatter test, a separate analysis was done for only three hit events in data and MC simulations. The cut value is chosen at the position of the valley-like region in the distribution of min δd_{ij} for three hit events, separately for data and MC as shown in Fig. 3.5 and 4.2. The chosen cut values are different for data and MC simulations.

As for the angle sum variable, the cut value is chosen to obtain the best consistency between data and MC which can be represented by a χ^2 consistency test by comparing the annihilation radius (Equation 4.3) for experimental data to the simulations at different cut values, given in Fig. 4.13 (a). The cut values are kept above 180° after eliminating the contribution from 2γ annihilations. The signal-to-background ratio (S/B) from MC simulations is also used as an optimization parameter for this cut variable as given in Fig. 4.13 (b). The χ^2/ndf distribution starts to flat after $\theta_1 + \theta_2 = 204°$ and the trend of S/B distribution changes at $\theta_1 + \theta_2 = 204°$ value that leads to choosing this value for the cut.

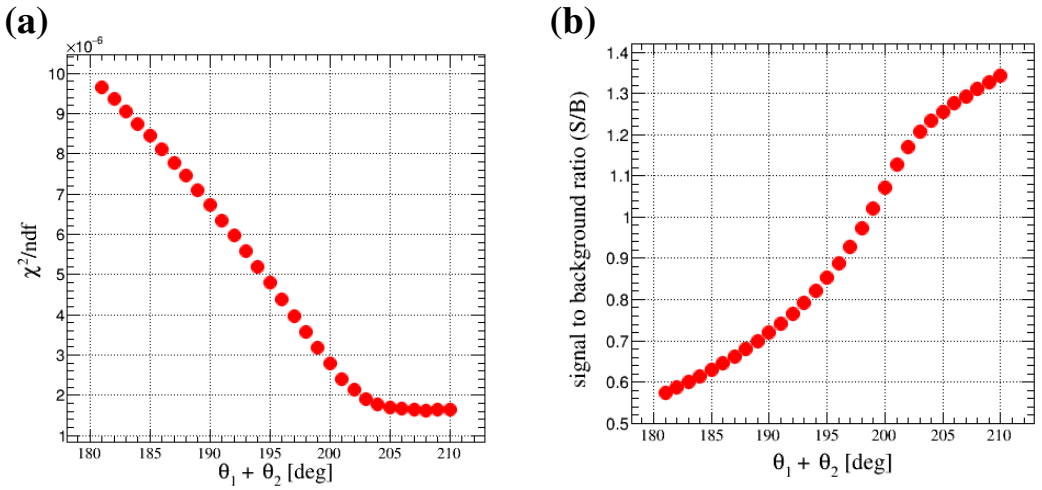

FIGURE 4.13: (a) The χ^2/ndf distribution and (b) signal to background (S/B) is used to optimize the analysis selection criteria of a sum of two smallest angles between annihilation photons.

Chapter 5

Study to evaluate the CPT odd observable

This chapter focuses on understanding the impact of different parameters used in the data analysis and evaluation of the CPT odd angular correlation operator on the experimental result. It includes the estimation of statistical uncertainty from two different measurements and detecting possible systematic effects in this study. The presented study leads to estimating the final expectation value of the CPT symmetry test in ortho-positronium decays with a J-PET detector.

5.1 Evaluation of statistical uncertainties on expectation value of CPT odd operator

The two potential forms of uncertainties affecting the final measurement are statistical and systematic uncertainties. Statistical uncertainties are the errors due to the statistical fluctuations in experimental data while systematic uncertainties are all other forms of error but not related to statistics of the data [91].

The measurement of asymmetry of the CPT odd operator $\vec{S} \cdot (\vec{k_1} \times \vec{k_2})$ is determined from the expectation value of the operator $<O_{CPT}>$ defined over the entire range of the $\cos\theta$ distribution, given in Section 3.3. The expectation value and its statistical error are estimated as

$$\begin{aligned} < O_{CPT} >= \frac{\sum_{i=1}^{nBins} x_i f(x_i)}{N_{Entries}} = \mu \,, \\ \sigma_{Statistical} = \frac{\sqrt{\sum_{i=1}^{nBins} f(x_i)(x_i - \mu)^2}}{N_{Entries}} \end{aligned} \tag{5.1}$$

where $f(x_i)$ is the number of events in a particular bin and x_i represents the value in the center of i_{th} bin in the $\cos\theta$ distribution. The larger $N_{Entries}$ is, the lesser the statistical error. The systematic effects of this study are discussed in Section 5.2.

The distribution of CPT-odd angular correlation for the identified o-Ps$\rightarrow 3\gamma$ decays in experimental data is given in Fig. 5.1 and 5.2. These figures compare the CPT odd operator from experimental data from two different measurements to its MC simulated total events, only signal and background events. The distributions are compared after optimizing the selection criteria for data as well as MC simulations (see Section 4.8) and optimized resolution parameters for MC simulations (see Section 4.7). The distribution for the data and MC simulations are normalized to their integrals while the signal and background are normalized to the integral of total MC.

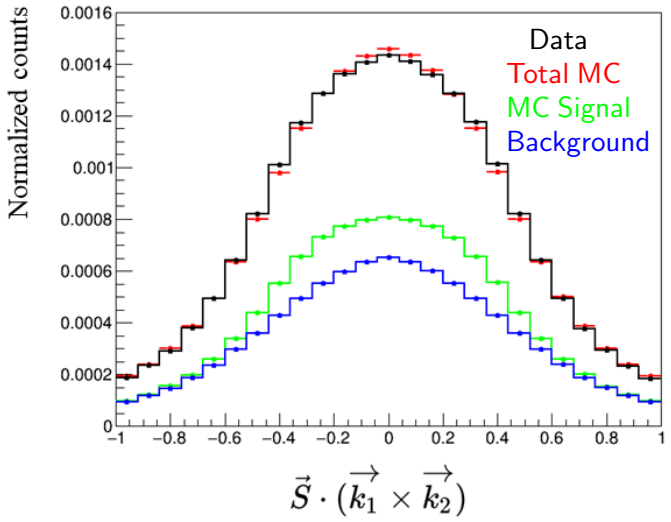

FIGURE 5.1: **CPT sensitive angular correlation.** The final distribution comparing data, total MC simulations, MC simulated signal events, and MC simulated background at 1.1 MBq source activity. The distribution is for 2.8 million o-Ps events from a 78-day measurement (termed as J-PET Run 12).

Fig. 5.1 presents the $\cos\theta$ distribution for 2.8 million o-Ps events from measurement at 1.1 MBq source activity. It is important to mention that for this measurement at 1.1 MBq source activity, the shown distribution in Fig. 5.1 has two times more MC events than data events at the stage of comparing operator distribution. A little discrepancy between data and MC is observed as the cosmic background is not simulated in the total MC.

A similar comparison of normalized distributions of the CPT sensitive angular correlation for data from the 278-day measurement at 4 MBq activity to its MC simulations is shown in Fig. 5.2. The presented data distribution is from 45 million o-Ps identified in experimental data. The total MC simulated events in this distribution constitute 19% of the data events compared at the last stage of selection criteria (described in Section 3.2). This means the statistics of MC are not equivalent to the data for this measurement. Due to the very high statistics of this experimental data, its equivalent MC simulations, using presently available programs and computing resources could take another 1 year of generation which is difficult in the scope of this thesis work. For that, some amount of simulations are generated to know the signal and background content in this data sample.

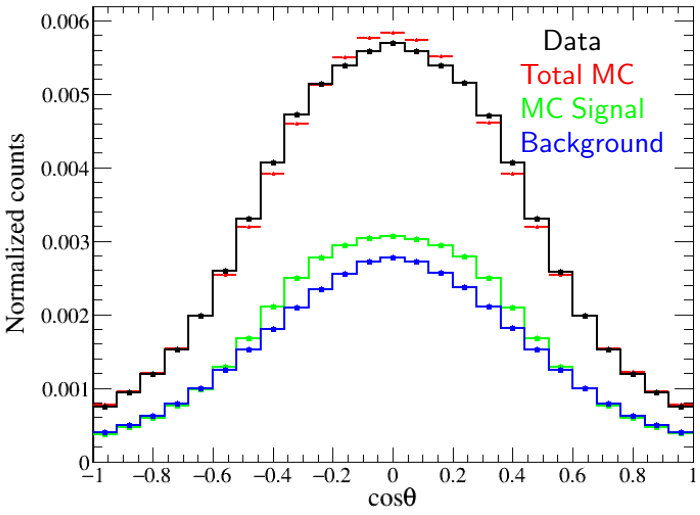

FIGURE 5.2: **CPT sensitive angular correlation from 278-day measurement.** The comparison of the distribution of CPT odd operator distribution for experimental data to its total MC simulated events, MC simulated signal events, and MC simulated background. It is plotted for the identified 45 million o-Ps events from a 278-day measurement at 4 MBq activity.

The mean and statistical error for the expectation value from $\cos\theta$ distribution is calculated using Equation 5.1 from the experimental data. The mean and its statistical uncertainty of $<O_{CPT}>$ for identified o-Ps events from two experimental data at different source activities are listed in Table 5.1.

TABLE 5.1: The identified o-Ps events and the statistical uncertainty on the expectation value of the CPT-odd operator $<O_{CPT}>$ for two measurements conducted with J-PET for the CPT symmetry test.

J-PET Run	Measurement duration	Identified o-Ps events	Expectation Value ($\mu \pm \sigma_{stat}$)
12 (1.1 MBq)	78 days	2.8×10^6	$-3.1 \pm 2.5 \times 10^{-4}$
13 (4 MBq)	278 days	45×10^6	$-0.98 \pm 0.62 \times 10^{-4}$

5.1.1 Signal and background estimation from MC simulations

The signal and the background content in the final data sample of the CPT symmetry test with J-PET are listed in Table 5.2. The numbers are estimated from the MC simulations of the setup at different source activities and the optimized threshold values used in this study. The estimated background in the measurement with 4 MBq activity is comparatively larger due to random coincidence events, which is also visible from the normalized background distribution in Fig. 5.2 on comparing it with the same distribution in Fig. 5.1.

The expectation value of the CPT odd operator for MC simulated events is given in Table 5.3. These values correspond to simulations using a 1.1 MBq source activity as the set of simulations

TABLE 5.2: Properties of signal and background obtained from MC simulations for two sets of measurements at different source activity.

Activity	S/B	Sample Purity (%)
1.1 MBq	1.3	55
4 MBq	1.1	53

from this measurement has equivalent statistics to the experimental data. The mean value of the operator for the MC-simulated background is consistent with zero, indicating its symmetric nature.

TABLE 5.3: The expectation value of the CPT-odd operator $<O_{CPT}>$ for signal and background from MC simulations. The listed values are obtained from the MC simulations of J-PET Run 12 at 1.1 MBq source activity, distributions are given in Fig. 5.1.

Type of events	Expectation Value ($\mu \pm \sigma_{stat}$)
Total MC simulated events	$2.9 \pm 1.7 \times 10^{-4}$
MC Signal	$2.3 \pm 2.2 \times 10^{-4}$
MC Background	$3.5 \pm 2.6 \times 10^{-4}$

5.1.2 Error estimation for removing background contribution in data

The simulation study shows that the selected events in the experimental data from each measurement have some fraction of background along with the signal events (see Table 5.2). To account for the background, the statistical error of each measurement is scaled down based on the estimation given as:

$$\sigma^2_{signal} = \sigma^2_{experiment} \cdot \frac{N_{experiment}}{N_{experiment} - N_{Background}}, \qquad N_{Background} = f \cdot N_{experiment}\,. \tag{5.2}$$

where f is the fraction of background present in each measurement. The background content is 0.45 and 0.47 in Run 12 and 13 as given in Table 5.2.

TABLE 5.4: Statistical error of two measurements after scaling down the background content.

Measurement with source activity	1.1 MBq	4 MBq
Statistical error	3.4×10^{-4}	0.85×10^{-4}

The mean and its statistical uncertainty for the final expectation value of the CPT-odd angular correlation operator are evaluated in the next section.

5.2 Studies of systematic effects

The different forms of systematic variations that can be considered in this analysis of two different measurements are discussed in the following sections.

5.2.1 Data consistency check

A crosscheck on the consistency of the data collected for the CPT symmetry test is done by splitting it into four independent sub-samples. The one year of data is divided into four subsets each consisting of three months of data. These sub-samples are analyzed separately to estimate the expectation value of the CPT odd angular correlation operator. The mean and error of $<O_{CPT}>$ for these subsets are compared with the mean of the final result obtained, given in Fig. 5.3.

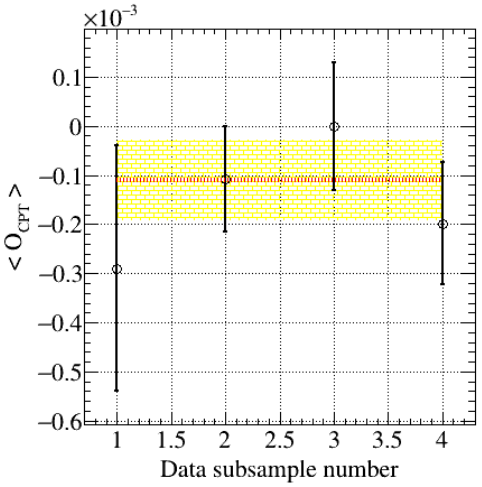

FIGURE 5.3: Dividing data into subsets: The total 365 days of data used in this work is divided into four subsets of three months each. The single data point represents the mean with its statistical error for the CPT odd operator obtained from different data-taking periods. The red and yellow lines represent the final mean and its error of $<O_{CPT}>$ for the whole data sample.

The first data sub-sample point is from the data set with a lower activity of 1.1 MBq while other points are at 4 MBq source activity but all correspond to the same duration of the measurement. These are the independent sample points obtained at different experimental conditions on source activity. The red horizontal line is the final mean of the $<O_{CPT}>$ for the whole data sample and the yellow region is the final error of its mean (-0.00011 $\pm$ 0.00008). There is no significant deviation of each sample point from the mean of the whole data observed as these points lie within the 1σ of the final results.

5.2.2 Cut Variations

The impact of the event selection cut variables on the expectation value of the CPT odd angular correlation is studied for the experimental data. At first, the TOT upper cut values are varied keeping the rest of the cuts the same as in the event selection criteria for the final result (see Fig. 3.3). The upper cut on TOT are changed to values TOT_{Upper} = {40, 55, 60, 67} ns. The expectation value at each of the cut values is given in Fig. 5.4. After this, the lower TOT values are varied to a range of values TOT_{lower} = {0, 3, 5, 7, 10} ns. Fig. 5.4 represents the expectation value at TOT lower and upper cut values with the mean value and its error as the error bar. The red line

and yellow band represent the mean and its error bar of the operator at the TOT upper cut value of 67 ns with no cut on its lower bound as used in the final selection criteria given in Section 3.2. The one cut variable is varied at one time and the others are the same as used in the data selection criteria.

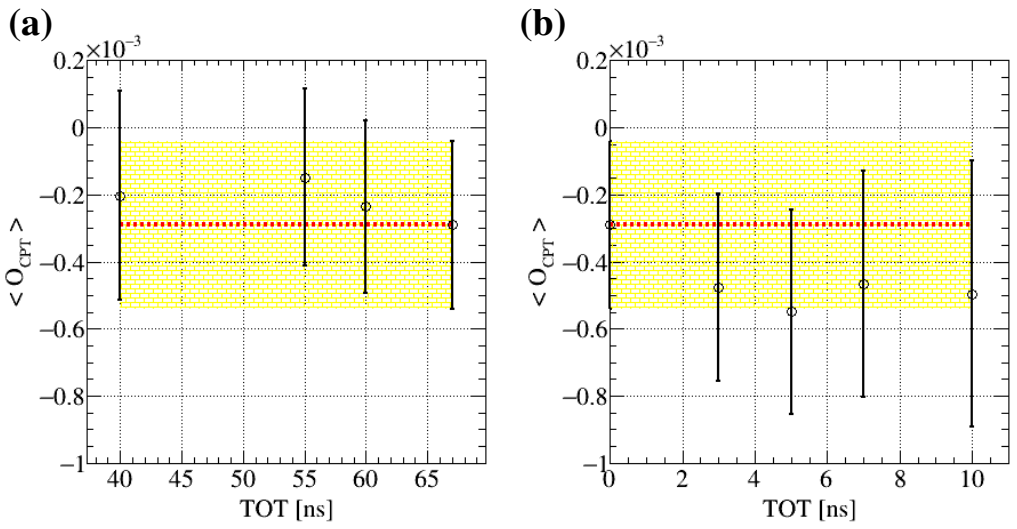

FIGURE 5.4: Comparison of the mean and its error at different values of TOT **(a)** upper and **(b)** lower bounds to the expectation value at TOT selection cut in the final data selection. The red dotted line and yellow band represent the mean value and the statistical error for the CPT odd operator obtained at 67 ns as the TOT upper cut value. This value is the one chosen for the final selection criteria for the CPT symmetry studies.

The impact of δd_{ij} for the scatter test is checked for the values of {15, 16, 17, 18, 20, 21, 22, 24, 26, 27, 28, 31} cm and compared with the final selected value at 23 cm. Fig. 5.5 gives the $<O_{CPT}>$ at different cut values. The mean values at different cut values on δd_{ij} lie within the statistical limit of the chosen cut at 23 cm.

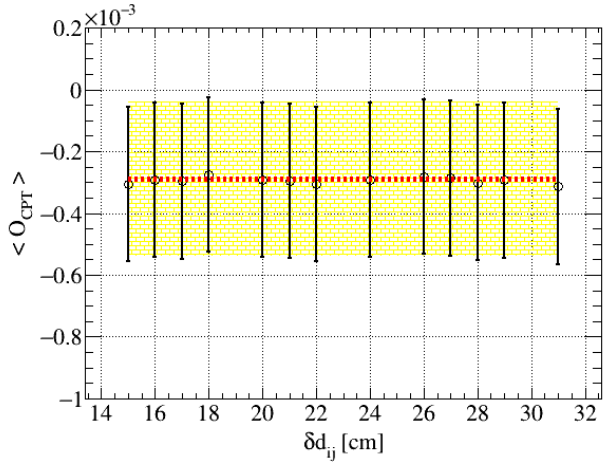

FIGURE 5.5: Mean and the error of the $<O_{CPT}>$ at different cut values of δd_{ij}. The red line is the mean value of the final result at 23 cm cut value and the yellow region represents the error of its mean. There is no significant change in the expectation value at different cut values for the scatter test.

Similarly, the Angle sum cut is varied in the range of $\{198 - 210\}^{\circ}$ to know its impact on the final operator distribution, given in Fig. 5.6.

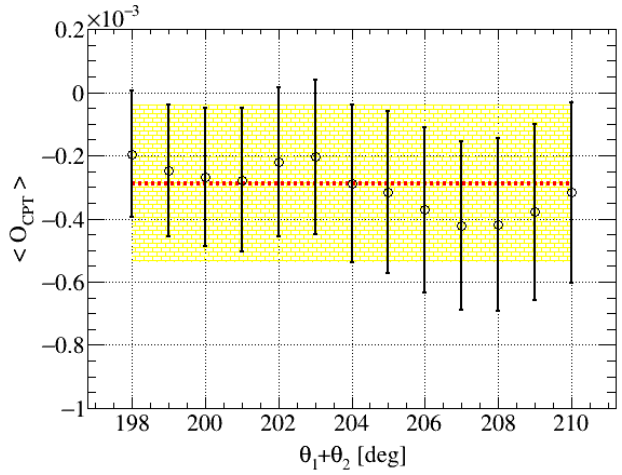

FIGURE 5.6: Comparison of $<O_{CPT}>$ at the final angle sum (3D) selection criteria. The red line and the yellow band are the mean value and its error of the final CPT odd operator at 204° cut value.

It is to be mentioned that the above checks are done for the J-PET Run 12 data sample at 1.1 MBq source activity. The studies indicate that the TOT cut might impact the final result (however within 1σ value) while the other two remaining cuts don't significantly affect the $<O_{CPT}>$.

At each stage of the selection criteria, the contribution of the event selection cut variables used in the analysis to the systematic uncertainty of the final result is investigated. The cut variable is shifted to $\pm$ the amount of its experimental resolution (σ). The nominal value represents the actual $<O_{CPT}>$ obtained for the final results. The shifted expectation value is obtained by changing the cut variable to $\pm\ 2\sigma$. The systematic contribution for each data selection criteria is estimated to be $\sigma_{sytematic}$ as given in the below equations. This method is adapted from Barlow's method of estimating the systematic [92, 93] consistently with the approach used in previous studies [94, 95]. For a given parameter, its contribution to systematic uncertainty is considered statistically significant when the significance would be greater than one.

$$\begin{aligned}
\text{Nominal Value} &= \mu_1 \pm \sigma_1\,, \\
\text{Shifted Value} &= \mu_2 \pm \sigma_2\,, \\
\Delta < O_{CPT} > &= \mu_1 - \mu_2\,, \\
\sigma_{Systematic} &= \sqrt{\sigma_2^2 - \sigma_1^2}\,, \\
\text{Significance} &= \frac{\Delta < O_{CPT} >}{\sigma_{systematic}}
\end{aligned} \tag{5.3}$$

The variation of selection cuts is performed separately for the 78-day and 278-day measurements with 1.1 and 4 MBq source activity. These are varied to $\pm 2\sigma$ of their corresponding experimental resolutions as given in Table 5.5 and 5.6. There is no statistically significant impact on the

measured value of $<O_{CPT}>$ observed from varying the event selection criteria as the significance obtained for each is less than one.

TABLE 5.5: Contribution to systematic uncertainty by varying event selection criteria for 78-day measurement with 1.1 MBq source activity (referred to as J-PET Run 12).

ToT (σ = 1 ns); μ_1 = -3.1 $\pm$ 2.5 $\times$ 10^{-4}

Variation	Mean Value (μ_2)	Error (σ_2)	$\triangle < O_{CPT} >$	$\sigma_\triangle$	$\triangle/\sigma_\triangle$
+2σ	-3.0 $\times$ 10^{-4}	2.5 $\times$ 10^{-4}	0.93 $\times$ 10^{-5}	2.8 $\times$ 10^{-5}	0.3
-2σ	-2.8 $\times$ 10^{-4}	2.5 $\times$ 10^{-4}	2.5 $\times$ 10^{-5}	3.0 $\times$ 10^{-5}	0.8
δd_{ij} (σ = 1 cm)					
+2σ	-3.0 $\times$ 10^{-4}	2.5 $\times$ 10^{-4}	0.13 $\times$ 10^{-5}	1.2 $\times$ 10^{-5}	0.1
-2σ	-3.1 $\times$ 10^{-4}	2.5 $\times$ 10^{-4}	0.63 $\times$ 10^{-5}	0.75 $\times$ 10^{-5}	0.8
Angle sum (3D) (σ = 1.2°)					
+2σ	-3.7 $\times$ 10^{-4}	2.6 $\times$ 10^{-4}	6.5 $\times$ 10^{-5}	8.4 $\times$ 10^{-5}	0.8
-2σ	-2.8 $\times$ 10^{-4}	2.3 $\times$ 10^{-4}	2.1 $\times$ 10^{-5}	9.2 $\times$ 10^{-5}	0.2

The expectation value obtained from Run 12 data is $<O_{CPT}>$ is -3.1 $\pm$ 2.5 $\times$ 10^{-4}. Table 5.5 shows no significant deviation of the mean at different shifted cut variables from the final expectation value obtained from Run 12.

TABLE 5.6: Checks on the possible contribution to systematic uncertainty from event selection criteria for 356-day measurement with 4 MBq source activity (referred to as J-PET Run 13).

ToT (σ = 1 ns); μ_1 = -0.98 $\pm$ 0.62 $\times$ 10^{-4}

Variation	Mean Value (μ_2)	Error (σ_2)	$\triangle < O_{CPT} >$	$\sigma_\triangle$	$\triangle/\sigma_\triangle$
+2σ	-0.99 $\times$ 10^{-4}	0.62 $\times$ 10^{-4}	0.060 $\times$ 10^{-5}	0.68 $\times$ 10^{-5}	0.1
-2σ	-0.99 $\times$ 10^{-4}	0.62 $\times$ 10^{-4}	0.038 $\times$ 10^{-5}	0.76 $\times$ 10^{-5}	0.04
δd_{ij} (σ = 1 cm)					
+2σ	-1.0 $\times$ 10^{-4}	0.62 $\times$ 10^{-4}	0.22 $\times$ 10^{-5}	0.54 $\times$ 10^{-5}	0.4
-2σ	-0.97 $\times$ 10^{-4}	0.62 $\times$ 10^{-4}	0.18 $\times$ 10^{-5}	0.23 $\times$ 10^{-5}	0.8
Angle sum (3D) (σ = 1.2°)					
+2σ	-0.89 $\times$ 10^{-4}	0.66 $\times$ 10^{-4}	0.87 $\times$ 10^{-5}	2.2 $\times$ 10^{-5}	0.4
-2σ	-1.3 $\times$ 10^{-4}	0.57 $\times$ 10^{-4}	3.4 $\times$ 10^{-5}	2.3 $\times$ 10^{-5}	1.5

5.2.3 Background effects

One of the backgrounds in the study is cosmic radiation as explained in Section 4.5. Its contribution to the systematic uncertainty is estimated by analyzing the 60-day data from cosmic measurements. It is estimated that less than 0.1% of background contribution is from cosmic radiations in the final data sample from 365-day measurement with the radioactive source, given in Section 4.5. The expectation value of 4123 cosmic events from cosmic measurements is $<O_{CPT}>$ = (0.21 $\pm$ 0.62) $\times$ 10^{-2}. Therefore the maximal systematic shift of the final result due to the presence of 0.1% cosmic events in the final event sample would be at the level of 10^{-5}.

5.2.4 Binning effects

The CPT odd operator distribution consisted of 25 bins in the range from -1 to 1. A systematic check is done by varying the number of bins and presented in Table 5.7 separately for two measurements used in this study.

TABLE 5.7: Checks on systematic effect at different bin sizes of the $\cos\theta$ distribution for CPT odd operator. The checks are done separately for two sets of measurements at 1.1 and 4 MBq source activity.

1.1 MBq (J-PET Run 12); μ_1 = -3.1 $\pm$ 2.5 $\times$ 10^{-4} at 25 bins

Bins	Mean Value (μ_2)	Error (σ_2)	$\triangle < O_{CPT} >$	$\sigma_\triangle$	$\triangle/\sigma_\triangle$
50	-2.9 $\times$ 10^{-4}	2.5 $\times$ 10^{-4}	1.2 $\times$ 10^{-5}	0.93 $\times$ 10^{-5}	1.2
12	-2.9 $\times$ 10^{-4}	2.5 $\times$ 10^{-4}	1.2 $\times$ 10^{-5}	1.9 $\times$ 10^{-5}	0.6

4 MBq (J-PET Run 13); μ_1 = -0.98 $\pm$ 0.62 $\times$ 10^{-4} at 25 bins					
50	-0.95 $\times$ 10^{-4}	0.62 $\times$ 10^{-4}	0.33 $\times$ 10^{-5}	0.22 $\times$ 10^{-5}	1.4
12	-0.96 $\times$ 10^{-4}	0.62 $\times$ 10^{-4}	0.23 $\times$ 10^{-5}	0.48 $\times$ 10^{-5}	0.5

5.2.5 Missing scintillators in the detector system

Looking for asymmetries such as in the experiment is particularly vulnerable to any flaws in the symmetry of the detection system. To check any asymmetry from the detector setup, a test is done where one of the scintillators is excluded from the 192-strip J-PET detector. The hits registered in the other 191 scintillators of the J-PET detector are considered for the event selection analysis. The three-gamma events from o-Ps are identified (using the same selection criteria given in Section 3.2) and the distribution of $\cos\theta$ for CPT odd angular correlation is studied, given in Fig. 5.7. It is a data-based study done separately for measurements with source activity of 1.1 and 4 MBq.

The expectation value of the CPT odd operator with one excluded scintillator in the detector comes out to be $<O_{CPT}>$ = (-0.31 $\pm$ 0.25) $\times$ 10^{-3} for 78-day measurement with 1.1 MBq source activity. The expectation value for 278-days measurement with 4 MBq source activity comes to be

(-0.11 $\pm$ 0.07) $\times$ 10^{-3}. There is no observed asymmetry on the final distribution if any scintillator in the J-PET detector is missing or stops working. It would impact the statistics of identified ortho-positronium events marking it a statistical effect.

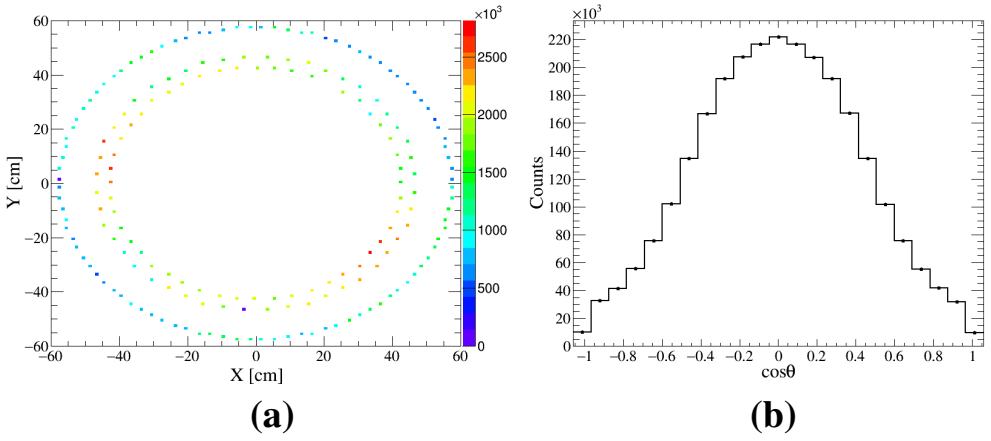

FIGURE 5.7: **One scintillator missing in 192-strip J-PET detector.**(a) The interaction position of the photons in the 191 scintillators of the detector in the XY transverse plane. There is an empty spot at X = 20 cm and Y = 35 cm due to the absence of one scintillator strip in the detector. (b) The $\cos\theta$ distribution for the identified o-Ps events. It shows the symmetric nature of angular correlation distribution with an expectation value of $<O_{CPT}>$ = -0.31 $\pm$ 0.25 $\times$ 10^{-3}.

5.2.6 Laboratory conditions

Laboratory conditions such as temperature and pressure used to create a vacuum inside the annihilation chamber were considered as another factor with a possible impact on the experiment result. Experimental data collected at different pressure conditions is mentioned in Table 3.1. The given data is analyzed and the expectation value of the final operator is compared, as given in Table 5.8. The data is processed through the same analysis criteria as described in Section 3.2. The number of events that survived all the selection criteria are the identified o-Ps events.

TABLE 5.8: The duration of measurements with 3-layer J-PET and spherical annihilation chamber at different pressures inside the annihilation chamber. The 1.1 MBq activity of ^{22}Na source was used during these measurements.

Pressure	Measurement duration	$<O_{CPT}>$	Identified o-Ps events
1 – 5 Pa	24 days	(-5.5 $\pm$ 3.8) $\times$ 10^{-4}	1.3 $\times$ 10^{6}
101 kPa (Atmospheric pressure)	35 days	(-2.1 $\pm$ 1.4) $\times$ 10^{-3}	84293
less than 1 Pa	78 days	(-3.1 $\pm$ 2.5) $\times$ 10^{-4}	2.8 $\times$ 10^{6}

There is no such statistically significant impact on the expectation value of the CPT odd operator observed from the collected data.

5.2.7 Impact of source position

The impact of the positioning of ^{22}Na source used in measurements on the experimental result is also evaluated. The source was positioned at the center of the detector system during the experimental measurements, as given in Fig. 3.1. There was no separate measurement conducted for this test. To study this effect, the coordinate system of reconstructed hits from the already existing data (with the source positioned at the center of the detector) is shifted from the center to a few other positions (with in 1σ from the center). The shifted positions considered are X, Y, Z = { (0.1, 0, 0); (0, 0.1, 0); (0.1, 0.1, 0) } cm. The effects are checked for two sets of measurements at 1.1 and 4 MBq source activity. The expectation value of the CPT-odd operator at the specified shifted positions is compared with the one where the source was at the center, as given in Table 5.9.

TABLE 5.9: The mean and its error for the expectation value at the shifted center coordinates of source position for 1.1 MBq activity measurement. The $<O_{CPT}>$ = (-3.051 $\pm$ 2.504) $\times$ 10^{-4} for these measurement where source is at the center of the detector system i.e. at (0,0,0) position.

Position [cm]	Mean Value (μ_2)	Error (σ_2)	$\triangle < O_{CPT} >$	$\sigma_{\triangle}$
(0.1, 0, 0) [1σ shift in x-axis]	-2.748 $\times$ 10^{-4}	2.503 $\times$ 10^{-4}	3.036 $\times$ 10^{-5}	0.3494 $\times$ 10^{-5}
(0, 0.1, 0) [1σ shift in Y axis]	-2.501 $\times$ 10^{-4}	2.504 $\times$ 10^{-4}	5.504 $\times$ 10^{-5}	0.3772 $\times$ 10^{-5}
(0.1, 0.1, 0) [1σ shift in XY axis]	-2.242 $\times$ 10^{-4}	2.504 $\times$ 10^{-4}	8.092 $\times$ 10^{-5}	0.2532 $\times$ 10^{-5}

5.2.8 Summary on systematic tests

The above-presented factors are studied as tests of the systematic uncertainties for the CPT symmetry test with J-PET and spherical annihilation chamber. The Barlow's approach is used to estimate the significance of possible systematic effect [92]. The precision level of systematic comes out to be insignificant with respect to the statistical error.

5.3 Determining the extent of CPT symmetry violation with J-PET

The determination of the level of potential CPT violation from the angular correlation operator $\vec{S} \cdot (\vec{k_1} \times \vec{k_2})$ requires the estimation of its expectation value. The mean and the statistical error of the expectation value are calculated in Section 5.1. For each of the measurements from Table 5.4, the statistical uncertainty is scaled down to account for the amount of background expected to be present in the final data sample on the basis of MC simulations. The final expectation value of the CPT odd operator is calculated by taking the weighted average of two different measurements, as presented in the following section.

5.3.1 Weighted average

The weighted average of the expectation values from two measurements is evaluated using the inverse variance weight method, as given below.

$$\begin{aligned} \mu_{wtd} &= \frac{\sum_{i=1}^{2} w_i \mu_i}{\sum_{i=1}^{2} w_i}, \\ \sigma_{wtd} &= \sqrt{\frac{1}{\sum_{i=1}^{2} w_i}} \\ w_i &= 1/\sigma_i^2 \end{aligned} \tag{5.4}$$

The w_i are the weights for two measurements which are inverse of the variance of the CPT odd operator, μ_i is the mean of the operator for each measurement, and μ_{wtd} and σ_{wtd} are the weighted mean and its error. The weighted expectation value from the two measurements is listed in Table 5.10.

TABLE 5.10: The summary of the expectation value of the CPT odd operator from two measurements after eliminating background content from each measurement and the weighted average of the respective measurements.

J-PET Run	12 (1.1 MBq)	13 (4 MBq)	Weighted Average
Expectation Value	-3.1 $\pm$ 3.4 $\times$ 10^{-4}	-0.98 $\pm$ 0.85 $\times$ 10^{-4}	-1.1 $\pm$ 0.82 $\times$ 10^{-4}

5.3.2 Evaluation of CPT odd asymmetry amplitude C_{CPT}

The amplitude of CPT violation is defined as the ratio of the expectation value of the operator to the degree of polarization associated with the uncertainty in estimating the spin axis of ortho-positronium events, as given below.

$$C_{CPT} = \frac{< O_{CPT} >}{P} \tag{5.5}$$

As already discussed, the positrons from ^{22}Na decay are linearly spin-polarized along the direction of their flight (i.e. along its momentum) due to parity violation. The dominant contribution to the effective ortho-positronium polarization arises from incorporating the evaluation of the spin axis orientation for each annihilation event along the direction of flight of the positron. This effective polarization (P) is determined by a convolution of several factors like the longitudinal polarization of positrons emitted from ^{22}Na decay where <P> = <v>/c = 67% [9]. The positrons are partially depolarized after undergoing multiple scatterings in aerogel. It results in an 8% polarization loss of positrons from thermalization [9]. The statistically transferred polarization fraction to the formed o-Ps due to spin statistics is $\frac{2}{3}$ [4]. The uncertainty in estimating the direction of positron emission depends on the reconstruction of the annihilation point on the walls of the spherical chamber. The polarization loss due to geometrical uncertainty amounts to 9% [83]. The effective polarization (P)

after incorporating all these factors amounts to 37.4%. This number is adapted from the previous work on testing the CPT-odd operator with J-PET as given in Ref. [8].

Chapter 6

Results and Discussion

The expectation value obtained from the angular distribution of the CPT odd operator $\vec{S} \cdot (\vec{k_1} \times \vec{k_2})$ after correction for the background contribution amounts to:

$$< O_{CPT} >= -1.1 \pm 0.82 \times 10^{-4} \tag{6.1}$$

The amount of background in the study is estimated from Monte Carlo Simulations and the background error is included in the final results, given in Chapter 5. After correcting the expectation value with the analyzing power of the setup P = 37.4%, the CPT asymmetry amplitude comes out to be

$$C_{CPT} =< O_{CPT} > /P = -0.00029 \pm 0.00022 \tag{6.2}$$

The obtained results are consistent with the CPT invariance showing no asymmetry at the achieved level.

An improved and advanced precise test of CPT symmetry in ortho-positronium decays with the J-PET detector has been reported in this thesis. The test is done by measuring the correlation between the momentum of annihilation photons and the spin orientation of decaying positronium without using any external magnetic field. The test is conducted with a 3-layer J-PET detector from plastic scintillators and a symmetric spherical-shaped annihilation chamber for positronium production. Around 48 million ortho-positronium signal events are identified from 356 days of measurement from April 2021 - August 2022.

The presented result is compared with the previous two best-known studies with the Gammasphere and J-PET detector where the precision for the CPT symmetry test reached 0.0026 $\pm$ 0.0031 [9] and 0.00067 $\pm$ 0.00095 [8], respectively. With this study, the amplitude of CPT violating angular correlation in o-Ps decays with J-PET obtained is -0.00029 $\pm$ 0.00022, a factor of 4 smaller than the last best-known experiment [8]. The comparison of the expectation value obtained from the previously best-known experiments to the current results is given in Fig. 6.1.

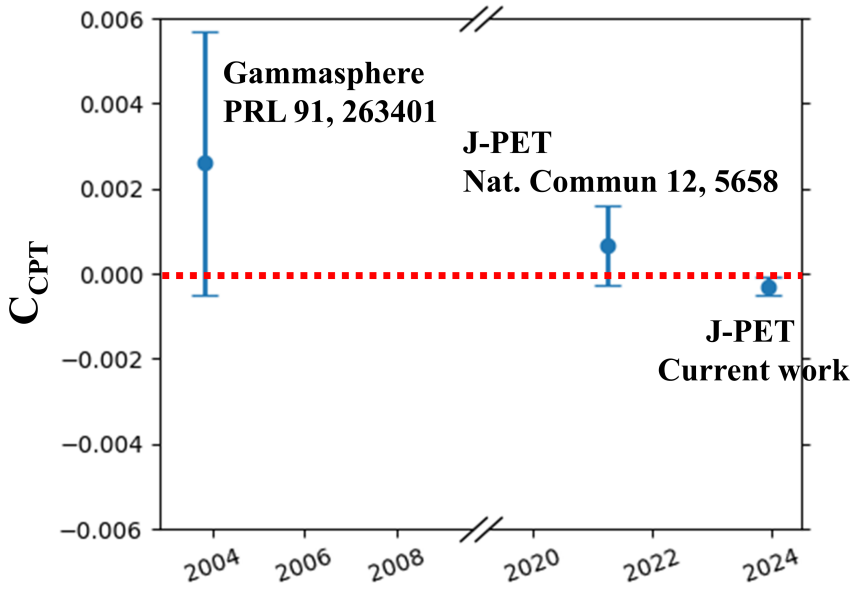

FIGURE 6.1: Comparison of the expectation value of the CPT violating angular correlation for the two previous two most precise tests with Gammasphere [9] and J-PET [8] detector with the present obtained result. The red line at zero represents no CPT symmetry violation. The error bars around each value correspond to the total uncertainty reported by each experiment.

Chapter 7

Into the Future: Optimization of the Modular J-PET geometry for the next generation of CPT symmetry test

A new generation J-PET detector has been built from plastic scintillators that came into operation in the year 2022 for Medical research. This detector system is portable and can be combined with the 3-layer J-PET to enhance the sensitivity for precision studies. A new experiment is planned to test the CPT symmetry with this prototype combined with the 3-layer J-PET. As a part of this thesis, Monte Carlo simulations were performed to optimize the setup for this future experiment. The study aims to optimize the geometrical configuration of the detector to evaluate the measurement time and conditions needed to achieve the sensitivity of 10^{-5} to CPT violation in o-Ps decays. A Monte Carlo simulation-based study is presented with the new modular J-PET detector system and a spherical annihilation chamber showing different configurations of the combined setup of single and multi-layer new modular J-PET with the existing 3-layer J-PET detector.

7.1 Modular J-PET detector

The Modular J-PET is a novel, portable positron emission tomography (PET) detector comprised of 24 detection modules [54, 96, 97]. Each module utilizes densely packed BC-404 plastic scintillator strips of 50 cm in length and cross-section of $24 \times 6\ mm^2$. These are wrapped in Vikuiti ESR foil and DuPont B Kapton foil for high reflection and light tightness, ensuring optimal light collection efficiency [66]. Signals are read out using a 1×4 matrix (6×6 mm^2) of silicon photomultipliers (SiPMs) of Hamamatsu S-13 type affixed to both ends of each scintillator strip. The key features of this detector include the reconfiguration possibility of individual modules into single or multi-layer geometries and portability. The advantage of the detector being reconfigurable

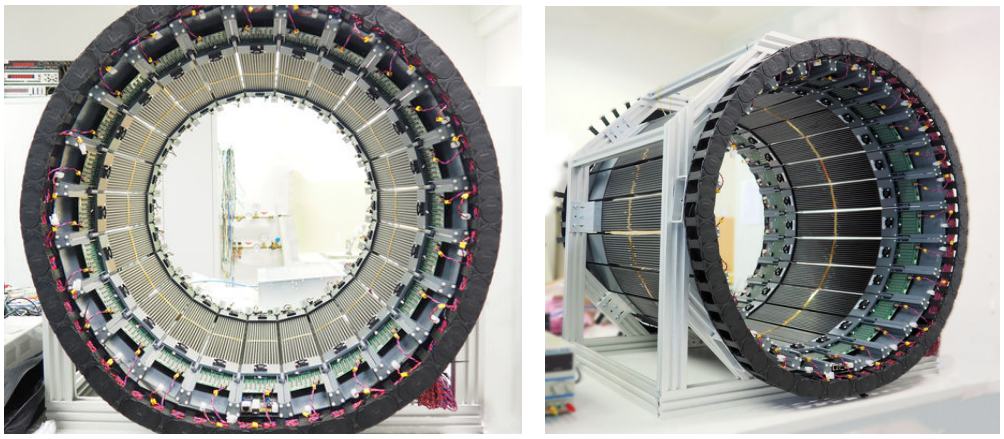

FIGURE 7.1: **Modular J-PET detector**. Photographs of the modular J-PET detector where its 24 modules are assembled cylindrically to form a single layer detector. representing the schematic and rotated view of the detector. The scintillators are wrapped in black foil and closely packed to form a single module. There are electronic boards on two ends of a single module.

into multiple layers is currently being exploited through Monte Carlo simulations to optimize the detector's configuration for high-precision measurements of CPT symmetry. The detector setup is shown in Fig. 7.1. The detector prototype has already been tested in various studies like positronium imaging with human patients [54], proton beam therapy [98, 99], physics studies using positronium beams [100, 29], etc.

7.2 Simulation study with different geometries of Modular J-PET

The six different detector geometries of Modular J-PET are studied. These are simulated using the J-PET Geant4 Monte Carlo simulation toolkit [86]. The considered geometrical setups include the 3-layer J-PET detector and the modular J-PET with 24 modules arranged cylindrically in single or multiple layers with a spherical annihilation chamber at its center. The placement of modules is at a different inner radius from the center of the detector depending upon the number of layers. The chamber configuration is adapted from the experiment with the 3-layer detector in Section 2.2. The geometrical setups are categorized based on the number of modules from Modular J-PET used in different layers. The configurations are listed below and their geometrical representation is given in Fig. 7.2.

(a) **3-layer J-PET + 24 modules:** A four-layer detector setup with 3 already-in-use J-PET detector with a single layer of 24 modules of Modular J-PET.

(b) **3-layer J-PET + 16+8 modules:** A five-layer setup with the 3-layer J-PET and 2 layers using 16 and 8 modules of modular J-PET.

(c) **3-layer J-PET + 14+10 modules:** 3-layer J-PET and 2 layers using 14 and 10 modules of modular J-PET.

(d) **3-layer J-PET + 12+12 modules:** The 3-layer J-PET and 2 layers using 12 and 12 modules of modular J-PET.

(e) **24 modules:** 24 Modular digital J-PET used as a stand-alone single-layer detector.

(f) **12+12 modules:** 24 modular digital J-PET used as a stand-alone detector with two layers of 12 modules each.

The positioning of modules in different setups is given in Table 7.1. A spherical annihilation chamber with porous silica coating on its inner walls, enclosed in a cylindrical tube was used in each detector setup as shown in Fig. 7.2. The simulated detector geometries are shown in the transverse plane in Fig. 7.2 and two of these detector configurations are shown form a different angle in Fig. 7.3.

TABLE 7.1: Radius of single and multiple layer modular J-PET in different detector configurations with respect to the center of modules

Detector geometry	Modular layer radius to the center of modules (cm)
3-layer + 24 modules	38
3-layer + 16+8 modules	23.5 and 20
3-layer + 14+10 modules	27 and 21
3-layer + 12+12 modules	28 and 23
24 modules	38
12 + 12 modules	38 and 33

7.3 A comparison study with 3-layer J-PET detector

Performance parameters are studied to compare the geometries with the 3-layer J-PET detector. These parameters are based on the registration and identification of the o-Ps signal events. For each geometrical configuration, 10^{10} events are generated in MC J-PET Geant4 software and further reconstructed using J-PET Framework software, as done for the 3-layer setup explained in Chapter 4. The parameters used for the reconstruction are $E_{dep} = 30$ keV, $\sigma_t = 225$ ps and $\sigma_z = 2$ cm with a source activity of 1.1 MBq. The events are analyzed from the perspective of identification of three gamma annihilations from the o-Ps atom. The analysis steps include the hit-level and event-level based selection criteria with similar cut variables as explained in the previous study with the 3-layer setup in Section 4.2. Due to the different geometry and properties of the modular J-PET, values of certain cuts had to be adjusted to qualitatively reflect those used for the three-layer detector. The photons with energy deposition of less than 340 keV are accepted. The scatter test cut value is 18 cm and the condition on a sum of the two smallest angles between annihilation photons is greater than 180° for this comparison study keeping the flow of analysis scheme similar to the 3-layer setup.

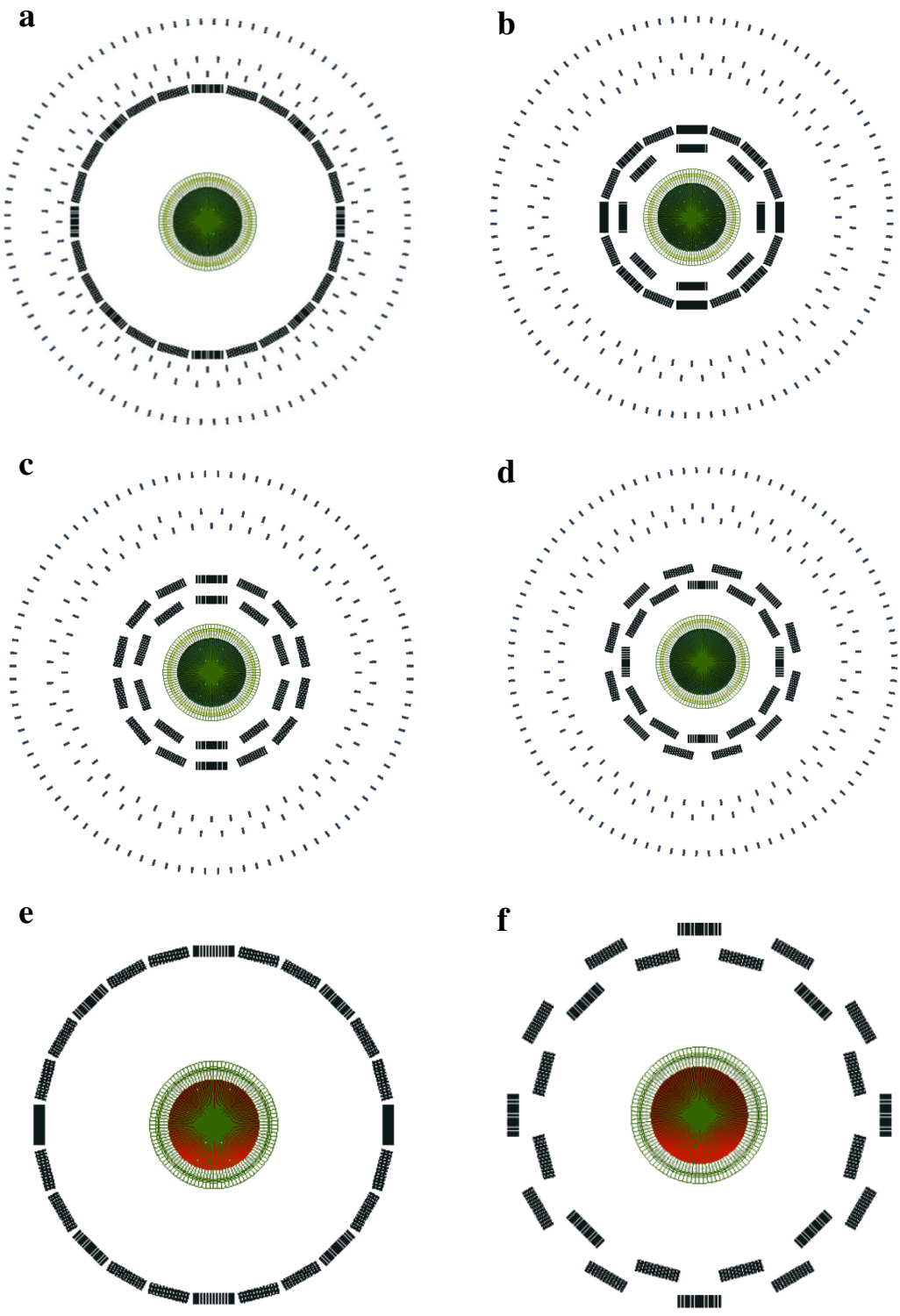

FIGURE 7.2: **Simulated detector configurations.** Schematic view of 3-layer J-PET and other possible geometries from 24 modules like (a) 24 Modules + 3-layer J-PET, (b) 16 and 8 modules + 3-layer J-PET, (c) 14 and 10 modules with 3-layer J-PET, (d) 12 and 12 modules with 3-layer J-PET, (e) 24 modular as a standalone J-PET detector and (f) 12 and 12 modules of modular J-PET with spherical annihilation chamber at the center of each detector geometry in Geant4.

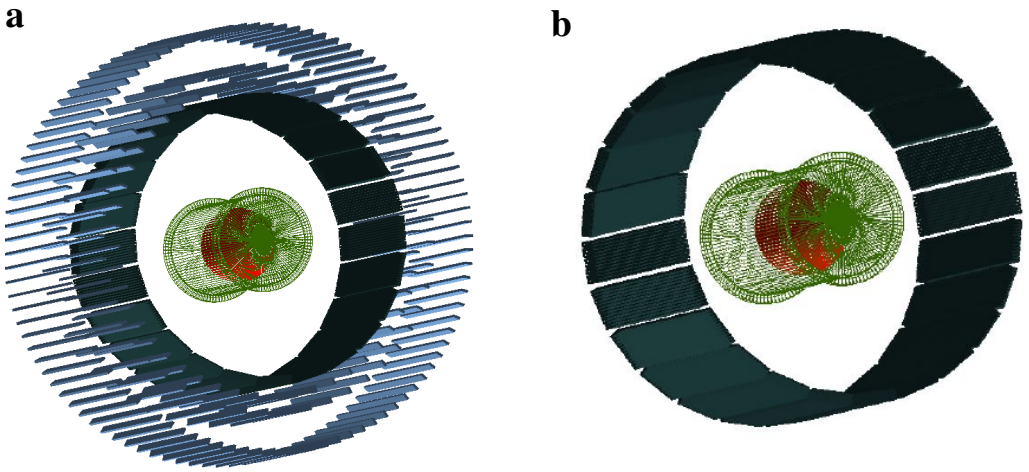

FIGURE 7.3: **Rotated view of detector configuration.** Geant4 visualization of (a) 3-layer J-PET and Modular J-PET, and (b) Modular as a standalone J-PET detector with spherical annihilation chamber at the center of each detector geometry. It is the rotated representation of (a) and (e) geometries in Fig. 7.2.

7.3.1 Efficiency estimation

The effective comparison between the different geometrical configurations is based on estimating the efficiency of registration of signal events in a particular detector setup. The total efficiency of registering and selecting o-Ps events is compared for different configurations. The registration efficiency of registering three photons from o-Ps events is given by $\epsilon_{registration}$, and $\epsilon_{analysis}$ is the analysis efficiency estimated after applying the selection cuts for the identification of signal events.

The registration efficiency is the probability of registration of three-photon annihilations of o-Ps in the detector. The registration efficiency of o-Ps events for different configurations of J-PET is defined in Equation 7.1. The relative gain of registration efficiency with respect to 3-layer J-PET is given in Table 7.2.

$$\epsilon_{registration} = \frac{\text{Number of o-Ps events recorded in detector}}{\text{Total number of generated } 3\gamma \text{ events}} \tag{7.1}$$

The estimation of registration efficiency does not include the effect of detector resolutions. The studies indicate that the registration efficiency of a single modular layer combined with a 3-layer J-PET is 28 times higher than the 3-layer J-PET detector. The multi-layer modular detector combined with three-layer J-PET gives the maximum registration efficiency of o-Ps events out of all the configurations.

The analysis efficiency is taken as a product of the relative event selection efficiency of o-Ps events after each selection cut used in the analysis. The analysis scheme is divided into two sections, i.e. hit-level and event-level criteria (explained in Section 3.2), and the efficiency of selecting o-Ps events is estimated after each of these two and given in Table 7.3. ϵ_{hit} is the relative event selection efficiency after hit-level criteria and ϵ_{event} is after event-level selection criteria.

TABLE 7.2: Registration efficiency for o-Ps$\rightarrow 3\gamma$ events in the detector. The Gain factor is defined to compare the efficiency of each detector setup to the 3-layer J-PET detector.

Detector geometry	$\epsilon_{registration}$	Gain factor (w.r.t 3-layer)
3-layer (current J-PET)	0.26 * 10^{-3}	1
(a) 3-layer + 24 modules	7.32 * 10^{-3}	28
(b) 3-layer + 16+8 modules	3.0 * 10^{-2}	28 $\times$4.1
(c) 3-layer + 14+10 modules	2.7 * 10^{-2}	28 $\times$3.7
(d) 3-layer + 12+12 modules	2.5 * 10^{-2}	28 $\times$3.4
(e) 24 modules	0.4 * 10^{-2}	28 $\times$0.55
(f) 12 + 12 modules	0.5 * 10^{-2}	28 $\times$0.68

TABLE 7.3: The relative event selection efficiency of o-Ps events after hit-level selection cuts and event-level selection criteria.

Detector geometry	ϵ_{hit}	ϵ_{event}
3-layer J-PET	0.69	0.46
(a) 3-layer + 24 modules	0.42	0.27
(b) 3-layer + 16+8 modules	0.29	0.24
(c) 3-layer + 14+10 modules	0.29	0.25
(d) 3-layer + 12+12 modules	0.29	0.26
(e) 24 modules	0.46	0.41
(f) 12 + 12 modules	0.44	0.39

The analysis efficiency of configurations from single and multi-layer modular J-PET are comparatively higher than the combined modular and 3-layer setup. After the selection criteria, the total efficiency of each setup is estimated from the number of o-Ps events left after the selection cuts and the total number of generated events; given in Equation 7.2. The comparison of each setup with 3-layer J-PET is given in Table 7.4.

$$\text{Total Efficiency} = \frac{\text{No. of o-Ps events after selection cut}}{\text{Total no. of generated events}} \tag{7.2}$$

As mentioned above, the analysis procedure used in this MC simulation study is similar to the one described in Section 3.2 and 4.2. The cut value for $\theta_1 + \theta_2$ variable is kept at a lower value of $\theta_1 + \theta_2 > 180^\circ$, compared to the value used in the usual analysis of 3-layer J-PET. The cut value is based on the hypothesis to eliminate the events 2γ annihilations where sum of two smallest angles is around 180° for such kind of events.

The studies depict that the overall efficiency of detecting o-Ps events in the combined setup of a single-layer modular detector with a three-layer detector is 21 times higher than the 3-layer J-PET

TABLE 7.4: The comparison of total efficiency for o-Ps events of different geometrical configurations to the 3-layer J-PET. The gain factor defined is to compare the configurations w.r.t 3-layer detector and is estimated based on total efficiency. The signal-to-background ratio (S/B) is estimated for each geometry.

Detector geometry	Total Efficiency	Gain factor	S/B
3-layer (current J-PET)	5.1×10^{-6}	1	0.5
(a) 3-layer + 24 modules	108.6×10^{-6}	21	0.06
(b) 3-layer + 16+8 modules	324.4×10^{-6}	21×3	0.08
(c) 3-layer + 14+10 modules	297.7×10^{-6}	21×2.7	0.08
(d) 3-layer + 12+12 modules	294×10^{-6}	21×2.7	0.1
(e) 24 modules	81.3×10^{-6}	21×0.75	0.3
(f) 12 + 12 modules	106.5×10^{-6}	21×0.98	0.22

detector. And it is around 60 times higher for five layer detector configuration combining multi-layer modular with three-layer J-PET. The signal-to-background ratio is evaluated after the selection criteria on the sum of the two smallest angles (angle sum) between photons $\theta_1 + \theta_2 > 180°$; cut variable is explained in Section 3.2. The value of signal to background ratio for single and double layer modular J-PET configurations is close to the one obtained from 3-layer J-PET detector. While it is less for the configurations from the combined setup of modular and 3-layer J-PET. It could be due to the more Compton scattered events in the four or five layer setup. The value of S/B for a 3-layer setup in Table 7.4 is comparatively less than the one estimated in the previous study given in Table 5.2 due to the different cut value for last selection criteria.

7.3.2 Other parameters

A few parameters like the fraction of secondary Compton scatterings, signal-to-background ratio (S/B), etc. are studied in MC simulations of different detector configurations. The fraction of secondary Compton scatterings in different detection setups is estimated from the total number of events where at least one of the primary photons from o-Ps annihilations has it's secondary (scattered) photon registered in the detector or annihilation chamber. The fraction of such events contributes to 10% for the three-layer J-PET, 38% for the four-layer setup (a), 28% for the five-layer setup (b, c, d), and 7% for the configurations from modular J-PET only (e and f) [101]. The background from scatterings is higher in case of four and five layer configurations due to the high probability of recording secondary photons with more layers. It resulted in low values of signal to background ratio for four and five layer detector setup as compare to configurations from only modular setup (given in Table 7.4). Also, the angular resolution of five layer configuration detector (b, c, d) is lower than other configurations due smaller distance from the source.

7.4 Conclusion

The MC simulation study gives major reasons to use the stand-alone 24 modular J-PET detector with spherical annihilation chamber for the next generation of CPT symmetry tests to be performed by J-PET collaboration. Although the selected detector geometry has lower registration efficiency for signal than multi-layer setups, it also has a lower background contribution from Compton scatterings in the detector. Selecting this geometry also allows for easier data acquisition and a better understanding of systematic uncertainties as compared to a setup where two different detector types have to be combined. The overall gain in efficiency for 24 modular J-PET is around 15 times higher than the present setup which would result in lowering the time of measurement. It is estimated that the seven months of measurement with stand-alone single-layer modular prototype could result in achieving the precision at the level of 10^{-5} for next CPT symmetry test.

Chapter 8

Summary and perspectives

The thesis aimed to test the CPT symmetry with a 192 plastic strip J-PET detector in ortho-positronium (o-Ps) annihilations, achieving higher precision than previous experiments. In the performed experiment, the CPT symmetry was tested in o-Ps decays, a purely leptonic system, by searching for the non-zero expectation value of the angular correlations between the o-Ps spin and the annihilation plane [1]. The detector setup included a spherical annihilation chamber for positronium production, centered within the three-layer J-PET detector.

The thesis reports the experimental measurements conducted over 356 days between April 2021 - August 2022. Two sets of measurements were performed at different source activities of 1.1 MBq (78 days) and 4 MBq (278 days) using the same experimental setup. This test represents the second generation CPT symmetry test with J-PET where the first test was conducted with a different annihilation chamber geometry using a higher source activity of 10 MBq for 30 days [8].

The presented selection criteria for signal events resulted in the identification of a total of 47.8 million o-Ps $\rightarrow 3\gamma$ events in the experimental data. A dedicated Monte Carlo simulation study was conducted to validate the selection criteria of candidate events in the data. Additionally, different background components that could mimic the 3γ signal events were evaluated. The final data sample was estimated to have a signal purity of approximately 55% with the rest consisting of background from the secondary Compton scatterings within the annihilation chamber and scintillators.

The potential sources of systematic uncertainty in this study were discussed in this work. The expectation value of the CPT odd operator is evaluated for the identified o-Ps events, which is

$$< O_{CPT} >= -0.00011 \pm 0.00008$$

resulting in

$$C_{CPT} = -0.00029 \pm 0.00022$$

where C_{CPT} is the correlation amplitude of the CPT-odd decays. C_{CPT} = 1 corresponds to the maximum CPT-odd asymmetry amplitude leading to the effects of CPT violation. Till now none of the experiments has observed any asymmetry in the CPT-odd decays.

The obtained results are consistent with the CPT invariance at the precision of 10^{-4}. The achieved precision is a factor of 4 better than the previous CPT symmetry test with J-PET [8]. The study has set a new limit on CPT-violating effects using the angular correlation operator in o-Ps decays.

The last part of the thesis focuses on the simulation study to optimize the best detector geometry for the future CPT symmetry test with J-PET that aims to further improve the precision of this study to the level of 10^{-5} [102]. The study concludes with a next-generation CPT symmetry test using a 24 Modular J-PET system as a stand-alone single-layer detector. The data-taking campaign with Modular J-PET and spherical annihilation chamber started in the beginning of 2023 [103] and was completed in November 2023. Following the estimation from simulation studies, 7 months of experimental data was collected for the next CPT symmetry test. It is expected to improve the registration efficiency of 3γ from o-Ps annihilations by a factor of 15 due to the higher granularity of Modular J-PET compared to the 3-layer setup. Lastly, the outlook of the number of ortho-positronium events collected with J-PET for the CPT symmetry tests since 2018, is shown in Fig. 8.1.

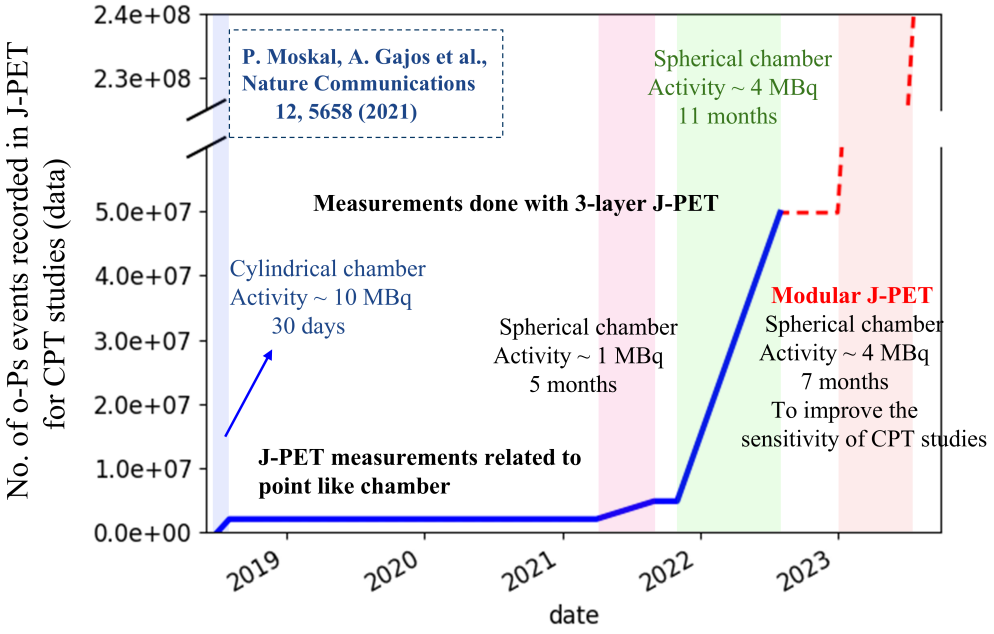

FIGURE 8.1: The "luminosity plot" of o-Ps event rate for the overall CPT symmetry tests with J-PET. Outlook of the total number of ortho-positronium events recorded in the J-PET device in its different experimental runs conducted so far for the CPT symmetry studies with large annihilation chambers (cylindrical and spherical) at different source activities. Flat lines indicate intervals where measurements with another chamber were conducted. The last column (red) shows a prediction about the measurements with Modular J-PET and spherical annihilation chamber that started at the beginning of 2023. The measurements aimed to collect two hundred million o-Ps events which would be 100 times more statistics than the first measurement with J-PET.

It is worth mentioning that the measurements shown in red column of Fig. 8.1 with Modular J-PET has already been conducted but its analysis and results are not in the scope of this work, which is why it is shown as a future perspective (in dashed lines).

Another aspect towards future perspective could be to improve the signal purity in the sample by using Machine learning algorithms. A test study was performed with a 3-layer J-PET MC simulations to classify the o-Ps signal events from background using ML approach as given in ref. [104]. The multivariate analysis were performed using classification algorithms given in TMVA based ROOT package [105]. This would be done in more detail for the studies with Modular J-PET.

Appendix A

Kinematic Fit

The decay vertex and time of o-Ps $\rightarrow 3\gamma$ events are reconstructed using the trilateration method [83] (given in Section 3.2). This method takes into account the position and time of interaction of three annihilation photons in the detector. The annihilation point of o-Ps into three photons can be determined by finding the intersection of three spheres centered at the photon interaction points, which is the basic principle of the trilateration method. Because these photons originate from a single point, their paths lie on a common plane. This constraint, combined with the detected photon interaction points, allows for a 2D reconstruction of the decay position within this plane. This solution is then transformed back to the 3D detector coordinate system.

The kinematic fit can be used to improve the precision of the reconstructed annihilation point and decay time of o-Ps events. This fitting is based on the least square method that simultaneously optimizes the three position coordinates of photons' interaction in the detector and their times of interaction.

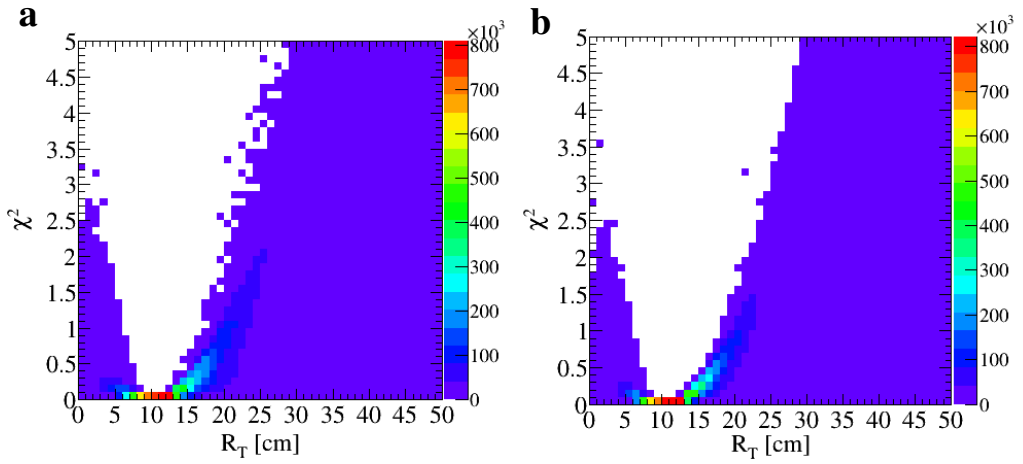

FIGURE A.1: χ^2 distribution as a function of reconstructed annihilation radius (from Equation. 4.3) for (a) experimental data and (b) MC simulations.

This fitting approach can be useful to accurately determine the spin of ortho-positronium which is required for the construction of CPT-sensitive operator $\vec{S} \cdot (\vec{k_1} \times \vec{k_2})$. For this fitting, the timing information of photon interactions was adjusted within their error bounds by minimizing the distance between the center of the detector of reconstructed annihilation points of the identified o-Ps events (termed as annihilation radius given in Equation. 4.3) and radius of spherical annihilation chamber (R = 10 cm). The χ^2 test is performed to check the variations between chamber radius and reconstructed annihilation radius. The distribution of χ^2 test versus the reconstructed annihilation radius from Equation. 4.3 is given in Fig. A.1 for experimental data (A.1 (a)) and MC simulations (A.1 (b)). The events with less than $\chi^2 = 0.5$ are only considered for further evaluation. The same selection criteria are applied for the identification of o-Ps events as described in Section 3.2 for data and in Section 4.2 for MC simulations.

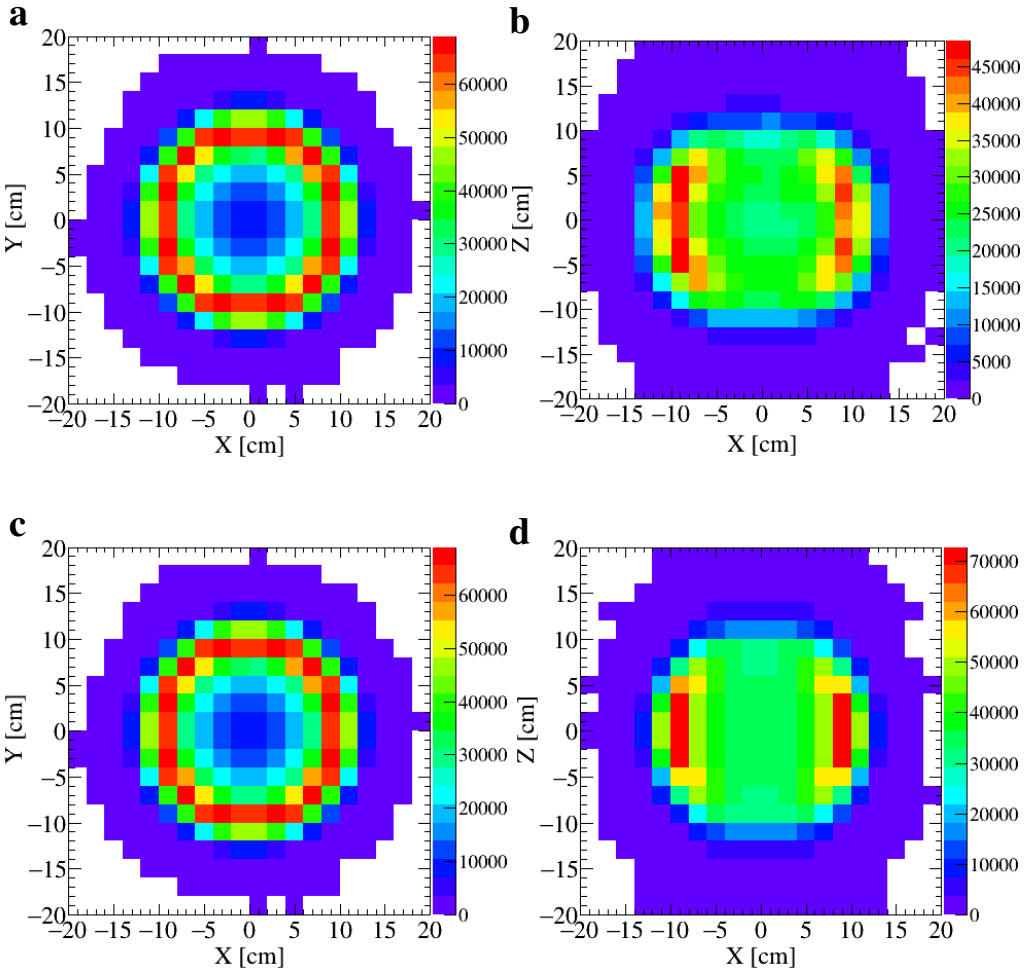

FIGURE A.2: The reconstructed annihilation point distribution of o-Ps after the cut on χ^2 less than 0.5 for data and MC simulations. (a) and (c) represent the transverse XY view of annihilations in the case of data and simulations while (b) and (d) represent the XZ view in the case of data and simulations respectively.

The improvement in the reconstructed position of the decay vertex can be realized from the annihilation point distribution of identified o-Ps events in the XY and XZ plane of the detector as given in Fig. A.2.

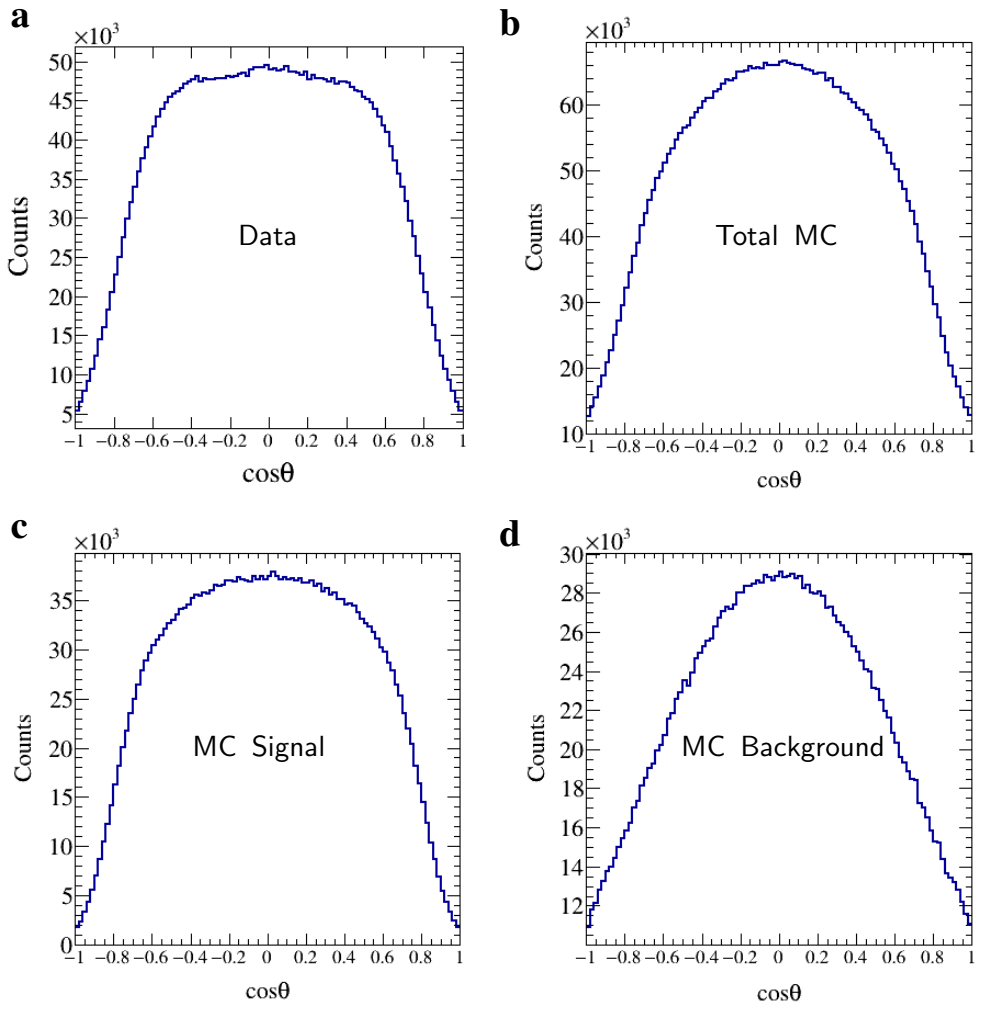

FIGURE A.3: The CPT-sensitive operator distribution obtained for the good kinematic fit identified o-Ps events from (a) experimental data, (b) total MC simulated events, (c) MC simulated signal events, and (d) background events from MC.

The distribution of CPT violating angular correlation for the o-Ps events is given in Fig A.3.

It should be noted that the kinematic fitting method was not employed in this analysis. Although this approach enhanced the quality of the reconstructed three-gamma images, it did not yield significant improvements in the final results. Incorporating this fitting method would have introduced additional uncertainty in the final results. To avoid this, it was excluded from the present work.

Bibliography

[1] P. Moskal, D. Alfs, T. Bednarski, P. Białas, E. Czerwiński, C. Curceanu, A. Gajos, B. Głowacz, M. Gorgol, B. Hiesmayr, *et al.*, "Potential of the J-PET detector for studies of discrete symmetries in decays of positronium atom - a purely leptonic system," *Acta Phys. Polon. B* **47** (2016) 509.

[2] S. D. Bass, "QED and Fundamental Symmetries in Positronium Decays," *Acta Phys. Polon. B* **50** (2019) 1319.

[3] M. Sozzi, "Tests of discrete symmetries," *Journal of Physics G: Nuclear and Particle Physics* **47** no. 1, (2019) 013001.

[4] B. K. Arbic, S. Hatamian, M. Skalsey, J. Van House, and W. Zheng, "Angular-correlation test of CPT in polarized positronium," *Physical Review A* **37** no. 9, (1988) 3189.

[5] P. Moskal, S. Niedźwiecki, T. Bednarski, E. Czerwiński, E. Kubicz, I. Moskal, M. Pawlik-Niedźwiecka, N. Sharma, M. Silarski, M. Zieliński, *et al.*, "Test of a single module of the J-PET scanner based on plastic scintillators," *Nuclear Instruments and Methods in Physics Research Section A: Accelerators, Spectrometers, Detectors and Associated Equipment* **764** (2014) 317–321.

[6] P. Moskal, N. Zoń, T. Bednarski, P. Białas, E. Czerwiński, A. Gajos, D. Kamińska, A. Kochanowski, G. Korcyl, J. Kowal, *et al.*, "A novel method for the line-of-response and time-of-flight reconstruction in TOF-PET detectors based on a library of synchronized model signals," *Nuclear Instruments and Methods in Physics Research Section A: Accelerators, Spectrometers, Detectors and Associated Equipment* **775** (2015) 54–62.

[7] S. Niedźwiecki, P. Białas, C. Curceanu, E. Czerwiński, K. Dulski, A. Gajos, B. Głowacz, M. Gorgol, B. Hiesmayr, B. Jasińska, *et al.*, "J-PET: a new technology for the whole-body PET imaging," *Acta Phys. Polon. B* **48** (2017) 1567.

[8] P. Moskal, A. Gajos, M. Mohammed, J. Chhokar, **N. Chug**, C. Curceanu, E. Czerwiński, M. Dadgar, K. Dulski, M. Gorgol, *et al.*, "Testing CPT symmetry in ortho-positronium decays with positronium annihilation tomography," *Nature Communications* **12** no. 1, (2021) 5658.

[9] P. A. Vetter and S. J. Freedman, "Search for CPT-odd decays of positronium," *Physical review letters* **91** no. 26, (2003) 263401.

[10] M. Sozzi, "Discrete symmetries and CP violation: From experiment to theory,". Oxford University Press, 2008.

[11] T.-D. Lee and C.-N. Yang, "Question of parity conservation in weak interactions," *Physical Review* **104** no. 1, (1956) 254.

[12] C.-S. Wu, E. Ambler, R. W. Hayward, D. D. Hoppes, and R. P. Hudson, "Experimental test of parity conservation in beta decay," *Physical review* **105** no. 4, (1957) 1413.

[13] J. I. Friedman and V. L. Telegdi, "Nuclear emulsion evidence for parity nonconservation in the decay chain $\pi + \rightarrow \mu+ \rightarrow e+$," *Physical Review* **106** no. 6, (1957) 1290.

[14] C. Bouchiat and L. Michel, "Theory of μ-meson decay with the hypothesis of nonconservation of parity," *Physical Review* **106** no. 1, (1957) 170.

[15] I. In, "Observations of the failure of conservation of parity and charge conjugation in meson decays: the magnetic moment of the free muon,".

[16] J. H. Christenson, J. W. Cronin, V. L. Fitch, and R. Turlay, "Evidence for the 2 π decay of the k 2 0 meson," *Physical Review Letters* **13** no. 4, (1964) 138.

[17] R. G. Sachs, "The physics of time reversal,". University of Chicago Press, 1987.

[18] O. W. Greenberg, "CPT violation implies violation of lorentz invariance," *Physical Review Letters* **89** no. 23, (2002) 231602.

[19] A. Angelopoulos, A. Apostolakis, E. Aslanides, G. Backenstoss, P. Bargassa, O. Behnke, A. Benelli, V. Bertin, F. Blanc, P. Bloch, *et al.*, "First direct observation of time-reversal non-invariance in the neutral-kaon system," *Physics Letters B* **444** no. 1-2, (1998) 43–51.

[20] J. Lees, V. Poireau, V. Tisserand, J. G. Tico, E. Grauges, A. Palano, G. Eigen, B. Stugu, D. N. Brown, L. Kerth, *et al.*, "Observation of time-reversal violation in the b 0 meson system," *Physical Review Letters* **109** no. 21, (2012) 211801.

[21] M. Borchert, J. Devlin, S. Erlewein, M. Fleck, J. Harrington, T. Higuchi, B. Latacz, F. Voelksen, E. Wursten, F. Abbass, *et al.*, "A 16-parts-per-trillion measurement of the antiproton-to-proton charge–mass ratio," *Nature* **601** no. 7891, (2022) 53–57.

[22] B. M. Latacz, B. P. Arndt, B. Bauer, J. A. Devlin, S. R. Erlewein, M. Fleck, J. Jäger, M. Schiffelholz, G. Umbrazunas, E. J. Wursten, *et al.*, "Base—high-precision comparisons of the fundamental properties of protons and antiprotons," *The European Physical Journal D* **77** no. 6, (2023) 94.

[23] R. S. Van Dyck Jr, P. B. Schwinberg, and H. G. Dehmelt, "New high-precision comparison of electron and positron g factors," *Physical Review Letters* **59** no. 1, (1987) 26.

[24] P. Schwinberg, R. Van Dyck Jr, and H. Dehmelt, "Trapping and thermalization of positrons for geonium spectroscopy," *Physics Letters A* **81** no. 2-3, (1981) 119–120.

[25] R. Bluhm, V. A. Kostelecký, and N. Russell, "CPT and lorentz tests in hydrogen and antihydrogen," *Physical Review Letters* **82** no. 11, (1999) 2254.

[26] M. Ahmadi, B. Alves, C. Baker, W. Bertsche, A. Capra, C. Carruth, C. Cesar, M. Charlton, S. Cohen, R. Collister, *et al.*, "Characterization of the 1s–2s transition in antihydrogen," *Nature* **557** no. 7703, (2018) 71–75.

[27] B. Schwingenheuer, R. Briere, A. Barker, E. Cheu, L. Gibbons, D. Harris, G. Makoff, K. McFarland, A. Roodman, Y. Wah, *et al.*, "CPT tests in the neutral kaon system," *Physical review letters* **74** no. 22, (1995) 4376.

[28] W. Bernreuther, U. Löw, J. Ma, and O. Nachtmann, "How to test CP, T, and CPT invariance in the three photon decay of polarized 3S1 positronium," *Zeitschrift für Physik C Particles and Fields* **41** no. 1, (1988) 143–158.

[29] S. Sharma, J. Baran, R. S. Brusa, R. Caravita, **N. Chug**, A. Coussat, C. Curceanu, E. Czerwiński, M. Dadgar, K. Dulski, *et al.*, "J-PET detection modules based on plastic scintillators for performing studies with positron and positronium beams," *Journal of Instrumentation* **18** no. 02, (2023) C02027.

[30] C. Amsler, A. Ariga, T. Ariga, S. Braccini, C. Canali, A. Ereditato, J. Kawada, M. Kimura, I. Kreslo, C. Pistillo, *et al.*, "A new application of emulsions to measure the gravitational force on antihydrogen," *Journal of instrumentation* **8** no. 02, (2013) P02015.

[31] P. Moskal, K. Dulski, **N. Chug**, C. Curceanu, E. Czerwiński, M. Dadgar, J. Gajewski, A. Gajos, G. Grudzień, B. C. Hiesmayr, *et al.*, "Positronium imaging with the novel multiphoton PET scanner," *Science Advances* **7** no. 42, (2021) eabh4394.

[32] R. Lehnert, "CPT symmetry and its violation," *Symmetry* **8** no. 11, (2016) 114.

[33] D. Colladay and V. A. Kostelecký, "CPT violation and the standard model," *Physical Review D* **55** no. 11, (1997) 6760.

[34] D. Colladay and V. A. Kostelecký, "Lorentz-violating extension of the standard model," *Physical Review D* **58** no. 11, (1998) 116002.

[35] A. D. Sakharov, "Violation of cp-invariance, c-asymmetry, and baryon asymmetry of the universe," in *In The Intermissions... Collected Works on Research into the Essentials of Theoretical Physics in Russian Federal Nuclear Center, Arzamas-16* (1998) 84–87. World Scientific.

[36] K. Abe, R. Akutsu, A. Ali, C. Alt, C. Andreopoulos, L. Anthony, M. Antonova, S. Aoki, A. Ariga, T. Arihara, *et al.*, "Constraint on the matter–antimatter symmetry-violating phase in neutrino oscillations," *Nature* **580** no. 7803, (2020) 339–344.

[37] G. Barenboim, C. A. Ternes, and M. Tórtola, "Neutrinos, dune and the world best bound on CPT invariance," *Physics Letters B* **780** (2018) 631–637.

[38] R. H. Parker, C. Yu, W. Zhong, B. Estey, and H. Müller, "Measurement of the fine-structure constant as a test of the standard model," *Science* **360** no. 6385, (2018) 191–195.

[39] H. Dehmelt, R. Mittleman, R. Van Dyck Jr, and P. Schwinberg, "Past electron-positron g- 2 experiments yielded sharpest bound on CPT violation for point particles," *Physical Review Letters* **83** no. 23, (1999) 4694.

[40] X. Fan, T. Myers, B. Sukra, and G. Gabrielse, "Measurement of the electron magnetic moment," *Physical review letters* **130** no. 7, (2023) 071801.

[41] S. D. Bass, S. Mariazzi, P. Moskal, and E. Stępień, "Colloquium: Positronium physics and biomedical applications," *Reviews of Modern Physics* **95** no. 2, (2023) 021002.

[42] L. Gurung, T. Babij, S. Hogan, and D. Cassidy, "Precision microwave spectroscopy of the positronium n= 2 fine structure," *Physical Review Letters* **125** no. 7, (2020) 073002.

[43] G. Adkins, D. Cassidy, and J. Pérez-Ríos, "Precision spectroscopy of positronium: Testing bound-state QED theory and the search for physics beyond the standard model," *Physics Reports* **975** (2022) 1–61.

[44] A. P. Mills and S. Berko, "Search for C nonconservation in electron-positron annihilation," *Physical Review Letters* **18** no. 11, (1967) 420.

[45] P. A. Vetter and S. J. Freedman, "Branching-ratio measurements of multiphoton decays of positronium," *Physical Review A* **66** no. 5, (2002) 052505.

[46] G. S. Adkins, D. R. Droz, D. Rastawicki, and R. N. Fell, "Orthopositronium decay form factors and two-photon correlations," *Physical Review A* **81** no. 4, (2010) 042507.

[47] J. Pérez-Ríos and S. T. Love, "Searching for light dark matter through positronium decay," *The European Physical Journal D* **72** (2018) 1–5.

[48] S. Andrukhovich, N. Antovich, and A. Berestov, "A spectrometer for the study of angular correlations in polarized-orthopositronium decay," *Instruments and Experimental Techniques* **43** (2000) 453–459.

[49] S. Andrukhovich, N. Antovich, A. Berestov, P. Vukotich, A. Gurinovich, O. Metelitsa, and A. Khrushchinskii, "A method for selecting three-photon positronium-annihilation events with a multidetector coincidence spectrometer," *Instruments and Experimental Techniques* **43** (2000) 295–299.

[50] I.-Y. Lee, "The gammasphere," *Nuclear Physics A* **520** (1990) c641–c655.

[51] T. Yamazaki, T. Namba, S. Asai, and T. Kobayashi, "Search for CP violation in positronium decay," *Physical review letters* **104** no. 8, (2010) 083401.

[52] P. Moskal, E. Czerwiński, J. Raj, S. D. Bass, E. Y. Beyene, **N. Chug**, A. Coussat, C. Curceanu, M. Dadgar, M. Das, *et al.*, "Discrete symmetries tested at 10^{-4} precision using linear polarization of photons from positronium annihilations," *Nature Communications* **15** no. 1, (2024) 78.

[53] C. Bartram, R. Henning, and D. Primosch, "Demonstration of o-ps detection with a cylindrical array of nai detectors," *Nuclear Instruments and Methods in Physics Research Section A: Accelerators, Spectrometers, Detectors and Associated Equipment* **966** (2020) 163856.

[54] P. Moskal, J. Baran, S. Bass, J. Choiński, **N. Chug**, C. Curceanu, E. Czerwiński, M. Dadgar, M. Das, K. Dulski, *et al.*, "Positronium image of the human brain in vivo," *Science Advances* **10** no. 37, (2024) eadp2840.

[55] D. W. Jeong, A. Khan, H. W. Park, J. Lee, and H. Kim, "Optimization and characterization of detector and trigger system for a kapae design," *Nuclear Instruments and Methods in Physics Research Section A: Accelerators, Spectrometers, Detectors and Associated Equipment* **989** (2021) 164941.

[56] H. Park, D. Jeong, J. Jegal, A. Khan, and H. Kim, "A novel hermetic detection system of kapae for measuring multiphoton decays of positronium," *Journal of Instrumentation* **18** no. 03, (2023) P03011.

[57] T.-E. Haugen, E. A. George, O. Naviliat-Cuncic, and P. A. Voytas, "Search for CP-violation in ortho-positronium decay," in *EPJ Web of Conferences*, vol. 282, p. 01003, EDP Sciences (2023).

[58] P. Moskal, P. Salabura, M. Silarski, J. Smyrski, J. Zdebik, and M. Zielinski, "Novel detector systems for the positron emission tomography," *Bio Algorithms Med Syst.* **7** no. 2, (2011) 73–78.

[59] P. Moskal, "Matrix device and method for determining the location and time of reaction of the gamma quanta and the use of the device to determine the location and time of reaction of the gamma quanta in positron emission tomography," (Mar. 3, 2015) . US Patent 8,969,817.

[60] P. Moskal, T. Bednarski, P. Białas, M. Ciszewska, E. Czerwiński, A. Heczko, M. Kajetanowicz, Ł. Kapłon, A. Kochanowski, G. Konopka-Cupiał, *et al.*, "TOF-PET detector concept based on organic scintillators," *Nuclear Medicine Review* **15** no. C, (2012) 81–84.

[61] G. Korcyl, P. Moskal, T. Bednarski, P. Białas, E. Czerwiński, Ł. Kapłon, A. Kochanowski, J. Kowal, P. Kowalski, T. Kozik, *et al.*, "Trigger-less and reconfigurable data acquisition system for positron emission tomography," *Bio-Algorithms and Med-Systems* **10** no. 1, (2014) 37–40.

[62] G. Korcyl, P. Białas, C. Curceanu, E. Czerwiński, K. Dulski, B. Flak, A. Gajos, B. Głowacz, M. Gorgol, B. C. Hiesmayr, *et al.*, "Evaluation of single-chip, real-time tomographic data processing on FPGA SoC devices," *IEEE transactions on medical imaging* **37** no. 11, (2018) 2526–2535.

[63] M. Pałka, P. Moskal, T. Bednarski, P. Białas, E. Czerwiński, Ł. Kapłon, A. Kochanowski, G. Korcyl, J. Kowal, P. Kowalski, *et al.*, "A novel method based solely on field programmable gate array (fpga) units enabling measurement of time and charge of analog signals in positron emission tomography (pet)," *Bio-Algorithms and Med-Systems* **10** no. 1, (2014) 41–45.

[64] M. Pałka, P. Strzempek, G. Korcyl, T. Bednarski, S. Niedźwiecki, P. Białas, E. Czerwiński, K. Dulski, A. Gajos, *et al.*, "Multichannel FPGA based mvt system for high precision time (20 ps rms) and charge measurement," *Journal of Instrumentation* **12** no. 08, (2017) P08001.

[65] S. Vandenberghe, P. Moskal, and J. S. Karp, "State of the art in total body PET," *EJNMMI physics* **7** (2020) 1–33.

[66] Ł. Kapłon, "Technical attenuation length measurement of plastic scintillator strips for the total-body J-PET scanner," *IEEE Transactions on Nuclear Science* **67** no. 10, (2020) 2286–2289.

[67] P. Moskal, N. Krawczyk, B. Hiesmayr, M. Bała, C. Curceanu, E. Czerwiński, K. Dulski, A. Gajos, M. Gorgol, R. Del Grande, *et al.*, "Feasibility studies of the polarization of photons beyond the optical wavelength regime with the J-PET detector," *The European Physical Journal C* **78** (2018) 1–9.

[68] P. Moskal, "Towards total-body modular PET for positronium and quantum entanglement imaging," in *2018 IEEE Nuclear Science Symposium and Medical Imaging Conference Proceedings (NSS/MIC)*, pp. 1–4, IEEE (2018).

[69] P. Moskal, "Positron Emission Tomography could be aided by entanglement," *Physics* **17** (2024) 138.

[70] P. Moskal, D. Kumar, S. Sharma, E. Beyene, **N. Chug**, A. Coussat, C. Curceanu, E. Czerwinski, M. Das, K. Dulski, *et al.*, "Non-maximal entanglement of photons from positron-electron annihilation demonstrated using a novel plastic PET scanner," *arXiv:2407.08574* (2024) .

[71] P. Moskal, "Positronium imaging," in *2019 IEEE Nuclear Science Symposium and Medical Imaging Conference (NSS/MIC)*, pp. 1–3, IEEE (2019).

[72] P. Moskal, D. Kisielewska, C. Curceanu, E. Czerwiński, K. Dulski, A. Gajos, M. Gorgol, B. Hiesmayr, B. Jasińska, K. Kacprzak, *et al.*, "Feasibility study of the positronium imaging with the J-PET tomograph," *Physics in Medicine & Biology* **64** no. 5, (2019) 055017.

[73] P. Moskal, D. Kisielewska, R. Y. Shopa, Z. Bura, J. Chhokar, C. Curceanu, E. Czerwiński, M. Dadgar, K. Dulski, J. Gajewski, *et al.*, "Performance assessment of the 2 γ positronium imaging with the total-body PET scanners," *EJNMMI physics* **7** (2020) 1–16.

[74] M. Gorgol, B. Jasińska, M. Kosior, E. Stępień, and P. Moskal, "Construction of the vacuum chambers for J-PET experiments with positron annihilation," *Acta Physica Polonica. B* **51** no. 1, (2020) .

[75] E. P. Barrett, L. G. Joyner, and P. P. Halenda, "The determination of pore volume and area distributions in porous substances. i. computations from nitrogen isotherms," *Journal of the American Chemical society* **73** no. 1, (1951) 373–380.

[76] A. Gajos, "Sensitivity of discrete symmetry tests in the positronium system with the J-PET detector," *Symmetry* **12** no. 8, (2020) 1268.

[77] B. Jasińska, M. Gorgol, M. Wiertel, R. Zaleski, D. Alfs, T. Bednarski, P. Białas, E. Czerwiński, K. Dulski, A. Gajos, *et al.*, "Determination of the 3γ fraction from positron annihilation in mesoporous materials for symmetry violation experiment with J-PET scanner," *Acta Phys. Polon. B* **47** (2016) 453.

[78] https://github.com/JPETTomography/j-pet-framework.

[79] P. Moskal, N. Sharma, M. Silarski, T. Bednarski, P. Białas, J. Bułka, E. Czerwiński, A. Gajos, D. Kamińska, L. Kapłon, *et al.*, "Hit Time and Hit Position Reconstruction in the J-PET Detector Based on a Library of Averaged Model Signals," *Acta Phys. Polon. A* **127** (2015) 1495–1499.

[80] S. Sharma, J. Chhokar, C. Curceanu, E. Czerwiński, M. Dadgar, K. Dulski, J. Gajewski, A. Gajos, M. Gorgol, N. Gupta-Sharma, *et al.*, "Estimating relationship between the time over threshold and energy loss by photons in plastic scintillators used in the J-PET scanner," *EJNMMI physics* **7** no. 1, (2020) 1–15.

[81] D. E. Alburger, "Gamma-radiation from Na^{22} and Co^{60}," *Physical Review* **76** no. 3, (1949) 435.

[82] S. Sharma, J. Baran, **N. Chug**, C. Curceanu, E. Czerwiński, M. Dadgar, K. Dulski, K. Eliyan, A. Gajos, N. Gupta-Sharma, *et al.*, "Efficiency determination of J-PET: first plastic scintillators-based PET scanner," *EJNMMI physics* **10** no. 1, (2023) 28.

[83] A. Gajos, D. Kamińska, E. Czerwiński, D. Alfs, T. Bednarski, P. Białas, B. Głowacz, M. Gorgol, B. Jasińska, G. Korcyl, *et al.*, "Trilateration-based reconstruction of ortho-positronium decays into three photons with the J-PET detector," *Nuclear Instruments and Methods in Physics Research Section A: Accelerators, Spectrometers, Detectors and Associated Equipment* **819** (2016) 54–59.

[84] D. Kamińska, A. Gajos, E. Czerwiński, D. Alfs, T. Bednarski, P. Białas, C. Curceanu, K. Dulski, B. Głowacz, N. Gupta-Sharma, *et al.*, "A feasibility study of ortho-positronium decays measurement with the J-PET scanner based on plastic scintillators," *The European Physical Journal C* **76** (2016) 1–14.

[85] M. Skalsey, T. Girard, and A. Rich, "Longitudinal polarization of positrons in ^{22}Na decay," *Physical Review C* **32** no. 3, (1985) 1014.

[86] https://github.com/JPETTomography/J-PET-geant4/.

[87] J. Allison, K. Amako, J. Apostolakis, P. Arce, M. Asai, T. Aso, E. Bagli, A. Bagulya, S. Banerjee, G. Barrand, *et al.*, "Recent developments in geant4," *Nuclear instruments and methods in physics research section A: Accelerators, Spectrometers, Detectors and Associated Equipment* **835** (2016) 186–225.

[88] **N. Chug** and A. Gajos, "CPT symmetry test in positronium annihilations with the J-PET detector," *PoS* **PANIC2021** (2022) 440.

[89] **N. Chug**, "Exploring the limits of CPT symmetry in ortho-positronium decays with J-PET," *PoS* **EPS-HEP2023** (2024) 366.

[90] M. Mohammed, "Study of angular correlations in the ortho-positronium annihilation with the J-PET detector for the search of CPT symmetry violation," PhD thesis (2020).

[91] O. Behnke, K. Kröninger, G. Schott, and T. Schörner-Sadenius, "Data analysis in high energy physics: a practical guide to statistical methods,". John Wiley & Sons, 2013.

[92] R. Barlow, "Systematic errors: facts and fictions," *arXiv preprint hep-ex/0207026* (2002) .

[93] R. Barlow, "A calculator for confidence intervals," *Computer Physics Communications* **149** no. 2, (2002) 97–102.

[94] P. Adlarson, W. Augustyniak, W. Bardan, M. Bashkanov, F. Bergmann, M. Berłowski, H. Bhatt, M. Büscher, H. Calén, I. Ciepał, *et al.*, "Investigation of the dd→ 3 he n π 0 reaction with the fz jülich wasa-at-cosy facility," *Physical Review C—Nuclear Physics* **88** no. 1, (2013) 014004.

[95] P. Adlarson, W. Augustyniak, W. Bardan, M. Bashkanov, F. Bergmann, M. Berłowski, H. Bhatt, A. Bondar, M. Büscher, H. Calén, *et al.*, "Charge symmetry breaking in dd→ he4π0 with wasa-at-cosy," *Physics Letters B* **739** (2014) 44–49.

[96] P. Moskal and E. Stępień, "Prospects and clinical perspectives of total-body PET imaging using plastic scintillators," *PET clinics* **15** no. 4, (2020) 439–452.

[97] F. Tayefi Ardebili, S. Niedźwiecki, and P. Moskal, "Evaluation of modular J-PET sensitivity," *Bio-Algorithms and Med-Systems* **19** no. 1, (2023) .

[98] J. Baran, D. Borys, K. Brzeziński, J. Gajewski, M. Silarski, **N. Chug**, A. Coussat, E. Czerwiński, M. Dadgar, K. Dulski, *et al.*, "Feasibility of the J-PET to monitor the range of therapeutic proton beams," *Physica Medica* **118** (2024) 103301.

[99] K. Brzeziński, J. Baran, D. Borys, J. Gajewski, **N. Chug**, A. Coussat, E. Czerwiński, M. Dadgar, K. Dulski, K. V. Eliyan, *et al.*, "Detection of range shifts in proton beam therapy using the j-pet scanner: a patient simulation study," *Physics in Medicine & Biology* **68** no. 14, (2023) 145016.

[100] S. Sharma, L. Povolo, S. Mariazzi, G. Korcyl, K. Kacprzak, D. Kumar, S. Niedźwiecki, J. Baran, E. Beyene, R. Brusa, R. Caravita, **N. Chug**, *et al.*, "Feasibility studies for imaging e+ e- annihilation with modular multi-strip detectors," *Nuclear Instruments and Methods in Physics Research Section A: Accelerators, Spectrometers, Detectors and Associated Equipment* **1062** (2024) 169192.

[101] **N. Chug** and A. Gajos, "Modular J-PET with improved o-Ps detection efficiency for CPT tests," in *Proceedings of the Ninth Meeting on CPT and Lorentz Symmetry*, pp. 253–255, World Scientific (2023).

[102] **N. Chug** and A. Gajos, "Towards improving the sensitivity of the CPT symmetry in positronium decays with the modular J-PET detector," *Acta Physica Polonica. B, Proceedings Supplement* **15** no. 4, (2022) .

[103] **N. Chug** and A. Gajos, "Improved test of CPT invariance in ortho-positronium decays at J-PET," *PoS* **DISCRETE2022** (2024) 064.

[104] **N. Chug** and P. Moskal, "Classification of signal events for CPT symmetry studies with J-PET using machine learning techniques," *Acta Phys. Polon. Supp.* **17** no. 7, (2024) 7–A2.

[105] A. Hoecker, P. Speckmayer, J. Stelzer, J. Therhaag, E. von Toerne, H. Voss, M. Backes, T. Carli, O. Cohen, A. Christov, *et al.*, "TMVA-toolkit for multivariate data analysis," *arXiv preprint physics/0703039* (2007) .

Acknowledgements

I would like to sincerely thank my supervisor, prof. Paweł Moskal, for his guidance and support throughout the project. His help and encouragement have been invaluable in reaching the final goal of this work.

I am very thankful to dr Aleksander Gajos, who introduced me to the world of research in different aspects. His advice and feedback have been essential in shaping this work.

I would like to extend my thanks to everyone in the J-PET group, especially dr Eryk Czerwiński, dr Sushil Sharma, dr Szymon Niedźwiecki, dr Magdalena Skurzok, dr Grzegorz Korcyl, dr Michał Silarski who have been consistently supportive throughout this journey. I am thankful to Deepak Kumar for all our discussions, especially while I was writing this thesis.

I am very grateful to my parents Maa - Papa and Badi Massi, for always encouraging me to follow my dreams. My younger brother, Yatin, who has been a huge support and always taken care of things back at home. I owe a special thanks to my grandparents Nana ji and Nani maa, and to Mausa ji, whose love, blessings and guidance have been lasting inspiration on my journey.

I am thankful to Soumi Banerjee for sharing many of my first experiences abroad and for always being there. Finally, I want to thank all other people I've met along the way, who taught me many things and gave memorable life experiences.

This work was supported by Polish National Science Center (NCN) through grant nos. 2019/35/B/ST2/03562, 2021/42/A/ST2/00423 and 2022/45/N/ST2/04084.